

Nanostructural Biomaterials and Applications

Guest Editors: Mingdong Dong, Lei Liu, and Shuai Zhang





Nanostructural Biomaterials and Applications

Journal of Nanomaterials

Nanostructural Biomaterials and Applications

Guest Editors: Mingdong Dong, Lei Liu, and Shuai Zhang



Copyright © 2016 Hindawi Publishing Corporation. All rights reserved.

This is a special issue published in "Journal of Nanomaterials." All articles are open access articles distributed under the Creative Commons Attribution License, which permits unrestricted use, distribution, and reproduction in any medium, provided the original work is properly cited.

Editorial Board

- Domenico Acierno, Italy
Katerina Aifantis, USA
Nageh K. Allam, USA
Margarida Amaral, Portugal
Martin Andersson, Sweden
Raul Arenal, Spain
Ilaria Armentano, Italy
Vincenzo Baglio, Italy
Lavinia Balan, France
Thierry Baron, France
Andrew R. Barron, USA
Hongbin Bei, USA
Daniel Bellet, France
Stefano Bellucci, Italy
Enrico Bergamaschi, Italy
Samuel Bernard, France
Debes Bhattacharyya, New Zealand
Sergio Bietti, Italy
Giovanni Bongiovanni, Italy
Theodorian Borca-Tasciuc, USA
Mohamed Bououdina, Bahrain
Torsten Brezesinski, Germany
C. Jeffrey Brinker, USA
Christian Brosseau, France
Philippe Caroff, Australia
Victor M. Castaño, Mexico
Albano Cavaleiro, Portugal
Bhanu P. S. Chauhan, USA
Shafiu Chowdhury, USA
Jin-Ho Choy, Republic of Korea
Kwang-Leong Choy, UK
Yu-Lun Chueh, Taiwan
Elisabetta Comini, Italy
Giuseppe Compagnini, Italy
David Cornu, France
Miguel A. Correa-Duarte, Spain
P. Davide Cozzoli, Italy
Shadi A. Dayeh, USA
Luca Deseri, USA
Yong Ding, USA
Philippe Dubois, Belgium
Zehra Durmus, Turkey
Joydeep Dutta, Oman
Ali Eftekhari, USA
Samy El-Shall, USA
- Ovidiu Ersen, France
Claude Estournès, France
Andrea Falqui, KSA
Matteo Ferroni, Italy
Ilaria Fratoddi, Italy
Alan Fuchs, USA
Miguel A. Garcia, Spain
Siddhartha Ghosh, Singapore
P. K. Giri, India
Russell E. Gorga, USA
Jihua Gou, USA
Jean M. Greneche, France
Smrati Gupta, Germany
Kimberly Hamad-Schifferli, USA
Simo-Pekka Hannula, Finland
Michael Harris, USA
Yasuhiko Hayashi, Japan
F. Hernandez-Ramirez, Spain
Michael Z. Hu, USA
Nay Ming Huang, Malaysia
Shaoming Huang, China
Zafar Iqbal, USA
Balachandran Jeyadevan, Japan
Xin Jiang, Germany
Rakesh Joshi, Australia
Jeong-won Kang, Republic of Korea
Hassan Karimi-Maleh, Iran
Antonios Kelarakis, UK
Alireza Khataee, Iran
Ali Khorsand Zak, Iran
Philippe Knauth, France
Ralph Krupke, Germany
Christian Kübel, Germany
Prashant Kumar, UK
Eric Le Bourhis, France
Jun Li, Singapore
Meiyong Liao, Japan
Shijun Liao, China
Silvia Licoccia, Italy
Wei Lin, USA
Nathan C. Lindquist, USA
Zainovia Lockman, Malaysia
Nico Lovergine, Italy
Jim Low, Australia
Jue Lu, USA
- Ed Ma, USA
Laura M. Maestro, Spain
Gaurav Mago, USA
Muhamamd A. Malik, UK
Devanesan Mangalaraj, India
Sanjay R. Mathur, Germany
Tony McNally, UK
Yogendra Mishra, Germany
Paulo Cesar Morais, Brazil
Paul Munroe, Australia
Jae-Min Myoung, Republic of Korea
Rajesh R. Naik, USA
Albert Nasibulin, Russia
Toshiaki Natsuki, Japan
Koichi Niihara, Japan
Natalia Noginova, USA
Sherine Obare, USA
Won-Chun Oh, Republic of Korea
Atsuto Okamoto, Japan
Abdelwahab Omri, Canada
Ungyu Paik, Republic of Korea
Piersandro Pallavicini, Italy
Edward A. Payzant, USA
Alessandro Pegoretti, Italy
Ton Peijs, UK
Oscar Perales-Pérez, Puerto Rico
Jorge Pérez-Juste, Spain
Alexey P. Popov, Finland
Philip D. Rack, USA
Peter Reiss, France
Orlando Rojas, USA
Marco Rossi, Italy
Ilker S. Bayer, Italy
Cengiz S. Ozkan, USA
Sudipta Seal, USA
Shu Seki, Japan
Vladimir Šepelák, Germany
Huaiyu Shao, Japan
Prashant Sharma, USA
Donglu Shi, USA
Bhanu P. Singh, India
Surinder Singh, USA
Vladimir Sivakov, Germany
Adolfo Speghini, Italy
Marinella Striccoli, Italy



Xuping Sun, KSA
Ashok K. Sundramoorthy, USA
Angelo Taglietti, Italy
Bo Tan, Canada
Leander Tapfer, Italy
Valeri P. Tolstoy, Russia
Muhammet S. Toprak, Sweden
R. Torrecillas, Spain
Achim Trampert, Germany
Takuya Tsuzuki, Australia

Tamer Uyar, Turkey
Bala Vaidhyanathan, UK
Luca Valentini, Italy
Rajender S. Varma, USA
Ester Vazquez, Spain
Ajayan Vinu, Australia
Ruibing Wang, Macau
Shiren Wang, USA
Yong Wang, USA
Magnus Willander, Sweden

Ping Xiao, UK
Zhi Li Xiao, USA
Yangchuan Xing, USA
Doron Yadlovker, Israel
Yoke K. Yap, USA
Kui Yu, Canada
William Yu, USA
Michele Zappalorto, Italy
Renyun Zhang, Sweden

Contents

Nanostructural Biomaterials and Applications

Mingdong Dong, Lei Liu, and Shuai Zhang
Volume 2016, Article ID 5903201, 2 pages

Improved Bonding Strength of Hydroxyapatite on Titanium Dioxide Nanotube Arrays following Alkaline Pretreatment for Orthopedic Implants

Yardnapar Parcharoen, Preecha Termsuksawad, and Sirinrath Sirivisoot
Volume 2016, Article ID 9143969, 13 pages

Characterization of Inter- and Intramolecular Interactions of Amyloid Fibrils by AFM-Based Single-Molecule Force Spectroscopy

Yinli Li, Hao Liang, Huiling Zhao, Dong Chen, Bo Liu, Thomas Fuhs, and Mingdong Dong
Volume 2016, Article ID 5463201, 18 pages

Micro-CT Imaging of RGD-Conjugated Gold Nanorods Targeting Tumor *In Vivo*

Xiaochao Qu, Xiaoxiao Li, Jingning Liang, Yanran Wang, Muhan Liu, and Jimin Liang
Volume 2016, Article ID 8368154, 13 pages

Niosomes as Nanoparticulate Drug Carriers: Fundamentals and Recent Applications

Didem Ag Sepeci, Muharrem Sepeci, Johanna-Gabriela Walter, Frank Stahl, and Thomas Scheper
Volume 2016, Article ID 7372306, 13 pages

Enhanced Stem Cell Osteogenic Differentiation by Bioactive Glass Functionalized Graphene Oxide Substrates

Xiaoju Mo, Yan Wei, Xuehui Zhang, Qing Cai, Yang Shen, Xiaohan Dai, Song Meng, Xing Liu, Yun Liu, Zhewen Hu, and Xuliang Deng
Volume 2016, Article ID 5613980, 11 pages

Editorial

Nanostructural Biomaterials and Applications

Mingdong Dong,¹ Lei Liu,² and Shuai Zhang³

¹Interdisciplinary Nanoscience Center (iNANO), Aarhus University, 8000 Aarhus, Denmark

²Institute for Advanced Materials, Jiangsu University, Zhenjiang 212013, China

³Physical Sciences Division, Pacific Northwest National Laboratory, Richland, WA 99352, USA

Correspondence should be addressed to Mingdong Dong; dong@inano.au.dk

Received 6 September 2016; Accepted 6 September 2016

Copyright © 2016 Mingdong Dong et al. This is an open access article distributed under the Creative Commons Attribution License, which permits unrestricted use, distribution, and reproduction in any medium, provided the original work is properly cited.

Nanostructure is the structure, at least one of whose dimensions is in nanoscale, normally between 0.1 nm and 100 nm. With the recent exciting progress of nanoscience and nanotechnology, kinds of materials with nanostructures are being discovered and synthesized every day. As being one of the key subcatalogs, biomaterials with nanostructures are rapidly developing. The integration of nanostructures into biomaterials gives them unique structures and special and inspiring properties. Hence, a variety of nanostructural biomaterials have been applied in many aspects of daily life, like medical treatment and diagnosis. This field is still fast developing, and it has significant effects on improving our world. In this special issue, we collect three original works and two overviews from the researchers in Thailand, China, Denmark, and Germany. They present to people the promising applications of nanostructural biomaterials in tissue engineering, drug delivery, and disease diagnosis. These works aim to inspire further researches and efforts focusing on biofunctionalized nanomaterials and the corresponding applications.

S. Sirivisoot et al. in Thailand and X. Deng et al. in China have provided two marvelous cases in bone-tissue engineering with biological composite nanomaterials. S. Sirivisoot et al. (in “Improved Bonding Strength of Hydroxyapatite on Titanium Dioxide Nanotube Arrays following Alkaline Pretreatment for Orthopedic Implants”) have focused on introducing nanostructures on Ti implant, in order to influence the further adsorbed hydroxyapatite (HA). They used alkaline to pretreat titanium dioxide nanotubes (ATi) on Ti surface, which is of capability to accelerate the formation of HA layer on top and tune the orientation. The synthesized

HA-ATi nanocomposite successfully mimics natural bone tissue and improves bioactivity of this type of orthopedic implants. That makes it a kind of new approach toward producing orthopedic implants with much longer functional life.

Unlike S. Sirivisoot et al.’s focus, X. Deng et al. (in “Enhanced Stem Cell Osteogenic Differentiation by Bioactive Glass Functionalized Graphene Oxide Substrates”) put their efforts to manipulate stem cell osteogenesis, in order to regenerate bone tissue. They utilized sol-gel method to synthesize graphene oxide (GO) and bioactive glasses (BG) hybrid scaffold. This new kind of biofunctional nanomaterial keeps the biological properties from the parents’ materials. The following cellular activity analysis provided promising evidence to demonstrate that the hybrid scaffold, with unique nanostructure and biological properties, is of capability to trigger osteogenic differentiation of *mesenchymal* stem cells. That is a positive sign for the potential application of GO hybrid materials in bone restoration.

The hybrid nanomaterial could have medical applications other than the candidates for medical treatment. J. Liang et al. from China reported the usage of Au nanorod- (AuNR-) peptide hybrid for tumor diagnosis (in “Micro-CT Imaging of RGD-Conjugated Gold Nanorods Targeting Tumor *In Vivo*”). They conjugated AuNRs with peptide RGD, which is a kind of receptor targeting some tumor cells and tumor neovasculature overexpressed Integrin $\alpha_v\beta_3$. The conjugated nanoparticles eliminated the cytotoxicity of AuNRs, but they improve the ability to target tumor cells *in vivo* and *in vitro*. The micro-CT results also prove their feasibility to target tumor models. And the uptaken level of AuNRs-RGD

nanoparticles is determined by the expression level of Integrin $\alpha_v\beta_3$ from tumor cells. All of the mentioned advantages give the authors a kind of promising candidate to diagnose tumors via micro-CT.

In other researches, hybrid nanoparticles have been used as nanocarriers to deliver drugs. T. Scheper et al. from Germany introduced and reviewed the application of noisome as nanodrug carriers. Noisome is self-associated by nonionic surfactants and cholesterol; and people have proved that it has several key advantages to deliver drugs, like biocompatibility, high stability in creature bodies, and feasibility to target specific site by controlled manner. The authors systematically introduced the structure and component of noisome. They further summarized the available methods to prepare and characterize noisome nanocarriers. In the end, the recent applications of noisome in drug delivery as nanocarriers were reviewed. We believe both academic researcher and therapeutic engineers will be inspired from this detailed review.

In nanoscience and nanotechnology, developing the techniques to characterize and evaluate nanostructures and nanomaterials is of the same importance as their fabrication and synthesis, and corresponding applications. M. Dong and his colleagues from Denmark, Germany, and China reviewed the applications of atomic force microscopy (AFM) and AFM based single-molecular force spectroscopy (AFM-SMFS) to characterize inter- and intramolecular interactions of amyloid self-assembly nanofibril, in order to understand the mechanism of amyloidogenesis on nanoscale. Besides, they also introduced the idea to consider amyloid fibrils as nanomaterials, due to the outstanding mechanical properties and the corresponding potentials. This review will also inspire the readers from the relevant fields of AFM and AFM-SMFS to characterize and evaluate other kinds of biofunctionalized nanomaterials.

In summary, all these authors present the feasibility of nanostructural biomaterials in a number of aspects and several promising bioapplications. They convince people of the attractive future of biofunctional nanomaterials in daily life, especially in medical related fields. Hopefully, this special issue will inspire the ideas to synthesize new biofunctionalized nanomaterials and the corresponding applications. We wish that it also raises people's enthusiastic efforts in related researches.

*Mingdong Dong
Lei Liu
Shuai Zhang*

Research Article

Improved Bonding Strength of Hydroxyapatite on Titanium Dioxide Nanotube Arrays following Alkaline Pretreatment for Orthopedic Implants

Yardnapar Parcharoen,¹ Preecha Termsuksawad,² and Sirinrath Sirivisoot³

¹Chulabhorn International College of Medicine, Thammasat University, Pathum Thani 12121, Thailand

²Division of Materials Technology, School of Energy, Environment and Materials,
King Mongkut's University of Technology Thonburi, Bangkok 10140, Thailand

³Biological Engineering Program, Faculty of Engineering, King Mongkut's University of Technology Thonburi,
Bangkok 10140, Thailand

Correspondence should be addressed to Sirinrath Sirivisoot; sirinrath.sir@kmutt.ac.th

Received 22 April 2016; Accepted 4 July 2016

Academic Editor: Lei Liu

Copyright © 2016 Yardnapar Parcharoen et al. This is an open access article distributed under the Creative Commons Attribution License, which permits unrestricted use, distribution, and reproduction in any medium, provided the original work is properly cited.

Hydroxyapatite (HA) is a bioactive bone substitute used in biomedical applications. One approach to use HA for bone implant application is to coat it on titanium (Ti) implant. However, adhesion of HA on Ti is major concern for their long-term use in orthopedic implants. To enhance the adhesion strength of HA coating on titanium (Ti), the surface of the Ti was anodized and alkaline pretreated prior to coating on Ti by electrodeposition. Alkaline pretreatment of titanium dioxide nanotubes (ATi) accelerated the formation of HA, which mimicked the features and structure of natural bone tissue. Nanostructured HA formed on the ATi and pretreated ATi (P-ATi), unlike on conventional Ti. This study is the first to show that the bonding of HA coating to a P-ATi substrate was stronger than those of HA coating to Ti and to ATi. The preosteoblast response tests were also conducted. The results indicated that HA coating improved preosteoblast proliferation after 3 days in standard cell culture.

1. Introduction

Recently, more than 90 percent of the elderly of world's populations suffer from bone-related trauma, such as osteoporosis, bone cancers, rheumatoid arthritis, or accidents, which require spinal, hip, and knee replacements [1]. Thus, a huge success in bone implant development is anticipated in 2030 [2]. In Thailand, the total cost of orthopedic implants increased from \$4.9 million in 2002 to \$39.7 million in 2010.

Bone is composed of ceramic and biosubstance that draws attention among material engineers, who look for material to substitute for bone. This substituted material should possess both high strength and fracture toughness, appropriated for orthopedic implants [3]. Common biomaterials used for bone replacements are stainless steels, cobalt-chromium (Co-Cr) alloys, titanium (Ti), and Ti alloys. Among these metals, the tensile modulus of Ti-based materials is closest

to that of bone. Additionally, wear and corrosion resistances of Ti-based materials are higher than those of the other two materials because of natural TiO₂ formation on the Ti-based surface. Although TiO₂ is bioinert in physiological environments, Ti-based implants often fail after 10–20 years of service. Failure modes include bone fracture around the implanted materials (due to lower elastic modulus of bone than that of the implant), wear or corrosion of the implant, inflammation, and infection [4]. Moreover, naturally formed TiO₂ has low osteoconduction [5, 6], which causes implant loosening leading to failure [7]. To provide high bioactivity and to improve bone ingrowth, one approach is to use Ti with a coating of nanostructured hydroxyapatite (HA).

HA is a naturally derived ceramic found in bones and its calcium to phosphate atomic ratio (Ca/P) is 1.67 [8]. Various coating methods of hydroxyapatite (HA) on Ti surface have been investigated, such as Ti soaking in simulated

body fluid (SBF) (mimicking naturally HA forming), plasma spraying, sol-gel deposition in HA particles solution, pulsed laser deposition, hot isostatic pressing, and electrochemical deposition [9–16]. HA coating by electrochemical deposition was shown to possess excellent corrosion protection and good biocompatibility under host environment [17]. Advantages of this technique are that it is relatively inexpensive and thickness of the coating can be easily controlled. Another concern point is that mechanical bonding strength of the HA coating should withstand the bone growth stresses, induced during the bone healing process [18]. The adhesion of electro-deposited HA on smooth Ti surface was observed to be very weak, which may cause implant loosening [19–22]. Therefore, to increase the adhesion strength between HA and Ti surface, one suggested method is to use TiO₂ nanotube array as a substrate for HA electrodeposition. In addition to improving bonding strength, HA grown on TiO₂ nanotube array is more favorable to osteoblast (or bone-forming cell) growth and differentiation when compared with naturally formed TiO₂ layer on conventional Ti. It was also found that nanostructure surface could promote deposition of bone minerals, induced by osteoblasts [23].

TiO₂ nanotubular can be formed by several methods, such as sol-gel method [24], electrophoretic deposition [25], and anodization [26]. These methods could form different tube alignment on surface. The vertically aligned TiO₂ nanotube arrays can be achieved by anodization method with various parameters (electrolytes, voltages, etc.) [27, 28]. In the present study, anodization using pulse voltage and neutral-viscous, fluoride-containing electrolyte was investigated to achieve a uniform, well-oriented TiO₂ nanotube arrays (ATi). The previous study shows that alkaline surface treatment on ATi and subsequently annealing of HA-electrodeposited ATi at high temperature (>300°C) improve the bonding strength between HA and ATi [29]. However, the results from another study suggested that annealed HA grown in simulated body fluid (SBF) at high temperature (>300°C) was not always necessary because HA grown in SBF still possesses the Ca/P ratio of 1.67, closely mimicking natural bone minerals [30, 31].

In the present study, HA coatings were coated onto alkaline pretreated TiO₂ nanotubes. The anodization conditions included two different values of pulse voltage (+20/−4 and +35/−4 V) and temperatures (5 and 25°C). The influence of alkaline pretreatment on ATi and physical structures (e.g., wall thickness, diameter, and length) of TiO₂ nanotubes on the growth of bioinspired HA was reported. The mechanical bonding strength of HA on its substrates was studied as an *in vitro* early assessment of long-term stability in the human body. The physical and chemical characteristics (e.g., structure, size, and a ratio of Ca/P) of HA were investigated to elucidate the effect of using this biomaterial to increase the preosteoblast viability under standard cell culture conditions.

2. Experimental Materials and Methods

2.1. Forming TiO₂ Nanotube Arrays. Ti plate (Supra Alloys Inc., USA) of 99.9% purity was polished using silicon

carbide papers (TOA, Thailand) of progressively decreasing roughness of 400, 600, 800, 1000, 1500, and 2000 grits. The samples were then polished with 0.05 μm alumina powder (Allied, USA) to achieve a mirror quality finish. Freshly polished Ti was then washed with deionized (DI) water and sonicated in acetone (Sigma-Aldrich, Thailand) and 95 vol% ethanol (Sigma-Aldrich, Thailand) for five minutes each before immediate anodization.

Anodization method was used to produce TiO₂ nanotube arrays. Ti was used as a positive electrode, whereas platinum was used as a negative electrode. The electrolyte was a mixture of 90 vol% glycerol and 10 vol% ammonium fluoride (NH₄F) (0.36 M) in water. Anodization was performed with the pulse voltage of either +20/−4 or +35/−4 V, the conditions from a previous study by Chanmanee et al. [32]. The anodization was carried out at either 5°C or 25°C for 90 minutes. Then anodized sample was washed with deionized water before it was dried with nitrogen gas at room temperature. All ATi samples were then annealed at 450°C for 30 minutes to obtain the anatase phase.

2.2. Electrodeposition of Hydroxyapatite. ATi samples were pretreated with 1 M NaOH at 50°C for two minutes. After the pretreatment, the HA deposition was conducted. The electrolyte for HA deposition was prepared by dissolving ammonium phosphate (NH₄H₂PO₄, 1.67 mM) (Sigma-Aldrich, Thailand) and calcium nitrate (Ca(NO₃)₂, 2.5 mM) (Sigma-Aldrich, Thailand) in distilled water. To increase ionic conductivity and to buffer pH of electrolyte at 7.2, 0.15 M NaCl (Ajax Finechem, New Zealand), tris(hydroxyl amino-methane) (Ajax Finechem, New Zealand), and hydrochloric acid (Ajax Finechem, New Zealand) were mixed [29]. The pretreatment ATi (P-ATi) was used as a negative electrode, whereas platinum was used as a positive electrode. Electrodeposition of HA was processed at −2.5 V and at 80°C for 10 minutes.

2.3. Physical and Chemical Characterizations of Anodized Titanium and Hydroxyapatite Coating. Scanning electron microscopy (FE-SEM, CamScanMX2600, UK) was used to investigate surface morphology of ATi. The dimensions of the TiO₂ nanotubes were measured using image analysis software (ImageJ version 1.32, NIH). The crystal structures of the surfaces of the NaOH-pretreated ATi and the HA-coated samples were investigated by X-ray diffractometer (Shimadzu Model: XRD 6000, Japan).

2.4. The Mechanical Properties of Coated Hydroxyapatite on Anodized Titanium. The mechanical bonding strength of coated HA on ATi was evaluated by tensile testing following an ASTM F 1044-05 standard [33]. Two HA-coated samples were glued together face-to-face using Plasmatech Klebbi adhesive (Plasma-Technik AG, Switzerland) and cured at 190°C for two hours. Tensile tests were conducted by a computer-controlled universal testing machine (Instron, Model 5500R, US) at a cross head speed of 0.25 centimeter

per minute (0.1 inch/minute). The degree of bonding strength was calculated as shown in

$$\text{Bonding strength (MPa)} = \frac{\text{Maximum load to failure (N)}}{\text{cross-sectional area (m}^2\text{)}} \quad (1)$$

2.5. Preosteoblast Cell Response

2.5.1. Cell Culture. Preosteoblasts (MC3T3-E, passage number = 10, MTEC, Thailand), or bone-forming cells, were used in the present study. Cells were cultured in alpha-modified minimal essential medium (alpha-MEM; Invitrogen Corporation, Paisley, UK) supplemented with 10 vol% fetal calf serum (Dominique Dutcher, Brumath, France) and 1 vol% penicillin/streptomycin (Invitrogen Corporation) at 37°C in humidified atmosphere of 5% CO₂ in air. The cell culture media were replaced every three days. Cells were seeded and cultured on plastic polystyrene (control); Ti; ATi; P-ATi; HA-ATi; and HA-P-ATi at the cell density of 5 × 10⁴ cells/cm².

2.5.2. Cell Morphology. After three days in culture, cells were fixed with 2.5 vol% sodium phosphate buffered glutaraldehyde (Sigma-Aldrich, Thailand) at pH 7 for 20 minutes. After two washes, the cells were postfixed with 1 vol% osmium tetroxide (OsO₄) (Sigma-Aldrich, Thailand) in saturated mercuric chloride (HgCl₂) (Sigma-Aldrich, Thailand). The

samples were then dehydrated with a series of ethanol washes (20, 30, 40, 50, 60, 70, 80, 90, and 100 vol%) at room temperature. All samples were subsequently critical-point dried (EMSCOPE CPD-750, Ashford, UK). The samples were coated with gold (EMSCOPE SC-500, UK) at a thickness of 10 nm before being characterized by SEM. The cell morphology on Ti, ATi, P-ATi, HA-coated on ATi (HA-ATi), and HA-coated on P-ATi (HA-P-ATi) was observed using SEM (JEOL J-SM-5300, Japan) at an accelerating voltage of 20 kV.

2.5.3. Cell Viability. Cells were seeded onto plastic polystyrene (control) and coated samples at a density of 5 × 10⁴ cells·cm⁻² in 24-well culture plates. Cell viability was tested using a commercial 3-[4,5-dimethylthiazol-2-yl]-2,5-diphenyl tetrazolium bromide (MTT) assay (Sigma-Aldrich, Thailand). The 10 vol% MTT solution in 1x phosphate buffer saline was mixed with alpha-MEM without phenol red to form a yellowish solution before being added onto the cell-seeded samples at the day 3 of cultures. Mitochondrial dehydrogenases of viable cells cleave the tetrazolium ring, yielding purple formazan crystals on cell-seeded samples after incubation for an hour. The absorbance of purple solution was measured at 570 nm wavelength using a spectrophotometer (Synergy Mx Multimode Reader, US). A concomitant change in the amount of formazan formed correlates to the change in the number of viable cells on the samples. The percentage of viable cells on the samples was calculated as shown in

$$\text{Cell viability (\%)} = \frac{\text{Absorbance of colored solution incubated with samples} \times 100\%}{\text{Absorbance of colored solution incubated with control (Polystyrene plate)}} \quad (2)$$

2.6. Statistical Analysis. Two-way analysis of variance (ANOVA) was used in the analysis of wall thickness, diameter, and length of TiO₂ nanotubes, which were anodized with different voltage pulses and temperatures. ANOVA was used to statistically analyze the effects of materials on bonding strength of the HA coatings and cell viability. The statistical analysis was performed using Minitab 16 (Minitab Inc., USA) software. Significant level of 0.05 ($p < 0.05$) was used for the test.

3. Results and Discussion

3.1. Characteristics of Anodized Titanium. Gong et al. reported that a certain anodization potential must be applied to yield ordered TiO₂ nanotube arrays [26]. Therefore, in this study, to control the size of the nanotubes, anodization potentials were varied. Figure 1 showed top-view SEM images of ATi, which were anodized under two different temperatures and pulse voltages: 5°C, +20/−4 V (Figure 1(a)); 5°C, +35/−4 V (Figure 1(b)); 25°C, +20/−4 V (Figure 1(c)); and 25°C, +35/−4 V (Figure 1(d)) for 90 minutes. The insets in Figures 1(a)–1(d) showed cross sections of TiO₂ nanotube arrays. The SEM images demonstrated that the oxide nanotubes formed in a uniform shape under the conditions

of +20/−4 V at both 5 and 25°C, while the nonuniform nanotubes were found for the sample prepared under the conditions of +35/−4 V at both temperatures. The formation of the nonhomogeneous nanotubes (at 35 V) may be because of the high electrical field inducing etching of TiO₂ at higher anodization potential. While the electrochemical oxidation rate was increased at the higher anodization potential, longer tube lengths and formation oxide films were observed (inset of cross sections). At an anodization potential of +20 V, the formation and etching of TiO₂ were slower than those formed at +35 V. Thus, the applied pulse voltage at +20/−4 V in anodization led to the formation of shorter and more uniform nanotube structures than that formed at +35/−4 V.

The wall thickness, tube diameter, and tube length of TiO₂ nanotubes were measured using ImageJ and were plotted as shown in Figure 2. The effects of each anodization parameter on nanotube diameter and wall thickness were summarized in Table 1. The results suggested that temperature and pulse voltage in anodization had a remarkable effect on the TiO₂ tubular features.

Electrolytes containing fluorine are known as the most efficient electrolytes for anodic formation of TiO₂ nanotube arrays. For electrochemical anodization with pulse potential of +20/−4 V or +35/−4 V, TiO₂ nanotube layers were formed

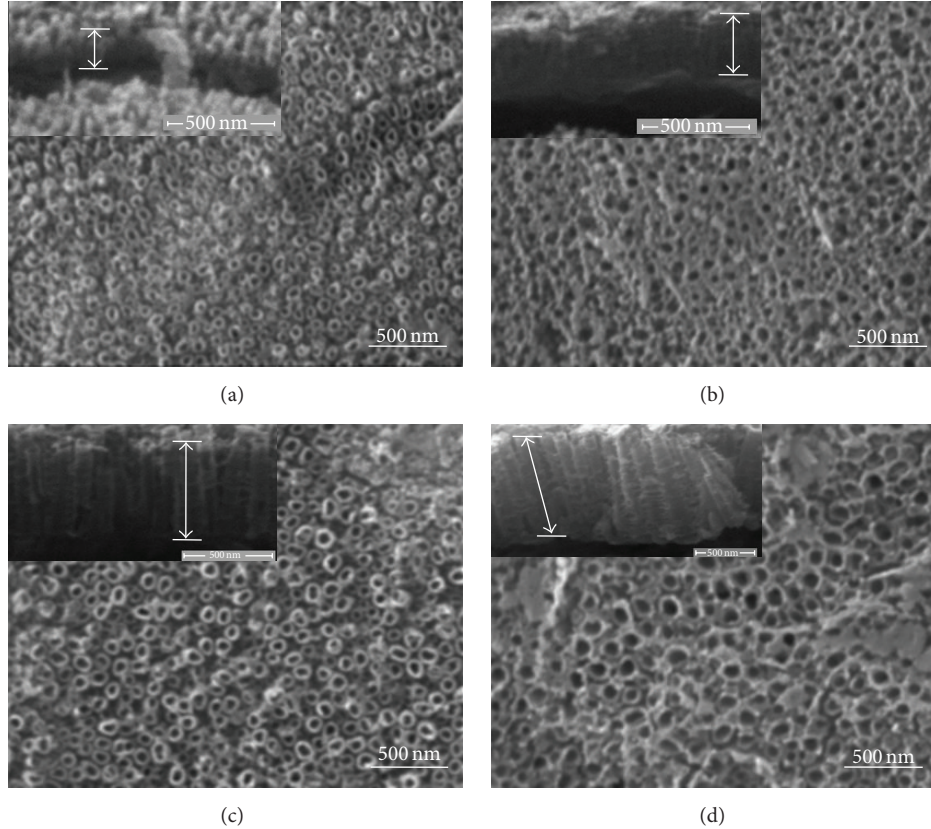
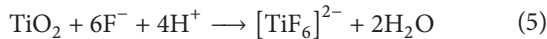
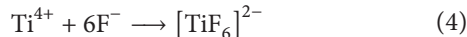
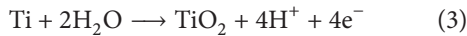
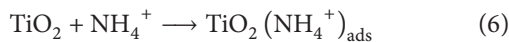


FIGURE 1: FE-SEM images of nanotube arrays anodized at 5°C, +20/-4 V (a); 5°C, +35/-4 V (b); 25°C, +20/-4 V (c); and 25°C, +35/-4 V (d) for 90 minutes. Scale bars are 500 nm. The insets showed cross sections of the anodized TiO₂ films.

by self-organization of TiO₂ as a result of the balance between electrochemical oxidation of Ti and TiO₂ (reaction (3)). The induced electrical field caused dissolution of the TiO₂ by fluoride ions (reactions (4) and (5)) [34, 35]. Dissolution of the TiO₂ was partially suppressed by the binding of NH₄⁺/NH₃ species on the TiO₂ surfaces (reaction (6)) as described by Chanmanee et al. [32]:



Reactions (3) and (5) occur during positive potential, whereas negative voltage electrostatically induces the binding of NH₄⁺ species with TiO₂, as shown in reaction (6), to form adsorbing TiO₂(NH₄⁺). The role of TiO₂(NH₄⁺) is to protect the nanotube walls against chemical etching by fluoride ions even in short times of negative potential (1 sec.) [32, 36–38]:



In the present study, it was found that tube diameter and length of ATi strongly depended on temperature and applied pulse voltage (Figures 1 and 2). Figure 2 showed that nanotube diameter and tube length formed at various temperatures

TABLE 1: The relationship between anodization parameters: (i) increasing the system temperature from 5°C to 25°C and (ii) increasing positive voltages from +20 V to +35 V, with the formation of TiO₂ nanotube arrays in terms of tube width and diameter. “TW” represents tube width, “TD” tube diameter, and “TL” tube length.

Parameter	Morphology
(i) 5°C to 25°C At the same voltage	TW not changed
	TD ↑
	TL ↑
(ii) +20 V to +35 V At the same temperature A constant voltage of -4 V	TW not changed
	TD ↑
	TL ↑

were significantly different with significant level of at least 0.05, while the wall thicknesses were comparable. The result suggested that the rate of TiO₂ formation and chemical dissolution at 25°C were faster than those at 5°C, while the TiO₂ formation rate and etching rate of TiO₂ induced by the electric field were similar at both temperatures [28]. However, at low temperature, etching of TiO₂ by fluoride ions is largely suppressed, leading to small tube diameter and similar wall thickness. The previous study by Wang and Lin found that, at room temperature, the TiO₂ formation rate was higher than that in an ice bath [28], while the etching rate of TiO₂

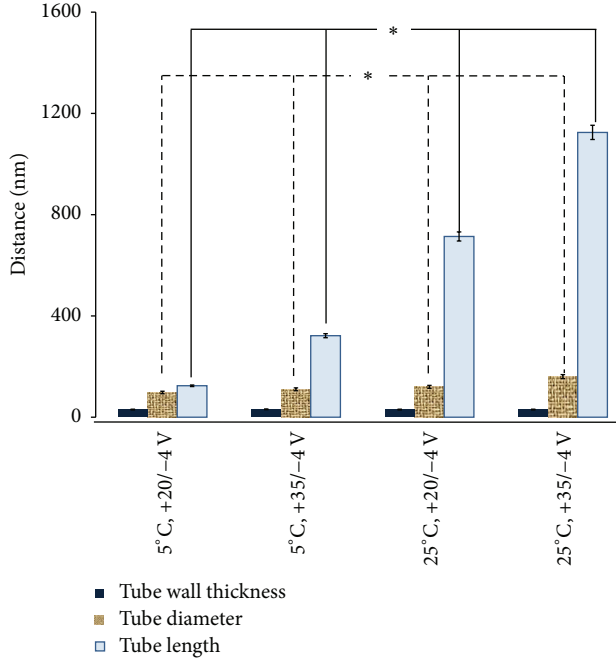


FIGURE 2: Wall thickness, diameter, and length of anodized TiO₂ nanotubes, formed from different conditions of anodization, analyzed by ImageJ. p value was calculated using two-way ANOVA; $n = 3$, * $p < 0.05$.

induced by electric field and fluorine ions remained similar at both temperatures. Their results showed a difference in inner diameter but not in the outer diameters. Their work was conducted in hydrofluoric electrolyte; thus, the anodization was not suppressed by neutral-viscous electrolyte. This phenomenon may be the reason to obtain different result from this present study. However, Wang and Lin also found that, at low temperature ($\sim 0^\circ\text{C}$), even though the potential was increased, the chemical dissolution of TiO₂ by fluorine ions was still very low in the glycerol solution containing 0.25 wt% ammonium fluorides. Therefore, only a small difference in both wall thickness and diameter of the nanotube was observed at a constant temperature [28].

3.2. Hydroxyapatite Electrodeposition

3.2.1. Effect of Alkaline Pretreatment. From the previous work, the sodium titanate (Na₂Ti₅O₁₁ or Na₂Ti₆O₁₃) was deposited on the top of TiO₂ nanotubes and acted as nucleation sites for nanoscale of HA electrodeposition [36]. The SEM images in Figures 3 and 4 showed the HA formation on ATi and P-ATi, respectively. From Figures 3(a)–3(d), without alkaline pretreatment, the HA coatings appeared as an oriented rod-like crystal structure on the ATi substrates with the average HA crystal sizes of 175, 107, 155, and 316 nm, respectively. On the P-ATi substrates, the HA coatings formed as an unoriented rod-like crystal structure with the average HA crystal sizes of 171, 194, 105, and 151 nm, respectively, as shown in Figures 4(a)–4(d). The average size of HA crystal on ATi (107 nm) in Figure 3(b) is smaller than the average HA crystal

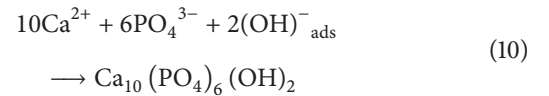
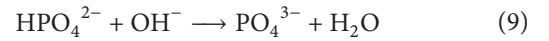
TABLE 2: EDS analysis of HA coating on ATi and conventional Ti represents the ratio of Ca and P. The anodized Ti was performed under various conditions with a constant voltage of -4 V . Data represent mean \pm standard deviation. p value was calculated using ANOVA; $n = 5$, * $p < 0.05$ compared with conventional Ti.

Substrate	The ratio of Ca and P	
	Pretreatment	Without pretreatment
ATi: $5^\circ\text{C}/+20\text{ V}$	1.56*	1.44*
ATi: $5^\circ\text{C}/+35\text{ V}$	1.46*	1.67*
ATi: $25^\circ\text{C}/+20\text{ V}$	1.66*	1.68*
ATi: $25^\circ\text{C}/+35\text{ V}$	1.43*	1.61*
Conventional Ti (control)	0.89	0.97

size on P-ATi (194 nm) in Figure 4(b). In this study, the results confirmed that the HA crystal was finer on ATi (5°C , $+35/-4\text{ V}$) without NaOH pretreatment.

3.2.2. Formation of Hydroxyapatite on Different Substrates. From Table 2, the EDS analysis of HA-ATi and HA-P-ATi revealed that the calcium to phosphate ratios, Ca/P, were in the range of 1.43 to 1.68 when ATi was used as a substrate. The HA on ATi and P-ATi had a Ca/P ratio closely mimicking that of natural bone. The HA coating on conventional Ti, however, had a Ca/P ratio of about 0.9. This ratio is close to that of dicalcium phosphate in bone [17]. The crystal structures of grown calcium phosphate minerals were analyzed by XRD, as shown in Figure 5. The XRD spectra and EDS analysis confirmed that HA (Ca₁₀(PO₄)₆(OH)₂) coating formed on ATi and P-ATi, but perhaps dicalcium phosphate formed on the conventional Ti.

The formation of HA crystals on Ti and ATi by electrodeposition in the solution containing calcium and phosphorus was investigated in the present study. Electrochemical reactions of HA formation are shown as follows [39]:



The reduction of water resulted in the release of H₂ and an increase of hydroxide ions, as shown in reaction (7). As a result of reaction (7) [39], the pH between the cathode and electrolyte interface increases. When pH was higher than 7.64, the rates of the HA electrodeposition of reactions (8) and (9) were accelerated. When the interfacial pH was high, it provided an appropriate chemical environment to form HA, Ca₁₀(PO₄)₆(OH)₂, coatings on the cathode (reaction (10)) [40]. In addition, the electric field draws Ca²⁺ ions to the cathode surface causing that Ca/P ratio is closer to that of natural bone than the Ca/P ratio obtained by conservative methods (precipitation of calcium phosphates from aqueous solution).

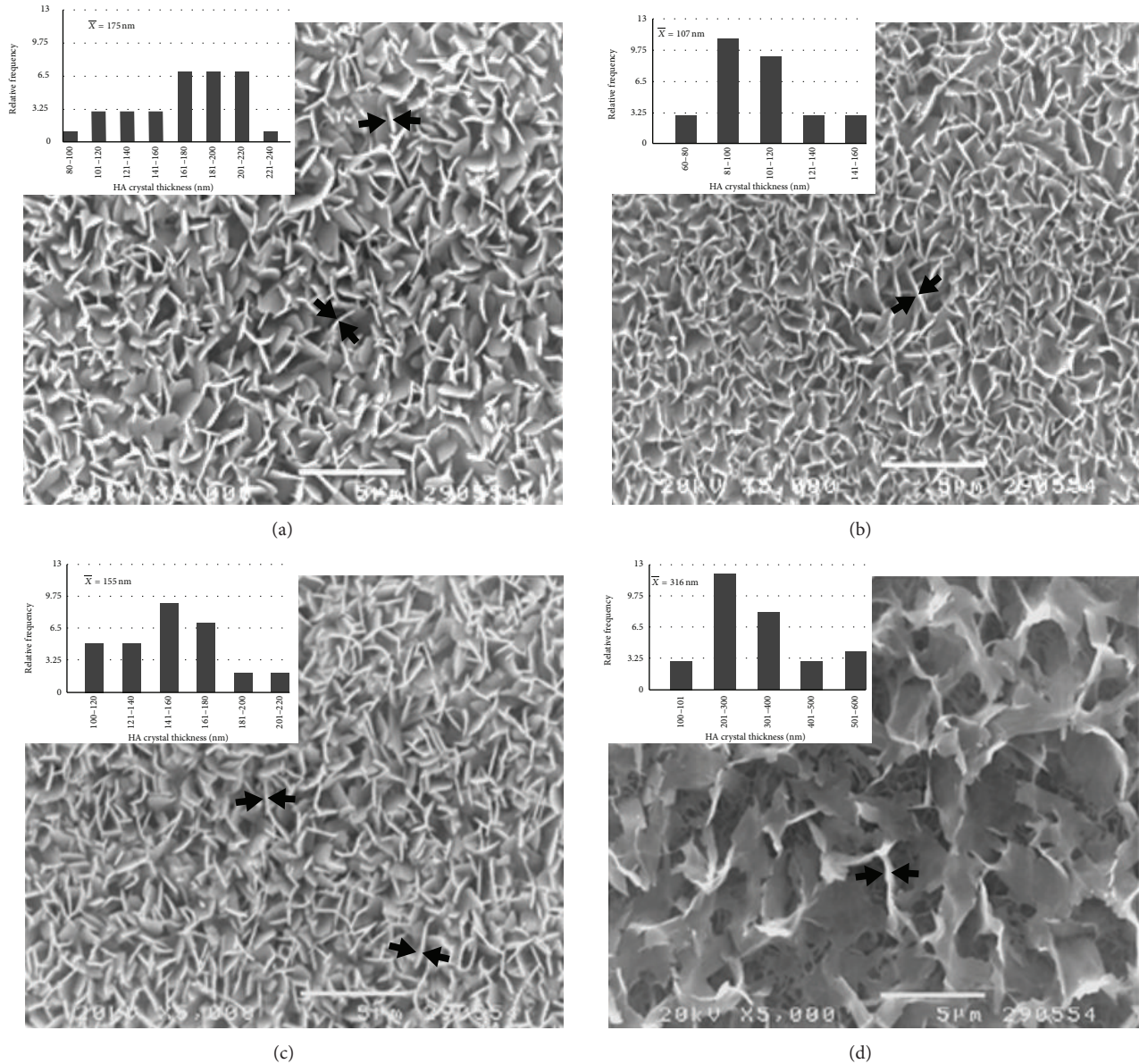


FIGURE 3: SEM images of HA coating on different ATi (without 0.5 M NaOH pretreatment) which were anodized under different conditions: (a) at 5°C, +20/-4 V; (b) at 5°C, +35/-4 V; (c) at 25°C, +20/-4 V; and (d) at 25°C, +35/-4 V for 90 minutes. Scale bars are 5 μm. Black arrows represent HA crystal thickness. Inset graphs are thickness analysis of HA using ImageJ. Data are calculated from three SEM images with $n = 30$.

The results from Figures 3 and 4 and Table 2 suggested that the chemical composition of HA depends on the surface structure of substrates. It was known that it is easier for electrons to travel through TiO₂ nanotubes electrode than through TiO₂ compact layers [34]. Therefore, feature of HA (Ca₁₀(PO₄)₆(OH)₂) coatings on ATi electrode was more orderly oriented than those on conventional Ti because HA layers on ATi possess Ca/P ratios near to that of natural bone due to Ca²⁺ ions enrichment on electrode (reaction (10)). Since ATi sample can carry more OH⁻ groups on its surface during NaOH pretreatment, it supports a very dense formation of apatite nuclei. Another study also found that HA deposition on conventional Ti from the solution containing

Ca²⁺ and PO₄³⁻ could obtain four different kinds of calcium phosphates, including Ca₁₀(PO₄)₆(OH)₂, Ca₂(PO₄)₃ · nH₂O, Ca₈H₂(PO₄)₆ · 5H₂O, and CaHPO₄ · 2H₂O [41].

3.2.3. Mechanical Bonding Strength of Hydroxyapatite on Anodized Titanium. The bond strength between coated HA and the implant material is very important because the adhesive failure of implant after implantation easily takes place when the bond strength is low. Therefore, the present study aimed to study effect of morphology of substrates used for HA coatings on bond strength between them. As shown previously that only nanotube length and tube diameter

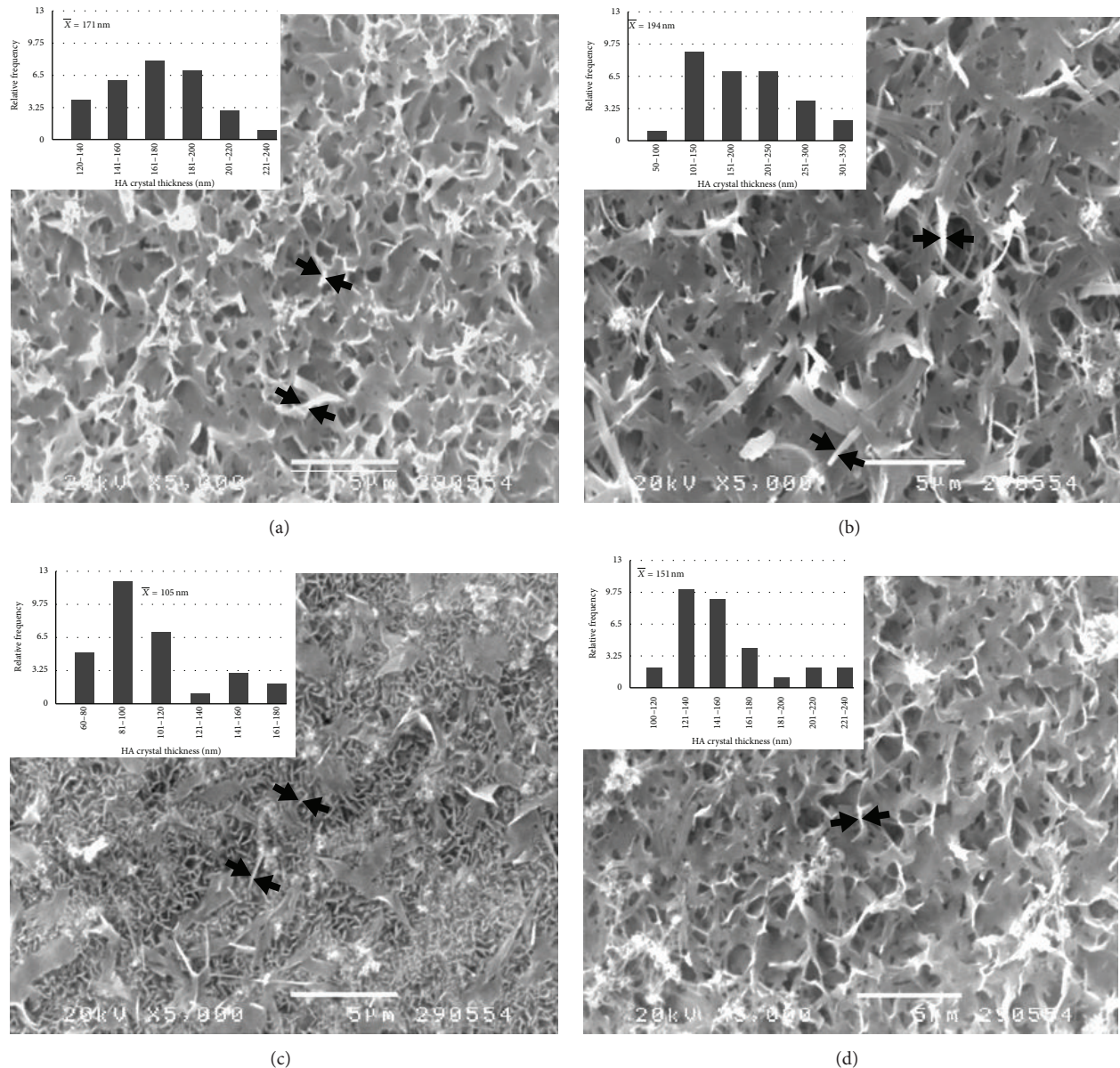


FIGURE 4: SEM images of HA coating on different P-ATi (with 0.5 M NaOH pretreatment) which were anodized under different conditions: (a) at 5°C, +20/-4 V; (b) at 5°C, +35/-4 V; (c) at 25°C, +20/-4 V; and (d) at 25°C, +35/-4 V for 90 minutes. Scale bars are 5 μm. Black arrows represent HA crystal thickness. Inset graphs are thickness analysis of HA using ImageJ. Data are calculated from three SEM images with $n = 30$.

varied with anodization conditions, length (L) to diameter (D) of TiO_2 nanotube was used to test for this effect. Figure 6(a) showed L/D ratio of TiO_2 nanotube arrays for ATi and P-ATi, anodized at the following conditions: 5°C, +20/-4 V, $L/D = 1.27$; 5°C, +35/-4 V, $L/D = 2.92$; 25°C, +20/-4 V, $L/D = 5.96$; and 25°C, +35/-4 V, $L/D = 7.03$. The results suggested that using either higher positive voltage or higher temperature increased L/D ratios. It was found that bonding strength of the HA coating on P-ATi is higher than that of HA-ATi (such that, at 5°C, +35/-4 V with $L/D = 2.92$, found bonding strength of the HA coating on P-ATi is 21 MPa and via ATi is 12 MPa). It is due to the fact that the NaOH pretreatment increases the pH inside the

titania nanopores, consequently, nucleation of HA crystals was enhanced during electrodeposition. As described by Kim et al., during the alkaline treatment, the protective oxide layer on Ti is dissolved into solution because of corrosive attack by hydroxyl groups [42]. Negatively charged hydrates, produced on the ATi substrate surface, combine with alkali ions from the aqueous solution to form a hydrogel layer of sodium titanate. After the hydrogel layer was exposed to high temperature, the layer was dehydrated and was densified to form a stable alkali titanate layer. The compact layer of alkali titanate facilitates good adhesion between the HA coating and Ti or ATi substrate. The bonding strength progressively decreased as L/D increased when L/D was higher than

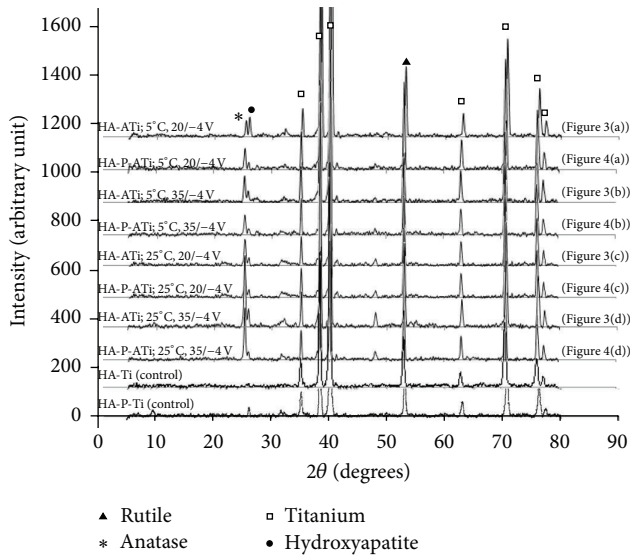


FIGURE 5: X-ray diffraction spectra of the electrodeposited HA coatings on Ti and ATi at the temperatures of 5°C and 25°C and the applied voltages of +20/-4 V and +35/-4 V, with NaOH pretreatment (P) and without NaOH pretreatment.

2.92. At L/D of 2.92, the highest bonding strength between HA and P-ATi was obtained. This phenomenon indicated that nanotube geometry is an important factor effecting on bonding strength between coated HA and substrate.

According to the ASTM F 1044-05 standard, there are three types of failures that can occur during the tensile test: adhesive, cohesive, and a combination of these two modes (Figures 6(b) and 6(c)). For the HA coated at 5°C, +35/-4 V ($L/D = 2.92$), during the shear bond tests, the fracture occurred only at the HA coating layers, as shown in Figure 6(c)(I). Accordingly, it can be stated that cohesion strength between the HA and TiO_2 nanotube was stronger than that between the HA layers. The same fracture surface was found for the deposited HA prepared at 25°C, +20/-4 V ($L/D = 5.96$). For the HA coated at 25°C, +35/-4 V ($L/D = 7.03$), fracture occurred at the HA and TiO_2 interface as well as at the HA layer as shown in Figure 6(c)(II). From Figure 6(c)(II), residues of TiO_2 nanotube were found in both sides of the fracture surface. This failure indicated a combination of adhesive and cohesive failures and also occurred for the HA coated at 5°C, +20/-4 V ($L/D = 1.27$). Using both bonding strength and fracture surface information, the high bonding strength was found when cohesion between HA and TiO_2 nanotube is stronger than adhesion between HA layers. The dependence of bonding strength on L/D ratio may be described as the following. When L/D is 1.27, the depth that deposited HA could form along nanotube is very shallow. As shown in Figure 2, the nanotube length in this case is only about 120 nm. Thus, nanotube surface area, which acts as nucleation site for HA formation, is low, leading to less HA-nanotube interface area. In addition, due to short nanotube length, both the nanotubes and Ti base may be subjected to the glue. Hence, the nanotube base was easily destroyed during testing. For the highest L/D ratio of 7.03, the presence

of nanotube residue indicated that TiO_2 nanotubes were damaged. From Figure 2, tube length was approximately 1120 nm, which is almost four times longer than that of the sample whose L/D ratio is 2.97. In this case, the failure of nanotube could be explained by the Euler equation; $\sigma_{cr} = \pi^2 EI / (AL^2)$ [43]. As shown in the equation, critical stress (σ_{cr}) that the column can bear is inversely proportional to the second order of column height, L . The higher the height of the column, the lower the critical stress that the column can bear. As a result, tube strength of nanotube layer is inversely proportional to nanotube length.

For the sample with L/D ratio of 5.96, the bonding strength is lower and the tube length is about two times higher than that for the sample with L/D ratio of 2.97. The Euler equation may be applied for this case; nevertheless, the fracture surface of the two samples indicated the similar adhesion mode. Further study is needed to analyze the effect of geometry in this range. In case of HA on conventional Ti substrate (Figure 6(c)(III)) fracture during the test occurred at the calcium phosphate-Ti interface, which indicated that only adhesive failure occurred. From these results, it can be concluded that as L/D ratio is approximately 3.00–6.00, the interfacial adhesion between HA and TiO_2 array is stronger than cohesion between HA layers.

In conclusion, the topography and chemical composition of Ti substrates before the electrodeposition of bioinspired HA directly influence the crystal structure and phases as well as mechanical bonding strength of HA coating. Following ISO Standard 13779-4:2002, bonding strength between coating and substrate of apatite coating implant should be higher than 15 MPa [44]. With this result, ATi samples anodized at 5°C and +35/-4 V ($L/D = 2.92$) were further studied for cell morphology and viability with preosteoblasts.

3.2.4. Responses of Preosteoblast Cells on Different Hydroxyapatite Coatings. ATi and P-ATi anodized at +35/-4 V and 5°C, as shown in Figures 3(b) and 4(b), respectively, were chosen for cell culture testing because the mechanical bonding strength of HA on these substrates was high, as shown in Figure 6. Figure 7 shows cell proliferation on Ti, ATi, P-ATi, HA-ATi, and HA-P-ATi. Previously, the samples were seeded with MC3T3-E1 preosteoblast cells and cultured for three days in a standard cell culture condition. The results of the MTT assay indicated that all of the samples had good cytocompatibility. The percentage of viable cells was the highest on HA-ATi. The electrodeposited HA, whose Ca/P ratio is similar to that of natural bone, exhibited the oriented rod-like crystal structure when it formed on ATi with an average crystal size of 107 nm. The results suggested that osteoblasts preferred to grow on HA-ATi compared to HA-P-ATi, whose average crystal size was larger, 194 nm. This result is in an agreement with other works [6, 23, 45]. Webster and Ejiro suggested that a small HA crystal size improved the biocompatibility of implants and increases osteoblast adhesion [23]. Tsuchiya et al. reported that nanostructured materials significantly improved osteoblast growth while they inhibited cell apoptosis [6]. Moreover, the nanostructure of biomaterials promoted cell functions, such as the synthesis of extracellular

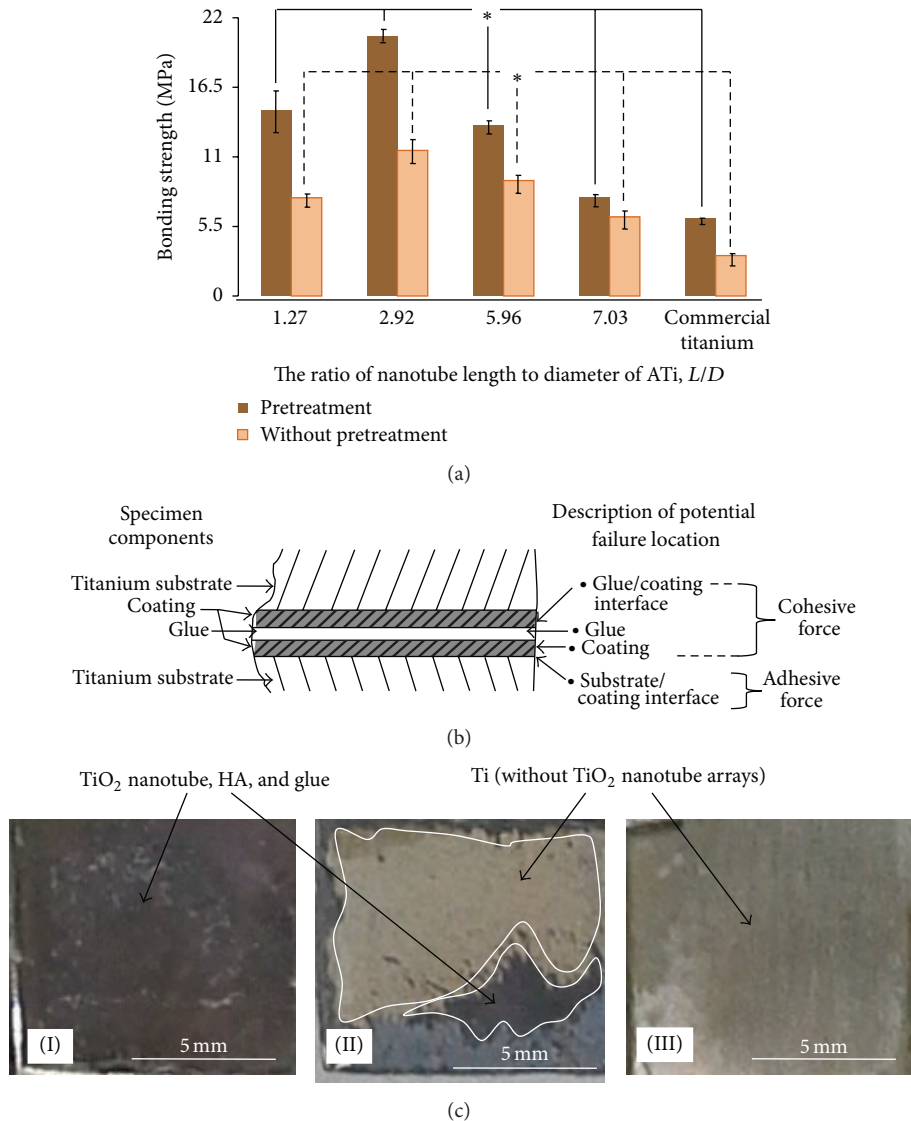


FIGURE 6: (a) Bonding strengths of HA coating on Ti, ATi, and P-ATi (with 0.5 M NaOH pretreatment). p value was calculated using one-way ANOVA; $n = 3$, $*p < 0.05$. (b) Nomenclature of specimen components and classification of failure location for the shear testing. (c) Light microscopy images of three types of failure for the tensile testing (HA coating on 5°C, +35/-4 V ATi; HA coating on 25°C, +20/-4 V ATi and Ti): (I) cohesive, (II) combination of cohesive and adhesive, and (III) adhesive force.

matrix proteins and calcium mineral deposition [45]. Thus, the size of the HA crystals formed on ATi and P-ATi directly affects osteoblast proliferation in this study.

Adhesion of osteoblast cells is a crucial prerequisite to all subsequent cell functions. According to Webster et al., the use of nanostructured ceramics (such as alumina, titania, and HA) significantly improved osteoblast adhesion [46, 47]. Importantly, the results shown in Figure 7 are in good agreement with previous findings that finer HA crystals improve cell proliferation. A study by Chou et al. demonstrated that small plate-like HA had greater preosteoblast proliferation after 4 days than large plate-like HA. Large plate-like HA, however, induced higher expression of the mature osteogenic markers osteocalcin and bone sialoprotein in preosteoblasts after 21 days of culture compared to small plate-like HA,

polystyrene, and conventional apatite [48]. Further studies are needed to confirm its effects on osteoblast differentiation and new bone formation juxtaposed to orthopedic implants.

Figures 7(b)–7(f) show that osteoblasts differed in their size, spreading, and adhesion on the samples. Figure 7(a) shows that although Ti is a biocompatible material, it is a bioinert material, which does not adequately increase osteoblast attachment, spreading, proliferation, or differentiation. In contrast, HA, as a major inorganic component of hard tissues, possesses excellent biocompatibility, bioactivity, and osteoconductivity [49]. Cells exhibited larger spreading on Ti than on all other samples, but cell peeling was observed due to the lower cell adhesion. Particularly noteworthy are HA-ATi and HA-P-ATi, which induced maximum cell adhesion with a smaller cell size. Cells appeared flattened and spread

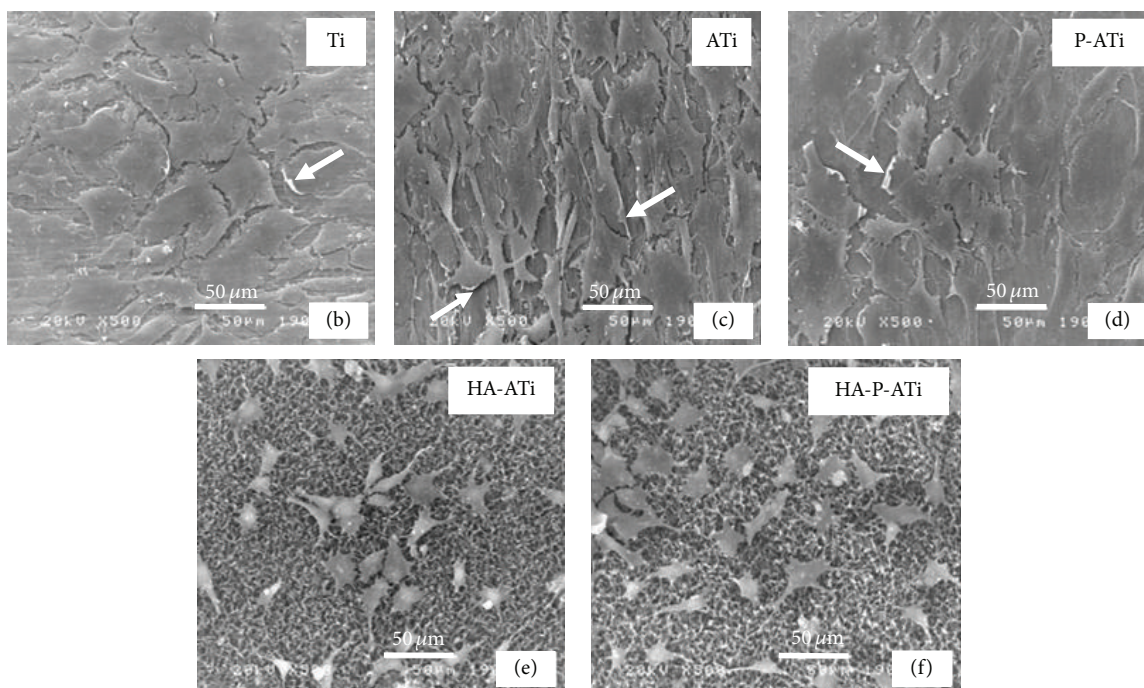
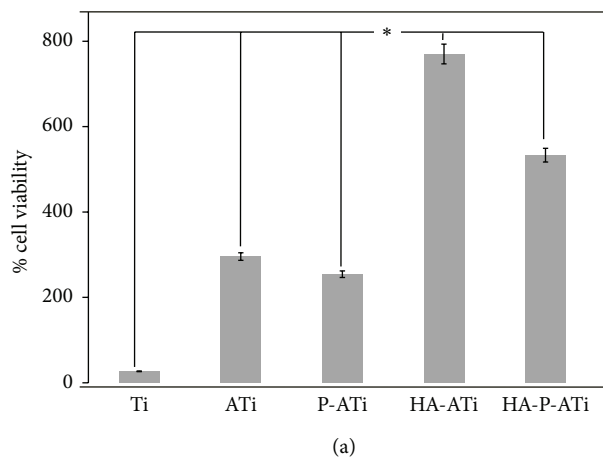


FIGURE 7: (a) Cell viability of MC3T3-E1 preosteoblasts on Ti, ATi, P-ATi, HA-ATi, and HA-P-ATi after three days of cultures. Data are mean \pm a standard error of mean. p value was calculated using one-way ANOVA; $n = 3$, $*p < 0.05$. SEM images of MC3T3-E1 preosteoblasts after three days of incubation on (b) conventional Ti, (c) ATi, (d) P-ATi, (e) HA-ATi, and (f) HA-P-ATi. Arrows show peeling areas of MC3T3-E1 cells from the substrates.

more widely on Ti, ATi, and P-ATi samples (Figures 7(b)–7(d)) than on the HA-coated samples (Figures 7(e) and 7(f)). Osteoblasts with no appendix on their substrates and cell peeling were observed on Ti, ATi, and P-ATi (Figures 7(b)–7(d)). This is perhaps due to the fact that the cell adhesion strength on the non-HA-coated samples was lower than that on HA-ATi and HA-P-ATi. HA improves osteoblast adhesion because it is a main component of the bone extracellular matrix. The HA coating reduced osteoblast spreading but improved the elongation of cell projections.

The effect of NaOH pretreatment on cell viability was also examined. Cell morphology of preosteoblasts on the ATi and P-ATi was similar (Figure 7). The ATi (without NaOH pretreatment), however, was more favorable for preosteoblast

proliferation than P-ATi, possibly due to their different surface compositions. Sodium titanate was present on the P-ATi surface but not on the ATi surface. HA-P-ATi has a lower ratio of Ca/P (1.46) and an unoriented rod-like crystal HA coating (Figure 4(b)), while HA on ATi has a Ca/P of 1.67 and an oriented rod-like crystal structure. The percentage of viable cells after 3 days of culture was greater on HA-ATi than on HA-P-ATi, but the cell morphology of preosteoblasts on HA-ATi was similar to that on HA-P-ATi. A previous study suggested that osteoblast adhesion and metabolic activity were very sensitive to surface morphology and roughness [50]. Surface energy is also reported to be an influential surface characteristic on cellular proliferation [51]. Therefore, the higher cell viability on nanoscale HA-ATi could be due to

the positive effects of the surface energy. Moreover, HA with low crystallinity may remarkably increase degradation rates *in vitro* or *in vivo* [49]. HA is the most stable and least soluble in aqueous media of all calcium phosphates [52]. It becomes more acidic and water-soluble as its Ca/P ratio decreases [53]. Thus, the dissolution of HA in HA-P-ATi may slow the growth of preosteoblast cells. Approximately 2–4 mM of Ca^{2+} is suitable for osteoblast proliferation and survival, and slightly higher concentrations (6–8 mM) favor osteoblast differentiation and mineralization. An excessively high concentration, >10 mM, can be cytotoxic to cells [54]. It is possible that the high concentration of Ca^{2+} in HA-P-ATi decreased preosteoblast proliferation in this study. On the other hand, with a higher Ca/P ratio (1.67) of HA-P-ATi, free phosphate level in the apatite microenvironment is also perhaps lower, and thus fewer phosphates participating in osteopontin regulation are transported into the cells [55]. This can cause lower cell proliferation on HA-P-ATi than on HA-ATi after 3 days of culture. Another possible mechanism is that high phosphate levels may induce the expression of calcium channels and phosphate transporters and activation of ERK1/2, but not MAPK, p38, or JNK signaling pathways [56]. This cascade participates in the regulation of a large variety of processes, including cell adhesion, cell cycle progression, cell migration, cell survival, differentiation, metabolism, proliferation, and transcription [57]. Therefore, we conclude that the size and Ca/P ratio of the HA crystal directly affect the cell proliferation, but not the cell morphology, of preosteoblasts.

Importantly, the nanotube formation of TiO_2 is the predominant factor to increase the bonding strength between the HA coating and TiO_2 nanotube substrate. The nanotube formation can promote a HA coating in the phase closely mimicking that found in natural bone. Therefore, the electrodeposited HA coating on ATi and P-ATi can illicit more favorable responses of preosteoblast morphology and proliferation than the samples without HA coating.

4. Conclusions

TiO_2 nanotube arrays were anodized for 90 min under various conditions: 5°C, +20/−4 V; 5°C, +35/−4 V; 25°C, +20/−4 V; and 25°C, +35/−4 V. HA was then electrodeposited onto ATi and P-ATi (with NaOH pretreatment). Increasing the pulse-positive voltage (from +20 V to +35 V) and temperature (from 5°C to 25°C) during anodization increased the nanotube length. At 25°C, changing the anodization voltage did not significantly affect the nanotube wall thickness. The bonding strength of the HA coatings on ATi layers was stronger than that of the HA coating on conventional Ti. Importantly, the bonding strength of the HA coating was higher on HA-P-ATi than on HA-Ti and HA-ATi. The results suggested that the HA crystals on ATi had an oriented rod-like crystal structure with an average size of 107 nm and a Ca/P ratio of 1.67. The HA crystals on P-ATi had an unoriented rod-like structure with an average size of 194 nm and Ca/P ratio of 1.46. The percentage of osteoblast viability at day 3 of cell culture was significantly higher on HA-P-ATi (98%) than those on Ti (59%) and P-ATi (92%) but lower

than those on ATi (108%) and HA-ATi (117%). Higher cell proliferation was observed on the smaller HA crystals of HA-ATi. The Ca/P ratio (1.67) of the HA crystals on ATi reduced the dissolution of calcium ions and phosphates, thus allowing for better cell proliferation. The electrodeposited HA coating improved preosteoblast adhesion as cell projections were elongated. In summary, P-ATi increases the mechanical bonding strength of an electrodeposited HA coating but decreases the Ca/P ratio of HA with a larger crystal size, thus leading to lower preosteoblast proliferation after 3 days of culture.

Competing Interests

The authors declare that there are no competing interests regarding the publication of this paper.

Acknowledgments

The authors would like to acknowledge financial supports from Commission on Higher Education (the Faculty Development Scholarships) and a Research Strengthening Project of the Faculty of Engineering, King Mongkut's University of Technology Thonburi, Bangkok, Thailand. They also thank Associate Professor Dr. P. Kajitvichyanukul, Associate Professor Dr. K. Pasuwat, Mr. C. Manussapol, Mr. C. Jongwanasiri, and Ms. K. Siruksasin for their contributions and useful advice in this study; Dr. W. Chanmanee for his advice in anodization; and Ms. W. Chokevivat from National Metal and Materials Technology Center for her help in animal cell experiments. They acknowledge Dr. Carmen V. Gaines (Ph.D.) and Mr. Cristian Guajardo for her and his useful discussion.

References

- [1] S. Ramakrishna, J. Mayer, E. Wintermantel, and K. W. Leong, "Biomedical applications of polymer-composite materials: a review," *Composites Science and Technology*, vol. 61, no. 9, pp. 1189–1224, 2001.
- [2] J. B. Park and J. D. Bronzino, *Biomaterials: Principles and Applications*, CRC Press, Boca Raton, Fla, USA, 2003.
- [3] M. J. Olszta, X. Cheng, S. S. Jee et al., "Bone structure and formation: a new perspective," *Materials Science and Engineering R: Reports*, vol. 58, no. 3–5, pp. 77–116, 2007.
- [4] R. S. Park and J. B. Lakes, *Biomaterials: An Introduction*, Plenum Press, New York, NY, USA, 1992.
- [5] P. Li and P. Ducheyne, "Quasi-biological apatite film induced by titanium in a simulated body fluid," *Journal of Biomedical Materials Research*, vol. 41, no. 3, pp. 341–348, 1998.
- [6] H. Tsuchiya, J. M. Macak, L. Müller et al., "Hydroxyapatite growth on anodic TiO_2 nanotubes," *Journal of Biomedical Materials Research—Part A*, vol. 77, no. 3, pp. 534–541, 2006.
- [7] G. Balasundaram and T. J. Webster, "A perspective on nanophase materials for orthopedic implant applications," *Journal of Materials Chemistry*, vol. 16, no. 38, pp. 3737–3745, 2006.
- [8] M. S. Johnsson and G. H. Nancollas, "The role of brushite and octacalcium phosphate in apatite formation," *Critical Reviews in Oral Biology & Medicine*, vol. 3, pp. 61–82, 1992.

- [9] T. Kokubo, T. Matsushita, and H. Takadama, "Titania-based bioactive materials," *Journal of the European Ceramic Society*, vol. 27, no. 2-3, pp. 1553–1558, 2007.
- [10] A. R. Boccaccini, J. Cho, T. Subhani, C. Kaya, and F. Kaya, "Electrophoretic deposition of carbon nanotube-ceramic nanocomposites," *Journal of the European Ceramic Society*, vol. 30, no. 5, pp. 1115–1129, 2010.
- [11] J. D. Haman, L. C. Lucas, and D. Crawmer, "Characterization of high velocity oxy-fuel combustion sprayed hydroxyapatite," *Biomaterials*, vol. 16, no. 3, pp. 229–237, 1995.
- [12] H. Hero, H. Wie, R. B. Jorgensen, and I. E. Ruyter, "Hydroxyapatite coatings on Ti produced by hot isostatic pressing," *Journal of Biomedical Materials Research*, vol. 28, no. 3, pp. 343–348, 1994.
- [13] R. Hu, C.-J. Lin, and H.-Y. Shi, "A novel ordered nano hydroxyapatite coating electrochemically deposited on titanium substrate," *Journal of Biomedical Materials Research Part A*, vol. 80, no. 3, pp. 687–692, 2007.
- [14] A. Montenero, G. Gnappi, F. Ferrari et al., "Sol-gel derived hydroxyapatite coatings on titanium substrate," *Journal of Materials Science*, vol. 35, no. 11, pp. 2791–2797, 2000.
- [15] V. Nelea, C. Ristoscu, C. Chiritescu et al., "Pulsed laser deposition of hydroxyapatite thin films on Ti-5Al-2.5Fe substrates with and without buffer layers," *Applied Surface Science*, vol. 168, no. 1–4, pp. 127–131, 2000.
- [16] Y. C. Tsui, C. Doyle, and T. W. Clyne, "Plasma sprayed hydroxyapatite coatings on titanium substrates part 2: optimisation of coating properties," *Biomaterials*, vol. 19, no. 22, pp. 2031–2043, 1998.
- [17] X. Zhu, D. W. Son, J. L. Ong, and K. Kim, "Characterization of hydrothermally treated anodic oxides containing Ca and P on titanium," *Journal of Materials Science: Materials in Medicine*, vol. 14, no. 7, pp. 629–634, 2003.
- [18] R. Rodriguez, K. Kim, and J. L. Ong, "In vitro osteoblast response to anodized titanium and anodized titanium followed by hydrothermal treatment," *Journal of Biomedical Materials Research Part A*, vol. 65, no. 3, pp. 352–358, 2003.
- [19] K. De Groot, R. Geesink, C. P. A. T. Klein, and P. Serekian, "Plasma sprayed coatings of hydroxyapatite," *Journal of Biomedical Materials Research*, vol. 21, no. 12, pp. 1375–1381, 1987.
- [20] H. Kurzweg, R. B. Heimann, and T. Troczynski, "Adhesion of thermally sprayed hydroxyapatite-bond-coat systems measured by a novel peel test," *Journal of Materials Science Materials in Medicine*, vol. 9, no. 1, pp. 9–16, 1998.
- [21] C.-M. Lin and S.-K. Yen, "Characterization and bond strength of electrolytic HA/TiO₂ double layers for orthopedic applications," *Journal of Materials Science: Materials in Medicine*, vol. 15, no. 11, pp. 1237–1246, 2004.
- [22] R. McPherson, N. Gane, and T. J. Bastow, "Structural characterization of plasma-sprayed hydroxyapatite coatings," *Journal of Materials Science: Materials in Medicine*, vol. 6, no. 6, pp. 327–334, 1995.
- [23] T. J. Webster and J. U. Ejirofor, "Increased osteoblast adhesion on nanophase metals: Ti, Ti6Al4V, and CoCrMo," *Biomaterials*, vol. 25, no. 19, pp. 4731–4739, 2004.
- [24] B. B. Lakshmi, C. J. Patrissi, and C. R. Martin, "Sol-gel template synthesis of semiconductor oxide micro- and nanostructures," *Chemistry of Materials*, vol. 9, no. 11, pp. 2544–2550, 1997.
- [25] Z. Miao, D. Xu, J. Ouyang, G. Guo, X. Zhao, and Y. Tang, "Electrochemically induced sol-gel preparation of single-crystalline TiO₂ nanowires," *Nano Letters*, vol. 2, no. 7, pp. 717–720, 2002.
- [26] D. Gong, C. A. Grimes, O. K. Varghese et al., "Titanium oxide nanotube arrays prepared by anodic oxidation," *Journal of Materials Research*, vol. 16, no. 12, pp. 3331–3334, 2001.
- [27] L.-K. Tsui and G. Zangari, "Water content in the anodization electrolyte affects the electrochemical and electronic transport properties of TiO₂ nanotubes: a study by electrochemical impedance spectroscopy," *Electrochimica Acta*, vol. 121, pp. 203–209, 2014.
- [28] J. Wang and Z. Lin, "Anodic formation of ordered TiO₂ nanotube arrays: effects of electrolyte temperature and anodization potential," *The Journal of Physical Chemistry C*, vol. 113, no. 10, pp. 4026–4030, 2009.
- [29] A. Kar, K. S. Raja, and M. Misra, "Electrodeposition of hydroxyapatite onto nanotubular TiO₂ for implant applications," *Surface and Coatings Technology*, vol. 201, no. 6, pp. 3723–3731, 2006.
- [30] H.-M. Kim, H. Kaneko, M. Kawashita, T. Kokubo, and T. Nakamura, "Mechanism of apatite formation on anodically oxidized titanium metal in simulated body fluid," *Key Engineering Materials*, vol. 254–256, pp. 741–744, 2004.
- [31] H.-M. Kim, T. Himeno, M. Kawashita, J.-H. Lee, T. Kokubo, and T. Nakamura, "Surface potential change in bioactive titanium metal during the process of apatite formation in simulated body fluid," *Journal of Biomedical Materials Research Part A*, vol. 67, no. 4, pp. 1305–1309, 2003.
- [32] W. Chanmanee, A. Watcharenwong, C. R. Chenthamarakshan, P. Kajitvichyanukul, N. R. de Tacconi, and K. Rajeshwar, "Titania nanotubes from pulse anodization of titanium foils," *Electrochemistry Communications*, vol. 9, no. 8, pp. 2145–2149, 2007.
- [33] ASTM International, "Standard test method for shear testing of calcium phosphate coatings and metallic coatings," ASTM F1044-05, ASTM International, West Conshohocken, Pa, USA, 2005, <http://www.astm.org>.
- [34] A. Ghicov and P. Schmuki, "Self-ordering electrochemistry: a review on growth and functionality of TiO₂ nanotubes and other self-aligned MO_x structures," *Chemical Communications*, no. 20, pp. 2791–2808, 2009.
- [35] P. Roy, S. Berger, and P. Schmuki, "TiO₂ nanotubes: synthesis and applications," *Angewandte Chemie-International Edition*, vol. 50, no. 13, pp. 2904–2939, 2011.
- [36] Y. Parcharoen, P. Kajitvichyanukul, S. Sirivisoot, and P. Termsuksawad, "Hydroxyapatite electrodeposition on anodized titanium nanotubes for orthopedic applications," *Applied Surface Science*, vol. 311, pp. 54–61, 2014.
- [37] R. M. Pittman and A. T. Bell, "Raman investigations of NH₃ adsorption on TiO₂, Nb₂O₅, and Nb₂O₅/TiO₂," *Catalysis Letters*, vol. 24, no. 1-2, pp. 1–13, 1994.
- [38] J. Ahdjoudj and C. Minot, "Adsorption of H₂O on metal oxides: a periodic ab-initio investigation," *Surface Science*, vol. 402-404, pp. 104–109, 1998.
- [39] Y.-M. Liao, Z.-D. Feng, and S.-W. Li, "Preparation and characterization of hydroxyapatite coatings on human enamel by electrodeposition," *Thin Solid Films*, vol. 516, no. 18, pp. 6145–6150, 2008.
- [40] J. M. Zhang, C. J. Lin, Z. D. Feng, and Z. W. Tian, "Mechanistic studies of electrodeposition for bioceramic coatings of calcium phosphates by an in situ pH-microsensor technique," *Journal of Electroanalytical Chemistry*, vol. 452, no. 2, pp. 235–240, 1998.
- [41] G. H. Nancollas and B. Tomažič, "Growth of calcium phosphate on hydroxyapatite crystals. Effect of supersaturation and ionic

- medium," *The Journal of Physical Chemistry*, vol. 78, no. 22, pp. 2218–2225, 1974.
- [42] H.-M. Kim, F. Miyaji, T. Kokubo, and T. Nakamura, "Preparation of bioactive Ti and its alloys via simple chemical surface treatment," *Journal of Biomedical Materials Research*, vol. 32, no. 3, pp. 409–417, 1996.
- [43] B. I. Jakobson, M. P. Campbell, C. J. Brabec, and J. Bernholc, "High strain rate fracture and C-chain unraveling in carbon nanotubes," *Computational Materials Science*, vol. 8, no. 4, pp. 341–348, 1997.
- [44] ISO, "Implants for surgery (Hydroxyapatite) Part 4: determination of coating adhesion strength," Tech. Rep. ISO/CD 13779-4, The International Organization for Standardisation, Geneva, Switzerland, 2002, <http://www.iso.org>.
- [45] K. C. Papat, L. Leoni, C. A. Grimes, and T. A. Desai, "Influence of engineered titania nanotubular surfaces on bone cells," *Biomaterials*, vol. 28, no. 21, pp. 3188–3197, 2007.
- [46] T. J. Webster, C. Ergun, R. H. Doremus, R. W. Siegel, and R. Bizios, "Enhanced functions of osteoblasts on nanophase ceramics," *Biomaterials*, vol. 21, no. 17, pp. 1803–1810, 2000.
- [47] T. J. Webster, L. S. Schadler, R. W. Siegel, and R. Bizios, "Mechanisms of enhanced osteoblast adhesion on nanophase alumina involve vitronectin," *Tissue Engineering*, vol. 7, no. 3, pp. 291–301, 2001.
- [48] Y.-F. Chou, W. Huang, J. C. Y. Dunn, T. A. Miller, and B. M. Wu, "The effect of biomimetic apatite structure on osteoblast viability, proliferation, and gene expression," *Biomaterials*, vol. 26, no. 3, pp. 285–295, 2005.
- [49] W. Chen, B. Tian, Y. Lei, Q.-F. Ke, Z.-A. Zhu, and Y.-P. Guo, "Hydroxyapatite coatings with oriented nanoplate and nanorod arrays: fabrication, morphology, cytocompatibility and osteogenic differentiation," *Materials Science and Engineering: C*, vol. 67, pp. 395–408, 2016.
- [50] N. Ribeiro, S. R. Sousa, and F. J. Monteiro, "Influence of crystallite size of nanophased hydroxyapatite on fibronectin and osteonectin adsorption and on MC3T3-E1 osteoblast adhesion and morphology," *Journal of Colloid and Interface Science*, vol. 351, no. 2, pp. 398–406, 2010.
- [51] B. Feng, J. Weng, B. C. Yang, S. X. Qu, and X. D. Zhang, "Characterization of surface oxide films on titanium and adhesion of osteoblast," *Biomaterials*, vol. 24, no. 25, pp. 4663–4670, 2003.
- [52] J. C. Elliott, *Structure and Chemistry of the Apatites and Other Calcium Orthophosphates*, vol. 18 of *Studies in Inorganic Chemistry*, Elsevier, Amsterdam, The Netherlands, 2003.
- [53] V. Nelea, I. N. Mihailescu, and M. Jelínek, "Biomaterials: new issues and breakthroughs for biomedical applications," in *Pulsed Laser Deposition of Thin Films: Applications-Led Growth of Functional Materials*, R. Eason, Ed., chapter 18, John Wiley & Sons, Hoboken, NJ, USA, 2006.
- [54] S. Maeno, Y. Niki, H. Matsumoto et al., "The effect of calcium ion concentration on osteoblast viability, proliferation and differentiation in monolayer and 3D culture," *Biomaterials*, vol. 26, no. 23, pp. 4847–4855, 2005.
- [55] G. R. Beck Jr., E. C. Sullivan, E. Moran, and B. Zerler, "Relationship between alkaline phosphatase levels, osteopontin expression, and mineralization in differentiating MC3T3-E1 osteoblasts," *Journal of Cellular Biochemistry*, vol. 68, no. 2, pp. 269–280, 1998.
- [56] G. R. Beck Jr., "Inorganic phosphate as a signaling molecule in osteoblast differentiation," *Journal of Cellular Biochemistry*, vol. 90, no. 2, pp. 234–243, 2003.
- [57] R. Roskoski Jr., "ERK1/2 MAP kinases: structure, function, and regulation," *Pharmacological Research*, vol. 66, no. 2, pp. 105–143, 2012.

Review Article

Characterization of Inter- and Intramolecular Interactions of Amyloid Fibrils by AFM-Based Single-Molecule Force Spectroscopy

Yinli Li,^{1,2} Hao Liang,¹ Huiling Zhao,^{1,2} Dong Chen,¹ Bo Liu,¹ Thomas Fuhs,² and Mingdong Dong²

¹Institute of Photo-Biophysics, School of Physics and Electronics, Henan University, Kaifeng, 475004 Henan, China

²Interdisciplinary Nanoscience Center (iNANO), Aarhus University, 8000 Aarhus C, Denmark

Correspondence should be addressed to Bo Liu; boliu@henu.edu.cn and Mingdong Dong; dong@inano.au.dk

Received 1 February 2016; Revised 9 June 2016; Accepted 15 June 2016

Academic Editor: Meiyong Liao

Copyright © 2016 Yinli Li et al. This is an open access article distributed under the Creative Commons Attribution License, which permits unrestricted use, distribution, and reproduction in any medium, provided the original work is properly cited.

Amyloids are fibrous protein aggregates defined by shared specific structural features. Abnormal accumulation of amyloid in organs leads to amyloidosis, which results in various neurodegenerative diseases. Atomic force microscopy (AFM) has proven to be an excellent tool investigating amyloids; it has been extensively utilized to characterize its morphology, assembly process, and mechanical properties. This review summarizes studies which applied AFM to detect the inter- and intramolecular interactions of amyloid fibrils and classified the influencing factors of amyloid's nanomechanics in detail. The characteristics of amyloid fibrils driven by inter- and intramolecular interactions, including various morphologies of amyloid fibrils, self-assembly process, and the aggregating pathway, are described. Successful examples where AFM provided abundant information about inter- and intramolecular interactions of amyloid fibrils in different environments are presented. Direct force measurement of intra- or intermolecular interactions utilizing an AFM-based tool, single-molecular force spectroscopy (SMFS), is introduced. Some mechanical information such as elasticity, adhesiveness, and strength was obtained by stretching amyloid fibrils. This review helps researchers in understanding the mechanism of amyloidogenesis and exploring the properties of amyloid using AFM techniques.

1. Introduction

Improper aggregation of polypeptide fragments may result in various neurological disorder diseases [1], such as Alzheimer's disease ($A\beta$ aggregation) [2–5], Parkinson's disease [6], Huntington's disease (Huntington aggregation) [7, 8], prion disease (PrP aggregation) [9], and amyotrophic lateral sclerosis (ALS) [10]. Amyloid aggregations are also found in type II diabetes (islet amyloid polypeptide) [11–14] and dialysis related amyloidosis (β -2 microglobulin aggregation) [6]. Recently, more and more studies have suggested that these diseases are related to the aggregations formed by amyloids sharing specific structural traits. Single soluble amyloid proteins start to interact with each other, and these intermolecular interactions finally assemble the soluble amyloid into various insoluble forms. In addition, a great variety of heterogeneous morphologies detected in self-assembly processes

indicate different assembly pathways of amyloid fibrils [15–17]. As a whole, their assembly pathways can be simply described as soluble protein \rightarrow nucleation \rightarrow fibrillar elongation/lateral aggregation \rightarrow mature network [18]. Though multiple amyloids have been widely explored in recent years, their pathogenic mechanism has not been elucidated clearly.

Atomic force microscopy (AFM) is an excellent tool which has been used extensively to study the fibrillar ultrastructures. AFM enables us to clearly visualize individual biological macromolecules at the nanometer scale [19–23]. Time-lapse AFM imaging [24] has been successfully adopted to monitor the growth of individual peptide fibrils and to characterize the influence of the chemical environment on amyloid aggregation [25]. AFM-based single-molecule force spectroscopy (SMFS) [26] has made force measurement at the single-molecule level with pico-Newton (pN) force resolution possible. This technique enables researchers to analyze

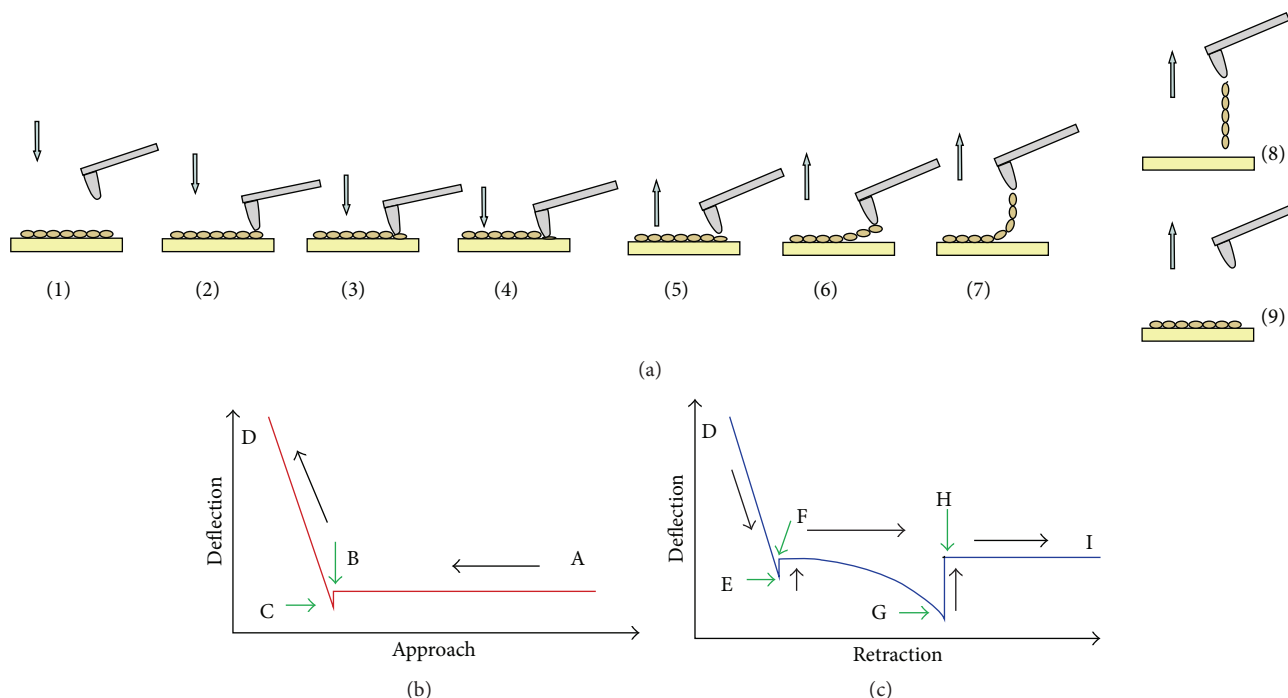


FIGURE 1: (a) Schematic principle of single-molecule force microscopy, (b) approaching force curve, and (c) retracting force curve. In the schematic of Figure (a), (1)–(4) show the approaching progress. (1) AFM tip moves forward to sample. (2) AFM tip contacts sample surface. (3) AFM tip indents sample. (4) AFM tip reaches the defined deflection value; (6)–(9) show the retracting progress, molecules firstly adsorb on AFM tip and then are gradually pulled away from substrate and finally rupture from substrate or from AFM tip.

inter- and intramolecular interactions [27, 28]. The obtained mechanical fingerprint [29] of amyloid fibrils has proven that SMFS is an efficient tool to explore the mechanisms of amyloid assembly process, the differences of various amyloids, and the mechanisms of interactions with chemicals and chaperones.

We review AFM techniques applied to characterize and understand the assembly process of amyloid fibrils involved in pathogenic disorders. We summarized AFM studies of amyloid fibrillogenesis focusing on the morphology, kinetics, and models of amyloid self-assembly. The investigation of the inter- or intramolecular interaction of amyloid fibrils using AFM-based SMFS was reviewed to explore the assembly mechanism and mechanical properties of various shaped fibrils, such as globular oligomers, protofibrils, mature intertwined fibrils, and network structures.

2. Principle of AFM-Based SMFS

AFM is a type of Scanning Probe Microscope (SPM) [65] with high-resolution, and now it has become one of the foremost tools in imaging, measuring, and manipulating matter at nanoscale [66–69]. AFM allows imaging both in ambient and in liquid environments which is of great importance for biological molecules [70–73]. AFM-based SMFS stands out among various single-molecule techniques [74–77] because of its high detection rate, easy operation, and wide application in measuring weak inter- or intramolecule interactions [78–80]. Through SMFS technique, multiple properties, such as

elasticity and viscosity [81], can be analyzed in detail. At the same time, SMFS is analytic technique applied not only to measure mechanical properties of various proteins but also to manipulate single-molecule at pico-Newton scale [78], for example, probing the helical structure, unfolding β -fold structure [64], and measuring intermolecular interactions.

Compared with simple topographic characterization, the AFM-based single-molecule force spectroscopy is more complex [26]. SMFS measurement is based on full knowledge of the force on the tip during approach and retraction. During the approach, the AFM tip moves slowly toward the sample surface and the cantilever is bent toward the sample surface when the tip-sample distance arrives at a certain force-distance, as it starts to feel long-range attractive forces like van der Waals forces (Figures 1(a), (1)–(2), and 1(b), A–B). With further movement, the cantilever starts to feel repulsive forces as well; it eventually recovers equilibrium. Further approach to the sample increases the repulsive force that will bend the cantilever away from the sample, and the tip finally stops at the predefined force value (Figure 1(a), (4)–(5)). The compressive stiffness or elasticity modulus of the molecule can be deduced from the force-distance curve between C and D from this approaching process. During retraction the probe slowly moves away from the substrate and fingerprint information representing the molecular mechanical properties is captured during the stretch-relaxation process. In the retraction force curve (Figure 1(c)), point E represents an adhesion force caused by nonspecific interaction between the AFM tip and substrate. Point F indicates the start of the phase when

the molecule is pulled away from the substrate. The force increases until point G when the molecule ruptures from the AFM tip or substrate, and cantilever returns to the equilibrium position (point H). The nanomechanics such as the stretching or unzipping response of the molecule can be obtained from this pulling process.

The mechanical responses observed in SMFS can be divided into three categories: single nonlinear elastic curve, saw-tooth curve, and irregular mechanical event [64, 82]. The long single nonlinear elastic curve is characterized by a large peak which indicates the detachment of the sample from the tip. Some groups reported that peaks in the force plateau [82] were caused by simultaneous unzipping of the molecular strand. The saw-tooth force curve is composed of several peaks starting with irregular peaks and ending with a rupture force. Each peak represents an unfolding or sudden detachment event. The plateau force curve has a long uniform plateau and an abrupt force drop belongs to the manipulating response of β -sheet [64]. An irregular mechanical event generally refers to complex multimolecular interactions [83] in which interconnected fibrils are stretched sequentially leading to the extension and breaking of loops or bonds in one pulling cycle. Among the mechanical responses, single nonlinear and orderly force patterns are useful in exploring mechanical properties. At the same time two prominent theoretical models, the Freely-Jointed Chain (FJC) model [84] and the Worm-Like Chain (WLC) model [85], have been developed to analyze these SMFS data.

3. Intermolecular Interaction

The assembly of amyloid peptides is a dynamic process. The pathway from soluble molecules to insoluble fibrils is driven by intermolecular interactions which usually result in the formation of heterogeneous shaped structures. Amyloid fibrils interact with each other and aggregate into larger fibrils and eventually transform into texture structures. According to previous reports, the textured structures are constituted by different mature fibrils generated through multiple pathways. Therefore, obtaining the morphologies of various structures at different stages is essential to comprehend their assembly process.

3.1. Self-Assembled Structures. Plenty of shapes of amyloid structures were reported in many previous studies, including globular, β -hairpin, β -sheet, disk-like, worm-like, rod-like, honeycomb, parallel, and braided structures [1]. The variety of these assembled structures is attributed to the intermolecular interactions including hydrogen bonds, electrostatic interaction, and hydrophobic interactions [32, 38, 86–89]. The globular structures formed at the beginning of the incubation process are easily observed in AFM (Figure 2(a)). They consist of many monomers as well as disk-like structures [16, 39, 44, 58]. Branch-like [14] and parallel structures [38] (Figures 2(b) and 2(c)) are the intermediate products [90] composed of several oligomers. A mature fibrillar structure (Figure 2(d)) is a large fibril composed of two or more fibrils. Table 1 shows the dimensions of fibrillar structures obtained at different

incubation stages, and the stages are represented by their typical structures.

McAllister et al. [87] found that the increase of protein-protein interaction usually resulted in morphological transformations, for example, β -sheet conformation with an elevated content. Gerber et al. [91] have reported disk-like structures that form stacks through interoligomer interactions. Sandal et al. [64] have studied β -like formation of α -Syn and found the relative abundance of the β -like structures significantly increased in different conditions promoting the aggregation of α -Syn, such as pathogenic A30P mutation and high ionic strength buffer. Sibley et al. [86] found that the interaction between insulin and porphyrin gave rise to circular, ring-like structures as well as fibrils. The possible reason to form various morphologies is related to the interactions between specific residues. Jansen et al. [38] found that the compact character or mature fibrillar structures might originate from the effort to minimize the exposure of hydrophobic residues. In order to explore the effects of specific residues, some functional residues were substituted during AFM-based measurements. Various mutations showed distinctive functions: some were prone to form amyloid fibrils while others formed spherical aggregates; some functioned as a β -sheet breaker while others were promoting overall-length aggregation [32, 92–94]. For example, $A\beta_{40}$ and $A\beta_{25-35}$ were found to form small oligomers and thin fibrils, respectively [94]. However, A53T and A30P mutants of α -Syn were found to form spherical or annular protofibrillar structures [34]. Common morphologies were observed for some residues, for example, twisted fibrils derived from the Q24K mutant, and spherical aggregates and short fibrils derive from other mutants. E46K mutant displays a very distinctive smaller periodicity [36] compared with other mutants. We summarize the different shapes of amyloid with different dimensions in Table 1.

3.2. Assembly Processes. Time-lapse monitoring of the amyloid aggregation process is crucial to deepen the understanding of the amyloid aggregation mechanisms. The assembly of various amyloid fibrils can be followed by *in situ* time-lapse AFM images. Amyloid aggregation is commonly divided into two stages: nucleation stage and fibril growth stage [47].

In the nucleation stage, often called lag-phase, it is critical to understand the behavior of “seed-like” structures and intermediate prefibrillar structures, as these are the starting point of the overall self-assembly process [95, 96]. Fukuma revealed that the lag-phase was related to the increase of the mass concentration of elongated fibrils, and long incubating time was not an important factor during the nucleation stage [38, 97]. When studying on the process of $A\beta$ aggregation, Harper et al. [98] found that the rate of oligomers was slower than that of fibrils and that fibrils rapidly aggregated once sufficient nucleated oligomers formed. Their results indicated that the elongation rate of individual amylin protofibrils was 1.1 ± 0.5 nm/min. In line with the aggregation pathway, the stability of monomer and oligomer state was significantly lower than that of the following stages. It is reported that the inhibition of fibril formation could be realized by reducing the stability of protofibrils, by blocking protofibril-Protofibril

TABLE I: Dimension of different shapes for various amyloid fibrils based on molecular interaction.

Catalog	Sample	Shape	Height	Width	Length	Diameter	Periodicity	Reference
PrP	rPrP	Mature fibrils	108 ± 30 nm	N/A	1.0 ± 0.6 μ m	N/A	N/A	[30]
	PrP ₈₂₋₁₄₆	Globular	1.5–10 nm	N/A	N/A	31 ± 11 nm	N/A	[16]
		Disc-like	1–10 nm	N/A	N/A	20–60 nm	N/A	
		Fibrillar	N/A	2–3 nm	5 to 10 nm	N/A	N/A	
		Mature fibrils	N/A	N/A	3–10 nm	5–8 nm	30–130 nm	
Human PrP	Disk-like	1.8 nm	N/A	N/A	15 ± 3 nm	N/A	[31]	
IAPP	IAPP ₁₋₁₉	Mature fibrils	5–15 nm	N/A	1–2 μ m	5–15 nm	N/A	[32]
	IAPP ₁₋₁₉	Protofibrils	N/A	N/A	1–2 μ m	0.5–1.5 nm	N/A	
	IAPP ₁₋₂₉	Fibrillar	N/A	N/A	0.2–2 μ m	5–15 nm	N/A	
	hIAPP	Mature fibrils	N/A	N/A	100 nm-several μ m	5–7 nm	N/A	
	IAPP	Mature fibrils	0.1–0.8 nm	N/A	0.1–1 μ m	7–13 nm	4–40 nm	
α -Synuclein	α -Synuclein	Protofibrils	2.5–4.2 nm	N/A	N/A	32–180 nm	N/A	[34]
	α -Synuclein	Oligomers	1.4–7.5 nm	N/A	N/A	N/A	N/A	[35]
		Fibrils	4.5–6.0 nm	N/A	N/A	N/A	N/A	
	α -Synuclein	Protofibrils	~ 1.2 nm	~ 8 nm	N/A	3–4 nm	N/A	[36]
	α -Synuclein WT	Mature fibrils	7.5 ± 0.9 nm	N/A	N/A	141 ± 82 nm	N/A	
	α -Synuclein A30P	Mature fibrils	8.7 ± 1.4 nm	N/A	N/A	139 ± 46 nm	N/A	
	α -Synuclein E46K	Mature fibrils	9.8 ± 1.2 nm	N/A	N/A	59 ± 28 nm	N/A	
α -Synuclein A53T	Mature fibrils	10.4 ± 1.3 nm	N/A	N/A	151 ± 41 nm	N/A		
Insulin	Insulin	Mature fibrils	N/A	N/A	30–140 nm	4–6 nm	N/A	[37]
		Particles	1.1 ± 0.2 nm	N/A	N/A	N/A	N/A	
	Insulin	Oligomers	N/A	N/A	N/A	3.2–3.9 nm	N/A	[38]
		Protofibrils	$\sim 2.0 \pm 0.5$ nm	N/A	N/A	N/A	N/A	
	Human insulin	Mature fibrils	N/A	N/A	several microns	10–20 nm	N/A	[39]
TTR	TTR ₁₀₅₋₁₁₅	Rod-like	N/A	N/A	~ 1 μ m	7–12 nm	N/A	[40]
	TTR ₁₀₅₋₁₁₅	Rod-like	9 ± 3 nm	N/A	1 μ m	a few nm	N/A	[41]
$A\beta$	$A\beta_{26-35}$	Filaments	1.0 ± 0.2 nm	N/A	N/A	N/A	N/A	[42]
	$A\beta_{1-40}$	Oligomers	4–5 nm	N/A	N/A	N/A	N/A	[43]
	$A\beta_{1-40}$	Globular	N/A	N/A	N/A	~ 2 nm	N/A	[44]
		Low MW oligomers	1–3 nm	N/A	N/A	5–10 nm	N/A	
	$A\beta_{42}$	Low MW protofibrils	~ 2 nm	~ 7 –8 nm	40 nm	N/A	N/A	[45]
		High MW oligomers	3–6 nm	N/A	N/A	15–25 nm	N/A	
		High MW protofibrils	~ 1.8 nm	N/A	N/A	N/A	N/A	
	$A\beta_{42}$	Rod-like	N/A	5–11 nm	N/A	N/A	93.5 ± 21.0 nm	[46]
		Protofibril	~ 1.5 nm	~ 5.5 nm	~ 100 nm	1.1 nm	N/A	
		Protofibrils	N/A	N/A	N/A	~ 4 nm	92.5 ± 20.3	
		Fibrils	N/A	11.4 ± 0.8 nm	N/A	N/A	107.3 ± 29.0 nm	
		Globular	~ 5 nm	N/A	N/A	4.4 ± 0.4 nm	N/A	
	$A\beta_{42}$	Beaded chains	N/A	N/A	18–21 nm	N/A	18–21 nm	[47]
Mature fibrils		4–6 nm	25–35 nm	30–145 nm	N/A	N/A		
Mature fibrils		N/A	8–14 nm	>1 μ m	N/A	N/A		
Sheet-structure		0.8–1 nm	12–14 nm	N/A	N/A	N/A		
Fibrils		N/A	N/A	N/A	N/A	12–18 nm		
Fibrils		0.7–1.6 nm	4.8–9 nm	15–55 nm	4–8 nm	N/A		
$A\beta_{42}$	Protofibrils	N/A	8–10 nm	12–18 nm	N/A	N/A	[48]	
	Mature fibrils	3–7 nm	25–40 nm	>1 μ m	N/A	N/A		

TABLE I: Continued.

Catalog	Sample	Shape	Height	Width	Length	Diameter	Periodicity	Reference	
β -lactoglobulin	β -lactoglobulin	Worm-like	2.7 ± 0.5 nm	~ 7 nm	100–500 nm	N/A	N/A	[49]	
		Protofibrils	1.2 ± 0.4 nm	~ 7 nm	$>1 \mu\text{m}$	8 ± 2 nm	53 ± 8 nm		
		particles	3.8 ± 0.6 nm	N/A	~ 200 nm	8 ± 2 nm	N/A		
		Oligomers	2–8 nm	N/A	N/A	35–70 nm	N/A		
	β -lactoglobulin	β -lactoglobulin	Mature fibrils	N/A	15–20 nm	N/A	N/A	60–100 nm	[50]
			Mature fibrils	2–3 nm	N/A	$>10 \mu\text{m}$	N/A	30–40 nm	
	β -lactoglobulin	β -lactoglobulin	Mature fibrils	N/A	8.5 ± 1.4 nm	$0.1\text{--}2 \mu\text{m}$	N/A	34.3 ± 7.4 nm	[51]
			Worm-like	1.1 ± 0.3 nm	7.1 ± 1.6 nm	150–500 nm	N/A	N/A	
			Protofibrils	0.9 ± 0.2 nm	2.5–4 nm	N/A	N/A	N/A	
			Oligomers	1.8 ± 0.4 nm	N/A	N/A	~ 3.6 nm	N/A	
β 2-microglobulin	β 2-microglobulin	Protofibril	1.4 ± 0.3 nm	~ 5 nm	N/A	8 nm	N/A	[52]	
		Worm-like	~ 3.5 nm	N/A	$\sim 150\text{--}160$ nm	N/A	N/A		
		Rod-like	~ 3.5 nm	N/A	$\sim 20\text{--}150$ nm	N/A	N/A		
		Protofibril	4–5 nm	N/A	>1000 nm	N/A	N/A		
	β 2-microglobulin	β 2-microglobulin	Mature fibrils	5–8 nm	N/A	N/A	N/A	30–100 nm	[53]
			Mature fibrils	4–9 nm	100–500 nm	N/A	N/A	N/A	
	β 2-microglobulin	β 2-microglobulin	Protofibril	4 ± 1 nm	17 ± 3 nm	N/A	N/A	25–60 nm	[53]
			Protofibrils	2.2 ± 0.5 nm	18 ± 1 nm	N/A	N/A	20–30 nm	
Oligomers			N/A	N/A	N/A	10–12 nm	N/A		
EAK	EAK16	EAK16-IV globular	2–3.2 nm	N/A	N/A	34 nm	N/A	[54]	
		EAK16-IV fibrillar	0.4–3.7 nm	28.69 ± 2.27 nm	N/A	60 nm	N/A		
		EAK16-II fibrillar	0.3–2.2 nm	12–40 nm	N/A	N/A	N/A		
		EAK16-II globular	N/A	N/A	N/A	48 nm	N/A		
Ceratoptanin	Ceratoptanin	Protruding	50–60 nm	N/A	N/A	N/A	N/A	[17]	
		Rod-like	6–8 nm	N/A	N/A	N/A	N/A		
SSP	SSP1	Mature fibrils	6.0 nm	6.4 ± 0.2 nm	N/A	6.4 nm	N/A	[55]	
	SSP2	Mature fibrils	2.5 nm	6.2 ± 0.3 nm	N/A	6.2 nm	N/A		
Glucagon	Glucagon	Mature fibrils	$0.1\text{--}1 \mu\text{m}$	N/A	$15 \mu\text{m}$	52–55 nm	N/A	[56]	
		Disc-like	1.5 ± 0.5 nm	20.8 ± 5.2 nm	N/A	N/A	N/A		
		Protofibrils	6.05 nm	32.9 nm	N/A	N/A	N/A		

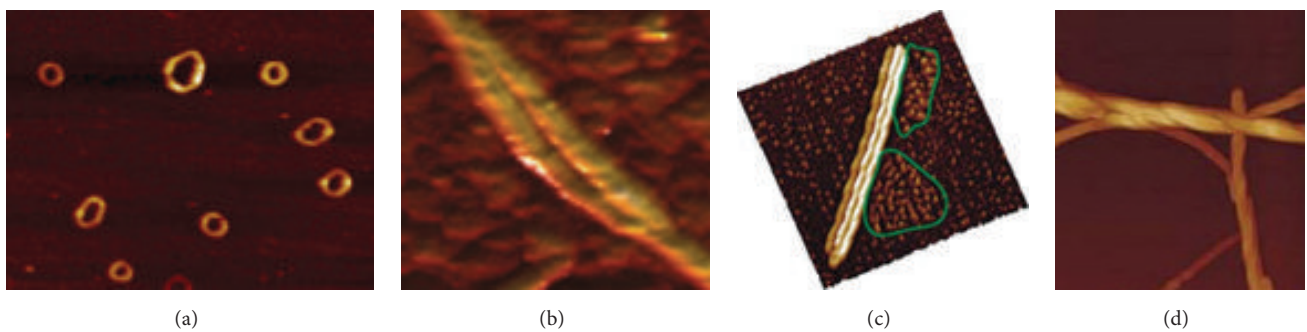


FIGURE 2: Distinctive shapes of various amyloid fibrils. (a) globular and disk-like structures [14], (b) branch-like structures [14], (c) parallel tubular fibers of insulin [38], and (d) mature insulin fibrils [38]. (Figures 2(a), 2(b), 2(c), and 2(d) are parts of figures from reference.)

interaction or by shifting the protofibril-monomer equilibrium. Oligomers contain nonfibrillar β -structures, and their total amount remains almost constant from the second half of the nucleation phase to the end of the aggregation process [44].

In the fibril growth stage, growth rate and aggregation propensity of amyloid assembly are influenced by different sequences or specific residues of the peptide. The corresponding amyloid assembly has been investigated by substitution of residues. Various amyloid peptides and their mutants were

studied, such as $A\beta$ with mutant $A\beta E22G$, $A\beta_{25-35_{N27}}$, or $A\beta_{40ARC}$ [59, 99, 100], α -synuclein with disease-related A30P, E46K, and A53T variants [34, 36, 93, 101, 102], mutant huntingtin (Htt) [103, 104], PAPBN1 N-WT with N-(+7)Ala mutant [105], and $\beta 2$ -microglobulin with its deamidated variant N17D [106]. Another example, rat amylin, although 84% residues are the same as in human amylin, cannot form amyloid fibrils [107]. The possible reason is that those residues, which differ from human amylin, influence the peptide assembly [59, 94]. In $A\beta$ mutation ($A\beta E22G$), fibrillization process will be accelerated, while the abundance of nonfibrillar assemblies will be decreased. Conway et al. [101] reported that the fibrillation rate of specific mutant peptides or mutant mixtures was faster than that of WT peptide. Seed-induced fibrillation of N-WT of PAPBN1 was slower than that of N-(+7)Ala. Monitoring the solubilization kinetics, they found that the stability of N-WT and N-(+7)Ala fibrils was different. In another case [98], $A\beta_{1-40}$ and $A\beta_{1-42}$ formed two discrete morphologies, and $A\beta_{1-42}$ aggregates grew faster than $A\beta_{1-40}$ ones. However, the rate of $A\beta$ amyloid aggregation *in vitro* was limited by the amount of available $A\beta$ nuclei. Moreover, the amounts of aggregated $A\beta_{1-40}$ and $A\beta_{1-42}$ protofibrils obviously differed from each other. Marek et al. [92] suggested that the difference between the amount of aggregated $A\beta_{1-40}$ and $A\beta_{1-42}$ protofibrils was caused by different residues affecting the aggregating rate of fibrillogenesis. In their study, the kinetics of amyloid assembly and the resulting morphology were influenced by the aromatic residues, which were important during the lag-phase in AFM measurements. Table 2 shows the assembly parameters of various amyloids under distinctive incubating environments. This overview suggests that experimental factors, such as buffer, pH, temperature, and concentration, are critical to the result of the fibrillation process.

3.3. Assembly Pathways. The aggregation process was reported to be associated with the pathology of the corresponding amyloid protofibrils. Numerous studies have been carried out to explore the aggregation pathway [13, 108]. For the mechanism of amyloid fibrillogenesis, several explanations have been established. It is suggested that the common noncovalent structure of proteins such as backbone hydrogen bonding and hydrophobic interaction [17] were the main forces driving the amyloid fibrils' aggregation. In early studies, a mechanism of nucleated conformational conversion, so-called on-pathway, was applied to explain the amyloid aggregation. However, exceptions have been found. Therefore, an alternative off-pathway mechanism was proposed to explain fibrillogenesis [57, 63]. While more and more studies explore the mechanism of amyloid aggregation, models for various kinds of amyloid fibrils have been designed to explain the amyloidogenesis formation. Here, we propose a model (Figure 3) based on various previous studies [15–17, 34, 38, 46, 53, 56, 62, 63, 109–113] to elucidate the mechanism of multipathway aggregation and describe it in detail in the following parts.

3.3.1. Nucleation and Elongation. AFM measurements revealed that the most favorable nucleation pathway contains

a two-stage sequential conversion (Figure 3, steps 1 and 2), in which soluble monomers are aggregated into small annular and spheroidal mature oligomers [14, 114] and then these seeds grow by further addition of more mature monomers. Mature oligomers have accumulated more monomers but still show globular morphology. Oligomers still have spherical superstructure but already show characteristic amyloid folding [93]. $A\beta_{1-42}$ [45, 47, 48, 115, 116], glucagon [56, 117], amylin [24, 107], and β -lactoglobulin [49, 50] have been observed to aggregate through the nucleation pathway. Fibril elongation (Figure 3, steps 4, 5, and 6) becomes the main process once a critical amount of oligomeric seeds has formed. In the elongation process, the addition of more monomers leads to a structural change into elongated prefibrillar intermediates, eventually resulting in the formation of protofibrils [45, 105]. Different assembly processes of amyloid were indicated in different color of lines in Figure 3.

3.3.2. Hierarchical Pathway. Hierarchical aggregation, which happens after nucleation and elongation, is characterized by two or more protofibrils intertwining through interoligomer or interfibril interactions. They form higher ordered fibrils and eventually helical structures. Many species, CP [17, 118], human prion protein (PrPSc) PrP₈₂₋₁₄₆ [16], PrP₁₀₆₋₁₂₆ [119], Ig light-chain [62], transthyretin peptide (TTR₁₀₅₋₁₁₅) [120], and β -lactoglobulin [51], were found to aggregate adopting a hierarchical pathway. Small or large oligomers undergo elongation and form heterogeneous structures, such as branch-like structures, annular-shaped oligomers, braided structures, and hairpin-like structures [17, 45, 46, 55]. Sbrana et al. [17] reported that branched structures were the disordered assembly of protruding segments. They also found that early annular-shaped oligomers seem to function as fundamental bricks in the hierarchical aggregation process [17]. The braided structure [62] consisting of winding protofibrils is usually observed in amyloid fibrillogenesis as well. In the self-assembly experiment of $A\beta_{42}$ peptides [48], intermediate-like protofibrils were found to join the helical structure formation. Generally speaking, these heterogeneous morphologies and twisting periodicity indicated a complex hierarchical amyloid assembly process.

3.3.3. Lateral Aggregation. Increasing evidence suggests the existence of alternative pathways [38] in amyloid fibrillogenesis. One prominent example is lateral aggregation; it usually follows the elongation phase. Ceratoplatenin (CP) [17], PrP [109], glucagon [56, 95], insulin [38, 57], $A\beta_{1-42}$ [46, 47], and $\beta 2$ -microglobulin [53, 121] were found to aggregate laterally. In this pathway several protofibrils associate parallelly to form a ribbon that wraps around into a fibril (Figure 3, steps 10 and 12, type 3 structure). It was reported that fibrillar bundles formed loose tangles eventually leading to the formation of mature fibrils [57]. Fibrils containing laterally associated filaments were found to show a right-handed twist at one point [47]. A similar aggregation pathway was also found in the strand-swapping peptide 1 (SSP1). Nagarkar et al. [55] reported the lateral self-assembly of SSP1 dimers via H-bond interaction along the fibril's long axis. Kad et al. [106] reported that four protofibrils associated laterally wound into

TABLE 2: Assembly parameters of various amyloid fibrils in different experimental conditions.

Disease	Species	Oligomer	Protofibril	Fibrils	Temperature	Ph	Substrates	Concentration	Buffer	Reference
Dialysis related amyloidosis	β 2M	26 min	89 min	164 min	37°C	3.6	Mica	1 mg/mL	0.4 M NaCl	[55]
Diabetes (type 1 or type 2)	Insulin	N/A	N/A	250~280 min	60°C	1.6	Mica	200 μ M	50 mM KCl/HCl in Millipore Super-Q water	[57]
	Insulin	30 s	5 min	10 min	60°C	1.6	Mica	170 μ M	Ultrapure water	[38]
	IAPP	180 min	13.5 h	N/A	23°C	7.0	DOPC/DOPG	1 μ M	Phosphate buffer solution	[58]
	β -Lactoglobulin	10 min	120 min	24 h	80°C	2.0	Mica	4% w/w	Deionized water	[49]
	β -Lactoglobulin	45 min	85 min	100 min	80°C	2.6	Mica	20 g/L	Milli-Q water	[50]
Parkinson	A β 26-35	N/A	84 min	120 min	23°C	7.4	POPC SLB	50 μ M	Water	[42]
	A β 1-42	10 min	N/A	72 h	37°C	N/A	Mica	62.5 μ M	Phosphate-buffered saline	[59]
	α -Synuclein	21 days	32 days	42 days	23°C	7.5	Mica	300 μ M	20 mM sodium phosphate buffer	[35]
N/A	Glucagon	90 min	420 min	20 h	23°C	2.0	Mica	2.5 mg/mL	10 mM HCl and 1 mM Na ₂ SO ₄	[56]
Transmissible spongiform encephalopathy	Yeast Prion Sup35	15 min	25 min	240 min	25°C	5.0	Mica	5 μ M	Phosphate buffer	[60]
Familial amyloidotic polyneuropathy	TTR105-115	N/A	24 h	60 h	25°C	1.9	Mica	1 μ M	HPLC grade water	[61]
Systemic AL amyloidosis	Ig light-chain	N/A	N/A	10 h	37°C	2.0	Mica	N/A	50 mM sodium acetate buffer	[62]

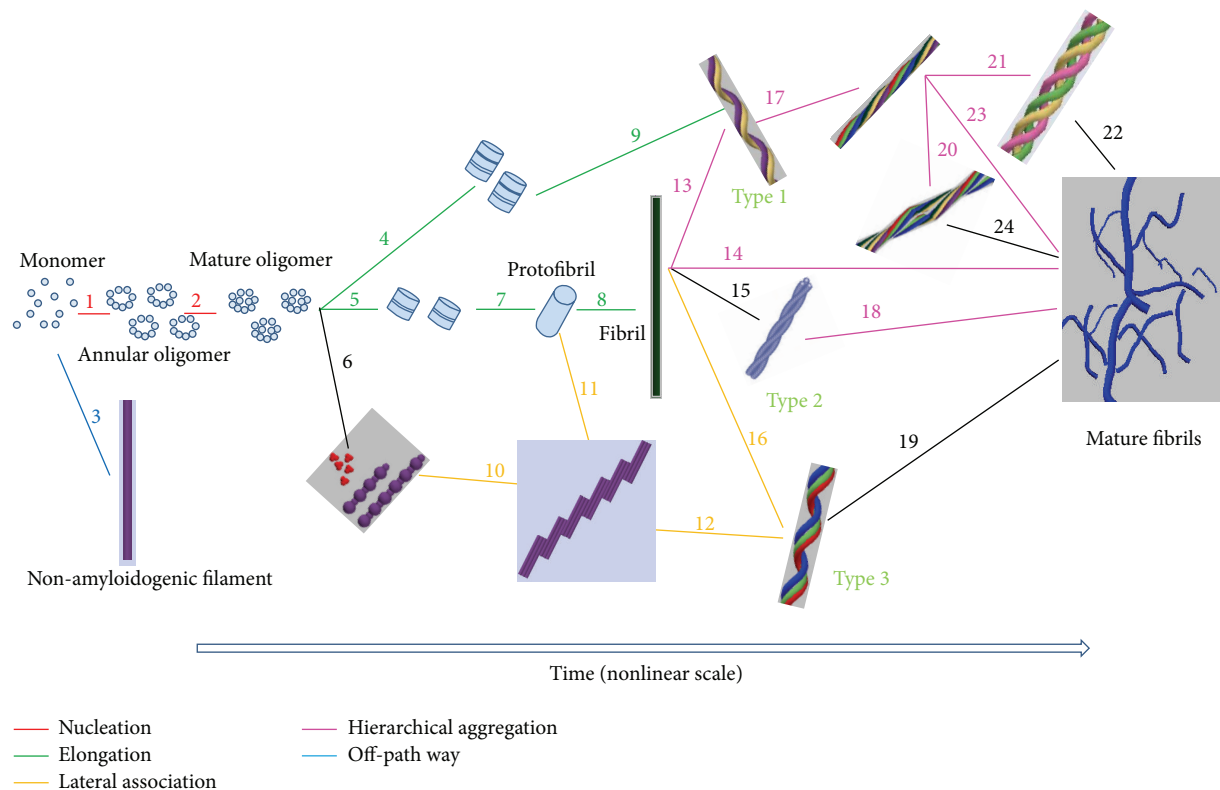


FIGURE 3: Model proposed based on various models in the investigation of numerous amyloid aggregations. There are five processes before the formation of mature fibrils: nucleation [56] (steps 1 and 2 in red lines), elongation [17] (steps 4, 5, 7, 8, and 9 in green lines), lateral association (steps 10, 11, 12, and 16 in yellow lines), hierarchical aggregation [15, 38, 53] (steps 13, 14, 17, 18, 20, 21, and 23 in purple lines), and off-pathway [63] (step 3 in blue line).

a twisted-ribbon shape with a clear periodicity, but there was no suggestion that lateral aggregation of smaller species was detected [49].

3.3.4. Multipathway. Multipathway is the combination of all pathways mentioned above: monomers conformationally change and merge into oligomers (Figure 3, steps 1 and 2); then oligomers longitudinally aggregate leading to protofibrils (Figure 3, steps 4, 5, and 7). Finally protofibrils laterally aggregate into protofibrils (Figure 3, steps 6, 10, and 11) [122]. Homogeneous protofibrils undergo elongation to form higher ordered mature fibrils (Figure 3, steps 13, 15, and 16) and finally lead to complex blocks. Hierarchical and lateral-aggregating structures were frequently observed in various kinds of amyloid fibrils [15–17, 36, 38, 45, 48, 53, 56, 57, 62, 95, 109, 111–113, 123].

In the off-pathway assembly, soluble monomers or oligomers directly construct fibrils [63] without the “seed-like” aggregation (Figure 3, step 3). Natalello et al. [16] reported that the linear PrP_{82–146} aggregates formed by oligomers aligning which suggested an off-pathway assembly. The main differences between on- and off-pathway oligomers are mainly their sizes and shapes. So, it is critical to clarify whether the aggregation is based on a nucleation phase and seeds or the formation of an active small oligomer.

On-pathway aggregation is characterized by the appearance of homogeneous nuclei, followed by elongation. At the same time, three types of fibrils (Figure 3) were found during the later stage of the aggregation process. These different types represent distinctive structures: type 1 is formed by two twined protofibrils; type 2 is formed by three twined protofibrils; and type 3 is formed by several parallel protofibrils laterally associated together. Several type 1 fibrils rearrange into intertwined style fibrils occasionally. Based on associated segments forming larger structures, Segers-Nolten et al. [36] proposed a segment pathway, indicating a multipathway assembly for α -synuclein. Jansen et al. [38] revealed that insulin amyloidogenesis *in vitro* involved a multipathway assembling scheme, in which native dimers were formed by either hierarchical intertwining or lateral interaction. A similar observation was made by Mauro et al. [57]. The size and shape of oligomers were measured to identify different distinctive pathways. However, it could not be distinguished [55] whether the hierarchical or parallel fibrils were lacking structurally different nucleating centers. Although various models have been proposed, the detailed mechanism needs further exploration such as amyloids’ aggregation and inter- or intramolecule interactions affected by constituent peptides or chemical chaperones.

3.4. Influencing Factors of Assembly. High-resolution AFM has been used in many characterization studies, aimed at the morphology and assembly pathway of amyloid fibrils and the effects of chemicals and chaperones [14, 25, 73, 124–126]. Concentration [36, 51, 96, 127–129], substrate [130], temperature [38, 49, 50, 57, 131], pH value [54, 106, 121, 132, 133], ionic strength [96, 99, 129, 134, 135], and stirring time and addition of denaturing agents [24, 50, 82, 115, 119, 128, 136] are important factors affecting the formation of various aggregates. For example, different substrates can affect the orientation of amyloid fibrillogenesis [4]; solvent conditions play critical roles in amyloid aggregating propensity, rate, and structural formation. In order to decipher the molecular mechanisms and develop better strategies to modulate aggregation, it is imperative to learn the effects of environmental conditions on structure, molecular assembly process, activities, and growth kinetics. In this section, we will have a closer look on these experimental factors.

3.4.1. Concentration Effect. Many trials indicated that the concentration of amyloid peptides played a prominent role in amyloid aggregation. Although differences in concentration are correlated to the corresponding disease *in vivo*, their precise relation is not well-known. Previous work showed that the self-assembling rate of amyloid increased with the increasing of its solution concentration [137]. Segers-Nolten et al. [36] found that α -synuclein shows relatively normal function at low concentrations, but it is apt to transform into a pathogenic species at high concentrations. There are a large number of experiments looking into surface density and concentration of the incubation solution [36, 51, 96, 127–129]. These experiments indicate that proteins form well-defined fibrils in low peptide concentrations with lower aggregation rates than that in a higher concentration. So, the amyloid fibril formation can be accelerated through increasing either surface density or the concentration in incubation solution [127]. In the same way, Pazzagli et al. [118] systemically studied the lag-phases in different concentrations and found that the transition time in higher concentration (1.3 Mm, lag-phase time being 6 hours) was sharply shortened comparing with that of the lower concentration (0.54 mM, lag-phase time being longer than ten days). The surface density of amyloid self-assembled fibrils can be adjusted by tuning the bulk concentration, and many groups showed that dense fiber-networks can be constructed starting with high peptide concentrations [96, 129]. However, insulin is an exception, as obvious structure change was observed for two enormously different concentrations [57].

3.4.2. Temperature Effect. Temperature, in general, can affect morphology, growth rate, stability, and activity of heterogeneous fibrils and eventually change the overall process of amyloid aggregation [38, 49, 50, 57, 131]. For example, various structures were observed upon increasing the temperature to 70°C, among them long straight rods, twisted-ribbon-like structures, rod bundles, and rope-like structures [38]. Increasing temperature can not only shorten the aggregation

lag-phase [118] but also affect the height of the assembled fibrils [138]. In contrast, nucleation was inhibited at low temperatures. Pazzagli et al. [118] investigated the ordered aggregates of ceratoplatinin and found that lag-time decreased from 30 to 10 days when incubation temperature was increased from 37°C to 50°C. Palhano et al. [60] employed 4°C and 25°C to investigate the effect of temperature on the process of amyloid aggregation. Their AFM results showed that the aggregations were higher at 4°C than at 25°C. At the same time they revealed that amyloid fibril were, on average, shorter at 4°C than at 25°C. The reason for this phenomenon is that the activity of amyloid can be influenced by temperature [131]. Native M β activity remained stable up to 70°C, but its activity abruptly decreased at a temperature ranging from 70°C to 80°C. Bellezza also found that the main activity of adsorbed M β decreased abruptly between 30°C and 60°C, while the activity reduced slightly below 30°C or higher than 60°C. Mauro et al. [57] studied the temperature impact on insulin and found the assembly adopting double quenching experiments. Their results indicated that the double quenching allowed the growth of a few long fibrils.

3.4.3. pH Effect. An acidic environment is beneficial for the amyloid formation [35, 87, 106, 128], and there are plenty of studies modulating amyloid aggregation through varying pH values [54, 106, 121, 132, 133]. In these studies, researchers found that amyloid fibrils were not stable in either acidic or alkaline solution environments, which easily led to the conformational changes. Many investigations suggested that the nanostructure of various amyloid assemblies could be modified through adjusting pH value. Bortolini et al. [133] built different nanostructures of peptide with three different kinds of residues by tuning the pH value of the solution [133]. McAllister et al. [87] reported that decreasing pH value resulted in the prominent increase of the interaction among protein molecules of A β (1–40) peptide, α -synuclein, and lysozyme. This leads to a dramatic increase in aggregation rate at the proper pH value. For most peptides there are large differences in reaction speed and product morphology between acidic and alkaline conditions. Short fibrils or small globular aggregates were found at pH 2.0, and fibrillar structures were found at pH 2.7, but there was no fibril or large aggregate observed at pH 3.7. Hong et al. [54] studied two kinds of amyloid aggregates at pH values varying from 4 to 11. Hong et al. found that KAK16-IV formed globular assemblies in neutral pH environments, which changed into fibrils under alkaline conditions. Another mutant, EAK16-II, did not exhibit any apparent changes. Jenko et al. [139] established that Stefin B started to form fibrils at pH 5, whereas Stefin A needed to be acidified to a pH value of less than 2.5. Most tests showed that acidic environments were conducive to fibrils formation, but the transformation of Stefin B from protofibrils into mature fibrils was inhibited at acidic solution [128].

3.4.4. Solvent Effect. AFM experiments suggest that the incubating medium plays an important role in the assembly process [47, 49–51, 97, 127, 140, 141]. Chaudhary et al. [97]

reported that AcPHF6 could be organized into fibrillar structures when the sample peptide was dissolved in MeOH, TFE, or HFIP. Gosal et al. [49] found that the aggregation rate of β -lactoglobulin was correlated with solvents used in experiments. There are more fibrillar structures presented in TFE-water mixed solvent in contrast to other alcohols. Gelling propensity was related to solvents: methanol > ethanol > propanol > TFE. At pH 7, the tendency of β -lactoglobulin to form a gel was higher in propanol than that in ethanol, methanol, or TFE. The fibrillar aggregates formed in TFE-water mixtures; imaged with negative-staining EM these TFE-induced fibrils showed worm-like and granular structures [49]. Nichols et al. [43] found rapid assembly of amyloid- β peptide at a liquid/liquid interface which induced unstable β -sheet fibers. The association rate of $A\beta_{1-40}$ in a two-phase system with chloroform was 1~2 orders of magnitude faster than that in the buffer alone. Daniela et al. [50] reported that β -lactoglobulin formed different amorphous aggregates in alcohols and TFE. The concentration of TFE also influenced the assembly process [128]. The aggregating rate of human Stefin B fibrils was accelerated in a solution containing alcohol, but, in contrast to other proteins, the lag-phase did not change TFE concentration.

3.4.5. Cations Effect. Metal ions such as Fe^{3+} , Cu^{2+} , K^+ , and Na^+ significantly affect the process of amyloid aggregation and morphology [96, 99, 129, 134, 135]. Ions function as an inhibitor or accelerator to various amyloid species, and fibril shapes may be influenced by varying the metal ions concentration. Precisely how the ions effect the aggregation is still controversial. Ryu et al. [96] reported that the initial rate of amyloid fibrillation was accelerated by 6 times in the presence of Fe^{3+} ions, but ions might act as an inhibitor under other conditions. For example, high ion concentration inhibited amyloid aggregation of rat amylin [107]. In addition, disrupted adhesive nanofiber structures can be repaired by solutions containing divalent cations [127].

Apart from the effects on amyloid aggregation speed, the morphology is also influenced by cations [134], as they interfere with peptide-peptide interaction. For example, fibrillar structures tend to form at low Cu^{2+} concentration, but the amount of granular, amorphous aggregation increased rapidly at higher concentrations of Cu^{2+} . Hong et al. [129] reported that the dimensions and surface tension of peptide nanostructures were influenced by the NaCl concentration in the solution. The orientation of amyloid aggregation on mica was affected by ions [99]; this was attributed to cooperative interaction of a positively charged $A\beta_{25-35}$ peptide moiety binding to the mica lattice. They pointed out that $A\beta_{25-35,N27C}$ binding to mica was sensitive to the presence of cations and suggested that the increase of NaCl or KCl concentration could reduce the binding strength between fibrils and mica surface. Further research indicated that fibrils binding to mica were more sensitive to K^+ compared to Na^+ ions.

3.4.6. Denaturing Additives Effect. Various additives are usually employed to modulate the behaviors of amyloid fibrils

through accelerating, inhibiting aggregation, or disassembling [24, 50, 82, 115, 119, 128, 136]. Some reversible changes can be accomplished [127, 142] by varying the concentration of additives. Different additives have been used to study their effects on various amyloids, such as the effect of Zn, sulfated glycopolymers, $C_{12}C_6C_{12}Br_2$ micelles, Trimethylamine N oxide, and glycerol on $A\beta$ peptide [82, 141–143], TFE on human stefin B [135], anionic lipid phosphatidylserine (PS) and cholesterol on amylin [24], antibody scFv on α -synuclein, insulin, and β -amyloid [136, 142], chitotriose and NAG on HEWL [132], DTT and SDS/CTAB on lysozyme [144], metalloporphyrins on insulin [86], SSMs-ectoine and mannosylglyceramide (MGA) on PrP₁₀₆₋₁₂₆ [119], and so forth. Though all additives affect the assembly process of amyloid, different additives act through different mechanisms on amyloids. Some additives affected the whole assembly process, whereas others acted at specific assembly stages.

Cho et al. [24] reported that the anionic lipid PS stimulated amyloid aggregation only at a certain stage. ScFv-6E enhanced the kinetic aggregation of httexl-51Q by binding and stabilizing the nascent fibrils which reduced the thermodynamic lag-time of fibrillogenesis [136]. Marcus et al. [145] suggested that the isolated scFv possibly targeted a shared fibrillar motif which might be the cross- β -sheet characteristic of amyloid fibrils. Further investigation suggested that those bonds appeared after lag-time stages. The random coil to β -sheet conformational transition of $A\beta$ was rapidly accelerated by Trimethylamine N oxide and glycerol [82], but the final stage of amyloid formation was dominated by osmolyte-facilitated changes in $A\beta$ hydration. Some additives function as inhibitors in amyloid aggregation. Cholesterol sequestered the amylin aggregation [24], metalloporphyrins inhibited insulin aggregation [86], and chelator of Zn induced a slow but nonfibrillar aggregation of globular $A\beta$ [142]. Kanapathipillai et al. [119] suggested a preferential exclusion mechanism of amyloid aggregation by adding denaturing agents. In their study, mixtures of ectoine and MGA, hydroxyectoine, and MG were employed to affect PrP₁₀₆₋₁₂₆ amyloid formation process. The results indicated that the former could inhibit PrP₁₀₆₋₁₂₆ amyloid formation whereas the latter could not. They found that hydroxyectoine and MG, respectively, possessed more hydrophilic features and negative charges because of their carboxyl group. In addition, PrP₁₀₆₋₁₂₆, consisting of N-terminal polar heads and long hydrophobic tails, seemed to only interact with its polar head in most hydrophilic solutes. It was found that $A\beta$ N-terminal hydrophilic domains could disassemble amyloid fibrils [116]. Similarly, mature $A\beta_{1-40}$ fibrils could be disassembled by a cationic gemini surfactant, $C_{12}C_6C_{12}Br_2$ micelles, *in vitro* [115]. Synergistic, hydrophobic, and electrostatic interactions are responsible for the disassembling of $A\beta_{1-40}$ fibrils. Tang et al. [146] reported the assembly-disassembly processes of α -synuclein (α -Syn) fibrils in different solutions and chaotropic agent guanidinium chloride rapidly breaking the long α -Syn fibrils into fragments.

3.4.7. Substrate Effect. AFM-based experiments indicated that identical species are apt to form different morphologies [52] at different rates [147] on distinctive substrates such as

mica, graphite, gold, glass, lipid membranes, and cell surfaces. Growth rate, orientation, and deformation of the aggregation were greatly influenced by the substrates used in the experiments. Some correlations exist between substrates and amyloid fibrils conformation [4, 11, 16, 29, 30, 42, 99, 107, 108, 135, 148, 149]. More and more results attributed this phenomenon to intermolecular interaction of static electronic interaction between amyloids and substrates [130, 135, 137, 150, 151]. Linear structures and uniform elongated sheets formed on mica and graphite substrates, respectively. At the same time, the orientation of assembled sheet structures can also be affected by substrates. The amount of fibrils, found in AFM images [148], suggested that the aggregation rate of protein covalently immobilized on a silicon surface was 4.6 times faster than that on a gold surface. Distinct hydrophilic and hydrophobic conformations formed on corresponding solid substrates. Right-handed helical orientation of beaded fibrils [47] formed on a hydrophobic interface, while left-handed helical orientation formed on a hydrophilic mica surface. However, A β 42 could not form fibrils on the surface of planar lipid. The reason might be that mica is crystalline and has negatively charged surfaces but the lipid membrane has a soft and fluid nature. Zhang et al. [42] reported that A β _{26–35}, respectively, formed large-scale, highly ordered, parallel-oriented surface patterns on different lipid membranes. Their observation implied that the properties of lipid membranes, such as the fluidity, were associated with the parallel-oriented fibrogenesis. Wegmann et al. [30] and Karsai et al. [99] also reported that heterogeneous shapes occurred on cell surfaces. Kiselev et al. [148] revealed the deformation of protein molecules immobilized on mica surfaces, and they reported that some species were preferentially adsorbed on specific substrate defects, such as edges of defects. Through myoglobin (Mb) adsorption on ZrO₂-P substrate, Bellezza et al. [131] found that ZrO₂-P nanoparticles affected the morphology and the interaction which resulted in prefibrillar-like aggregates. Furthermore, Liang et al. [61] found that different-staged A β had distinctive mechanisms of aggregation. At present, it is hypothesized that hydrophobicity is the main driving force of A β and liposome interaction.

3.4.8. Other Disturbances' Effect. Other factors, such as stirring, dehydration, and magnetic fields, were found to have effects on the amyloid aggregation as well. Stirring accelerated the formation of amyloid fibrils [147]. The internal structure of A β _{1–42} fibrils was changed by dehydration [152]. Hill [153] reported that aligned aromatic peptide tubes formed in strong magnetic fields, which benefited the fibril growth [139].

4. Intramolecular Interaction

Apart from the studies using AFM imaging to investigate intermolecular interactions, the intramolecular interactions were explored by AFM-based single-molecule force spectroscopy (SMFS). SMFS has been employed to probe the mechanical properties of various biological molecules, such as polysaccharides, DNA, and proteins. A unique mechanical response representing the fingerprint of the corresponding

molecule was discovered. For example, the length transitions in the mechanical fingerprint of polysaccharides were attributed to the shift of individual pyranose rings from chair to boat or inverted chair conformations [154, 155]. The extensive conformational change of a B-S transition was observed in stretching dsDNA. Moreover, direct measurement of intramolecular interactions, including donor-acceptor, ionic, conjugational, and hydrophobic interactions, has been performed. Recently, various amyloid fibrils were probed. The mechanical properties of β -sheets were gradually observed with SMFS.

4.1. Amyloid Fibrils' Unfolding. Force measurement of amyloids focused on the β -sheet structures existing in A β _{25–35} and A β _{1–40} peptides [29], α -synuclein [64], TTR_{105–115} [156], unicellular Subaerial Algae [122], terrestrial alga *Prasiola linearis* [83, 157], and glucagon [117]. Figure 4 illustrates the unfolding mechanical signatures of α -Syn (there are three tandem titin I27 domains on either side of the α -Syn sequence [64] in Figure 4(a)). The repetitive saw-tooth patterns during the stretch process represent the typical mechanical response of multidomain proteins of titin [158]. During the stretch process, the increasing and the abrupt force drop in each saw-tooth pattern reveal that one I27 domain was stretched and unzipped. So, the six peaks on left side with identical spacing and amplitude indicate the regular inner structure of β -sheet (Figure 4). The last peak in the saw-tooth pattern corresponds to the detachment activity between the molecule and the tip. The number of unzipping peaks agreed with that of the I27 domains composing the protein, and the indistinguishable peaks suggested a series of identical structures. The spacing gap between each saw-tooth pattern in figure is 28 nm for tandem titin I27 domains, and the approximate force value of the six unzipping peaks is 200 nN.

For other amyloid fibrils, the force patterns exhibit different spacing and rupture forces. The saw-tooth peaks were regularly spaced with a separation of approximately 36 nm for unicellular Subaerial Algae, 56 ± 9 nm for cement of the barnacle *Amphibalanus amphitrite* [159], 36.04 ± 6.5 nm for terrestrial alga *Prasiola linearis* [157], 34.9 ± 5.6 nm for *Prasiola linearis* [83], and 1600 ± 76 nm for glucagon [117]. The average magnitude of the force peaks of terrestrial alga *Prasiola linearis* was found to be 244 ± 36 pN at the stretching rate of 2.5 to 3.0 $\mu\text{m/s}$, 235 ± 12 pN for glucagon at the loading rate of 2 $\mu\text{m/s}$, 3.5 nN for stretching cement, and 20 pN for TTR fibrils at the loading rate of 30 nm/s. The magnitude of the force, at this extension rate, would be the characteristic of the previous systems containing hydrogen-bonded β -sheets. Each jump of the saw-tooth response was attributed to a “sacrificial bond” and “hidden length” [160]. The fingerprint of the force responses could be used to analyze the specific structure present in heterogeneous conformations [87]. In the study of stretching A β _{25–35} and A β _{1–40} peptides, staircase-like force patterns were obtained. Kellermayer et al. [29] found that the force curves for two kinds of amyloid fibril were qualitatively similar. Comparing the statics data of mechanical response, A β _{25–35} and A β _{1–40} exhibited the characteristics of the smallest plateau forces of 33 ± 7 pN and 41 ± 7 pN, respectively. They suggested that

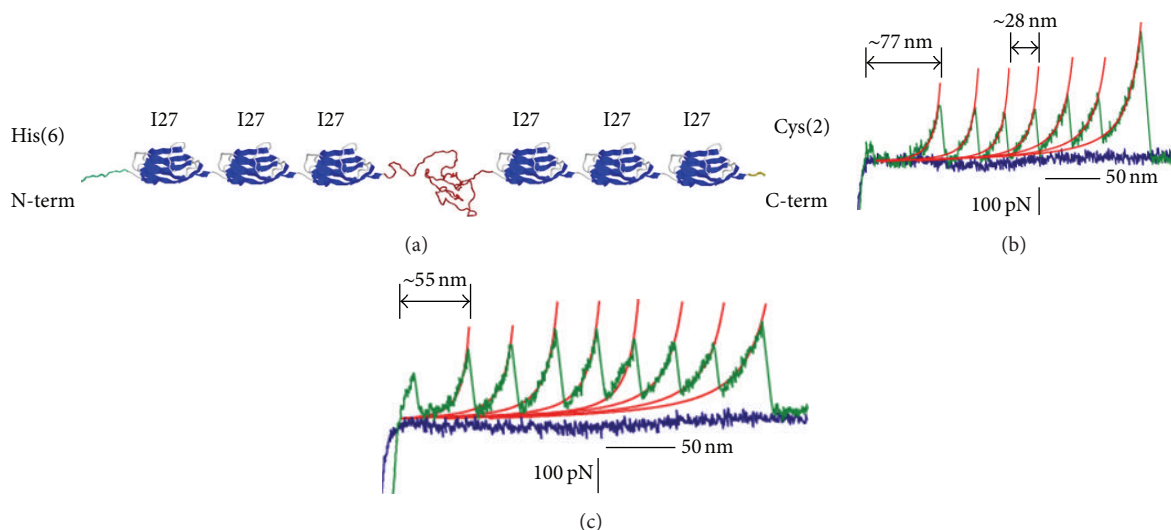


FIGURE 4: (Images of (a), (b), and (c) in Figure 4 are parts of figures from reference.) The mechanical signatures of α -Syn conformational classes recorded by SMFS [64]. (a) Schematic representation of the polyprotein constructs used in the work. (b) Example of curve characterized by a featureless region assigned to the stretching of α -Syn moiety having, in this case, the mechanical properties of a random coil. (c) Example of the curves featuring the β -like signature of α -Syn, showing seven practically indistinguishable unfolding events of similar magnitude and spacing.

the smallest force was the very unit for superimposing force pattern.

4.2. Mechanical Measurement. During the pulling process of SMFS, the mechanical response can be indirectly used to measure the semiflexible properties of molecules. Their quantification was performed by fitting a Worm-Like Chain (WLC) model for the semiflexible properties. The studies revealed the mean persistence length of 0.44 ± 0.08 nm for *Coccomyxa* sp., 0.38 ± 0.07 nm for *Glaphyrella trebouxiodes* [122], 0.35 ± 0.05 nm for barnacle cement [159], 0.38 ± 0.06 nm for $A\beta_{1-40}$ [29], 0.36 ± 0.05 nm for α -Syn [64], 0.57 for adhesive nanofibers [157], 0.34 ± 0.18 nm for EPS [83], and 0.70 ± 0.15 nm for glucagon [117]. Two kinds of Subaerial Algae with strong attachment to anthropogenic surfaces were selected to investigate the nanoscale adhesive properties by SMFS [157] technology. The mechanical data shows how amyloid provides cohesive strength to the adhesives, and this intrinsic mechanical property can be used to explain the attachment of these subaerial microalgae onto various surfaces in urban environments.

The stiffness of nanoscale structures was quantified using force indentation curves [86, 159, 161, 162]. By fitting indentation data, typically the mechanical Hertz model [74], Young's modulus of the material could be obtained.

Beside the useful modulus property of amyloid, the basic force-distance curve can also provide rich information of samples. The reproducibility of the saw-tooth pattern when successive curves are taken at the same locations [64, 83, 122, 157] is strong point of view to prove that amyloid fibers are able to reassemble after being stretched. Dong et al. [117] suggested that the observed elasticity was due to a force-induced conformational transition and the reversibility was

attributed to the β -helical conformation of protofibrils which allows a high degree of extension.

Insulin fibrils exhibited a nearly elastic response to the compressive load which suggested lower packing density in amyloid fibrils [161] than that in protein crystals. The measured lower Young modulus indicated that insulin fibrils possess a looser internal packing compared to globular protein crystals and agree with the loose structure of β 2-microglobulin amyloid [163].

4.3. Effects of Experimental Conditions. Force responses are, in a similar fashion as the morphology, heavily influenced by experimental parameters such as loading rate, ionic concentration, pH value, and incubating time. Time-lapse AFM imaging and force spectroscopy have been performed to study the assembly process of $A\beta_{1-40}$ fibrils under different experimental conditions *in situ*. α -Synuclein, amyloid β -peptide ($A\beta$), and lysozyme were used to explore the pH value influence on interprotein interaction of amyloid aggregation [87]. It has been confirmed that the pH value for these conformational transitions coincided with pH values that led to changes in the pulling forces. The SMFS data showed that the attractive force between homologous protein molecules was minimal at a physiological pH value and increased dramatically at an acidic pH value. However, it has not been directly proven that the dramatic increase in interprotein interaction under acidic conditions was responsible for fibrillation.

5. Summary and Outlook

We reviewed the latest observations of inter- or intramolecular interactions of amyloid fibrils using AFM and AFM-based

SMFS techniques. Various morphologies of amyloid fibrils, the assembly process, and the aggregating pathways were summarized in order to analyze their influence on amyloid fibrillogenesis. In addition, the fingerprint of mechanical response through AFM-based SMFS complements the information gained by topological AFM imaging. There is no doubt that SMFS combined with AFM provides a useful application in detecting inter- or intramolecular interactions. They opened a new path to explore fibrillogenesis, provide information of amyloid fibrils, and finally initiate a solution to curing neurological disordered diseases.

Competing Interests

The authors declare that they have no competing interests.

Acknowledgments

The authors acknowledge financial support from the National Natural Science Foundation of China (nos. U1304310 and 21373077), and Henan Natural Science Research Office of Education project (no. 12A180005 and no. 2010A140001).

References

- [1] C. Bortolini and M. Dong, "Cystine oligomers successfully attached to peptide cysteine-rich fibrils," *Frontiers of Chemical Science and Engineering*, vol. 10, no. 1, pp. 99–102, 2016.
- [2] J. Hardy and D. J. Selkoe, "The amyloid hypothesis of Alzheimer's disease: progress and problems on the road to therapeutics," *Science*, vol. 297, no. 5580, pp. 353–356, 2002.
- [3] D. J. Selkoe, "Alzheimer's disease: genes, proteins, and therapy," *Physiological Reviews*, vol. 81, no. 2, pp. 741–766, 2001.
- [4] J. Wang, Y. Cao, Q. Li, L. Liu, and M. Dong, "Size effect of graphene oxide on modulating amyloid peptide assembly," *Chemistry—A European Journal*, vol. 21, no. 27, pp. 9632–9637, 2015.
- [5] X. Wang, J. K. Weber, L. Liu, M. Dong, R. Zhou, and J. Li, "A novel form of β -strand assembly observed in A β 33–42 adsorbed onto graphene," *Nanoscale*, vol. 7, no. 37, pp. 15341–15348, 2015.
- [6] A. B. Singleton, M. Farrer, J. Johnson et al., " α -synuclein locus triplication causes Parkinson's disease," *Science*, vol. 302, no. 5646, p. 841, 2003.
- [7] G. Bates, "Huntingtin aggregation and toxicity in Huntington's disease," *The Lancet*, vol. 361, no. 9369, pp. 1642–1644, 2003.
- [8] Y. P. Goldberg, H. Telenius, and M. R. Hayden, "The molecular genetics of Huntington's disease," *Current Opinion in Neurology*, vol. 7, no. 4, pp. 325–332, 1994.
- [9] J. Collinge, "Prion diseases of humans and animals: their causes and molecular basis," *Annual Review of Neuroscience*, vol. 24, no. 1, pp. 519–550, 2001.
- [10] M. Neumann, D. M. Sampathu, L. K. Kwong et al., "Ubiquitinated TDP-43 in frontotemporal lobar degeneration and amyotrophic lateral sclerosis," *Science*, vol. 314, no. 5796, pp. 130–133, 2006.
- [11] H. F. Christoffersen, M. Andreasen, S. Zhang et al., "Scaffolded multimers of hIAPP_{20–29} peptide fragments fibrillate faster and lead to different fibrils compared to the free hIAPP_{20–29} peptide fragment," *Biochimica et Biophysica Acta—Proteins and Proteomics*, vol. 1854, no. 12, pp. 1890–1897, 2015.
- [12] M. Anguiano, R. J. Nowak, and P. T. Lansbury Jr., "Protofibrillar islet amyloid polypeptide permeabilizes synthetic vesicles by a pore-like mechanism that may be relevant to type II diabetes," *Biochemistry*, vol. 41, no. 38, pp. 11338–11343, 2002.
- [13] M. Chen, S. Zhang, Q. Liu et al., "An investigation into the formation of annular aggregates of human Islet amyloid polypeptide on tantalum oxide surfaces," *Chemistry—A European Journal*, vol. 18, no. 9, pp. 2493–2497, 2012.
- [14] P. Liu, S. Zhang, C. Wang et al., "Co-assembly of human islet amyloid polypeptide (hIAPP)/insulin," *Chemical Communications*, vol. 48, no. 2, pp. 191–193, 2012.
- [15] R. Khurana, C. Ionescu-Zanetti, M. Pope et al., "A general model for amyloid fibril assembly based on morphological studies using atomic force microscopy," *Biophysical Journal*, vol. 85, no. 2, pp. 1135–1144, 2003.
- [16] A. Natalello, V. V. Prokhorov, F. Tagliavini et al., "Conformational plasticity of the Gerstmann-Sträussler-Scheinker disease peptide as indicated by its multiple aggregation pathways," *Journal of Molecular Biology*, vol. 381, no. 5, pp. 1349–1361, 2008.
- [17] F. Sbrana, L. Bongini, G. Cappugi et al., "Atomic force microscopy images suggest aggregation mechanism in cerato-platanin," *European Biophysics Journal*, vol. 36, no. 7, pp. 727–732, 2007.
- [18] T. R. Serio, A. G. Cashikar, A. S. Kowal et al., "Nucleated conformational conversion and the replication of conformational information by a prion determinant," *Science*, vol. 289, no. 5483, pp. 1317–1321, 2000.
- [19] F. J. Giessibl, "Advances in atomic force microscopy," *Reviews of Modern Physics*, vol. 75, no. 3, pp. 949–983, 2003.
- [20] Y. Li, M. Dong, D. E. Otzen et al., "Influence of tunable external stimuli on the self-assembly of guanosine supramolecular nanostructures studied by atomic force microscope," *Langmuir*, vol. 25, no. 23, pp. 13432–13437, 2009.
- [21] Y. Li, Y. Li, Y. Yao et al., "Two-dimensional scaffold layer formations on a solid surface through xanthan polysaccharide: temperature effect," *Colloids and Surfaces B: Biointerfaces*, vol. 74, no. 1, pp. 136–139, 2009.
- [22] E. S. Andersen, M. Dong, M. M. Nielsen et al., "Self-assembly of a nanoscale DNA box with a controllable lid," *Nature*, vol. 459, no. 7243, pp. 73–76, 2009.
- [23] M. Dong, S. Husale, and O. Sahin, "Determination of protein structural flexibility by microsecond force spectroscopy," *Nature Nanotechnology*, vol. 4, no. 8, pp. 514–517, 2009.
- [24] W. J. Cho, B. P. Jena, and A. M. Jermic, "Nano-scale imaging and dynamics of amylin-membrane interactions and its implication in type II diabetes mellitus," *Methods in Cell Biology*, vol. 90, pp. 267–286, 2008.
- [25] L. Liu, L. Niu, M. Xu et al., "Molecular tethering effect of c-terminus of amyloid peptide A β 42," *ACS Nano*, vol. 8, no. 9, pp. 9503–9510, 2014.
- [26] M. Rief, F. Oesterhelt, B. Heymann, and H. E. Gaub, "Single molecule force spectroscopy on polysaccharides by atomic force microscopy," *Science*, vol. 275, no. 5304, pp. 1295–1297, 1997.
- [27] A. Janshoff, M. Neitzert, Y. Oberdörfer, and H. Fuchs, "Force spectroscopy of molecular systems—single molecule spectroscopy of polymers and biomolecules," *Angewandte Chemie—International Edition*, vol. 39, no. 18, pp. 3213–3237, 2000.
- [28] T. R. Strick, J.-F. Allemand, D. Bensimon, and V. Croquette, "Stress-induced structural transitions in DNA and proteins,"

- Annual Review of Biophysics and Biomolecular Structure*, vol. 29, no. 1, pp. 523–543, 2000.
- [29] M. S. Z. Kellermayer, L. Grama, Á. Karsai et al., “Reversible mechanical unzipping of amyloid β -fibrils,” *Journal of Biological Chemistry*, vol. 280, no. 9, pp. 8464–8470, 2005.
- [30] S. Wegmann, M. Miesbauer, K. F. Winklhofer, J. Tatzelt, and D. J. Muller, “Observing fibrillar assemblies on scrapie-infected cells,” *Pflügers Archiv—European Journal of Physiology*, vol. 456, no. 1, pp. 83–93, 2008.
- [31] T. Fukuma, A. S. Mostaert, L. C. Serpell, and S. P. Jarvis, “Revealing molecular-level surface structure of amyloid fibrils in liquid by means of frequency modulation atomic force microscopy,” *Nanotechnology*, vol. 19, no. 38, Article ID 384010, 2008.
- [32] D. Radovan, V. Smirnovas, and R. Winter, “Effect of pressure on islet amyloid polypeptide aggregation: revealing the polymorphic nature of the fibrillation process,” *Biochemistry*, vol. 47, no. 24, pp. 6352–6360, 2008.
- [33] S. Bhattacharya, J. Naveena Lavanya Latha, R. Kumresan, and S. Singh, “Cloning and expression of human islet amyloid polypeptide in cultured cells,” *Biochemical and Biophysical Research Communications*, vol. 356, no. 3, pp. 622–628, 2007.
- [34] T. T. Ding, S.-J. Lee, J.-C. Rochet, and P. T. Lansbury Jr., “Annular α -synuclein protofibrils are produced when spherical protofibrils are incubated in solution or bound to brain-derived membranes,” *Biochemistry*, vol. 41, no. 32, pp. 10209–10217, 2002.
- [35] M. M. Apetri, N. C. Maiti, M. G. Zagorski, P. R. Carey, and V. E. Anderson, “Secondary structure of α -synuclein oligomers: characterization by Raman and atomic force microscopy,” *Journal of Molecular Biology*, vol. 355, no. 1, pp. 63–71, 2006.
- [36] I. Segers-Nolten, K. van der Werf, M. van Raaij, and V. Subramaniam, “Quantitative characterization of protein nanostructures using atomic force microscopy,” in *Proceedings of the 29th Annual International Conference of the IEEE Engineering in Medicine and Biology Society (EMBS '07)*, pp. 6608–6611, IEEE, Lyon, France, August 2007.
- [37] C. Ortiz, D. Zhang, A. E. Ribbe, Y. Xie, and D. Ben-Amotz, “Analysis of insulin amyloid fibrils by Raman spectroscopy,” *Biophysical Chemistry*, vol. 128, no. 2-3, pp. 150–155, 2007.
- [38] R. Jansen, W. Dzwolak, and R. Winter, “Amyloidogenic self-assembly of insulin aggregates probed by high resolution atomic force microscopy,” *Biophysical Journal*, vol. 88, no. 2, pp. 1344–1353, 2005.
- [39] M.-S. Lin, H.-M. Chiu, F.-J. Fan et al., “Kinetics and enthalpy measurements of interaction between β -amyloid and liposomes by surface plasmon resonance and isothermal titration microcalorimetry,” *Colloids and Surfaces B: Biointerfaces*, vol. 58, no. 2, pp. 231–236, 2007.
- [40] P. Mesquida, C. K. Riener, C. E. MacPhee, and R. A. McKendry, “Morphology and mechanical stability of amyloid-like peptide fibrils,” *Journal of Materials Science: Materials in Medicine*, vol. 18, no. 7, pp. 1325–1331, 2007.
- [41] P. Mesquida, E. M. Blanco, and R. A. McKendry, “Patterning amyloid peptide fibrils by AFM charge writing,” *Langmuir*, vol. 22, no. 22, pp. 9089–9091, 2006.
- [42] L. Zhang, J. Zhong, L. Huang, L. Wang, Y. Hong, and Y. Sha, “Parallel-oriented fibrogenesis of a β -sheet forming peptide on supported lipid bilayers,” *Journal of Physical Chemistry B*, vol. 112, no. 30, pp. 8950–8954, 2008.
- [43] M. R. Nichols, M. A. Moss, D. K. Reed, J. H. Hoh, and T. L. Rosenberry, “Rapid assembly of amyloid- β peptide at a liquid/liquid interface produces unstable β -sheet fibers,” *Biochemistry*, vol. 44, no. 1, pp. 165–173, 2005.
- [44] N. Benseny-Cases, M. Cócera, and J. Cladera, “Conversion of non-fibrillar β -sheet oligomers into amyloid fibrils in Alzheimer’s disease amyloid peptide aggregation,” *Biochemical and Biophysical Research Communications*, vol. 361, no. 4, pp. 916–921, 2007.
- [45] I. A. Mastrangelo, M. Ahmed, T. Sato et al., “High-resolution atomic force microscopy of soluble A β 42 oligomers,” *Journal of Molecular Biology*, vol. 358, no. 1, pp. 106–119, 2006.
- [46] M. Arimon, I. Díez-Pérez, M. J. Kogan et al., “Fine structure study of A β 1–42 fibrillogenesis with atomic force microscopy,” *The FASEB Journal*, vol. 19, no. 10, pp. 1344–1346, 2005.
- [47] Z. Wang, C. Zhou, C. Wang, L. Wan, X. Fang, and C. Bai, “AFM and STM study of β -amyloid aggregation on graphite,” *Ultramicroscopy*, vol. 97, no. 1–4, pp. 73–79, 2003.
- [48] Z. Wang, L. Wan, C. Zhou, X. Fang, C. Wang, and C. Bai, “Study of β -amyloid adsorption and aggregation on graphite by STM and AFM,” *Chinese Science Bulletin*, vol. 48, no. 5, pp. 437–440, 2003.
- [49] W. S. Gosal, A. H. Clark, and S. B. Ross-Murphy, “Fibrillar β -lactoglobulin gels—part 1: fibril formation and structure,” *Biomacromolecules*, vol. 5, no. 6, pp. 2408–2419, 2004.
- [50] O. Daniela, W. Lizhe, B. André, M. Edmond, and M. A. E. Auty, “Characterization β -lactoglobulin fibrillar assembly using atomic force microscopy polyacrylamide gel electrophoresis, and in situ fourier transform infrared spectroscopy,” *Journal of Agricultural and Food Chemistry*, vol. 58, no. 6, pp. 3667–3673, 2010.
- [51] W. S. Gosal, A. H. Clark, P. D. A. Pudney, and S. B. Ross-Murphy, “Novel amyloid fibrillar networks derived from a globular protein: β -lactoglobulin,” *Langmuir*, vol. 18, no. 19, pp. 7174–7181, 2002.
- [52] S. E. Radford, W. S. Gosal, and G. W. Platt, “Towards an understanding of the structural molecular mechanism of β 2-microglobulin amyloid formation in vitro,” *Biochimica et Biophysica Acta (BBA)—Proteins and Proteomics*, vol. 1753, no. 1, pp. 51–63, 2005.
- [53] N. M. Kad, S. L. Myers, D. P. Smith, D. A. Smith, S. E. Radford, and N. H. Thomson, “Hierarchical assembly of β 2-microglobulin amyloid *in vitro* revealed by atomic force microscopy,” *Journal of Molecular Biology*, vol. 330, no. 4, pp. 785–797, 2003.
- [54] Y. Hong, R. L. Legge, S. Zhang, and P. Chen, “Effect of amino acid sequence and pH on nanofiber formation of self-assembling peptides EAK16-II and EAK16-IV,” *Biomacromolecules*, vol. 4, no. 5, pp. 1433–1442, 2003.
- [55] R. P. Nagarkar, R. A. Hule, D. J. Pochan, and J. P. Schneider, “De novo design of strand-swapped β -hairpin hydrogels,” *Journal of the American Chemical Society*, vol. 130, no. 13, pp. 4466–4474, 2008.
- [56] M. Dong, M. B. Hovgaard, S. Xu, D. E. Otzen, and F. Besenbacher, “AFM study of glucagon fibrillation via oligomeric structures resulting in interwoven fibrils,” *Nanotechnology*, vol. 17, no. 16, pp. 4003–4009, 2006.
- [57] M. Mauro, E. F. Craparo, A. Podestà et al., “Kinetics of different processes in human insulin amyloid formation,” *Journal of Molecular Biology*, vol. 366, no. 1, pp. 258–274, 2007.
- [58] F. Evers, C. Jeworrek, S. Tiemeyer et al., “Elucidating the mechanism of lipid membrane-induced IAPP fibrillogenesis and its inhibition by the red wine compound resveratrol: a

- synchrotron X-ray reflectivity study,” *Journal of the American Chemical Society*, vol. 131, no. 27, pp. 9516–9521, 2009.
- [59] I. H. Cheng, K. Scarce-Levie, J. Legleiter et al., “Accelerating amyloid- β fibrillization reduces oligomer levels and functional deficits in Alzheimer disease mouse models,” *Journal of Biological Chemistry*, vol. 282, no. 33, pp. 23818–23828, 2007.
- [60] F. L. Palhano, C. B. Rocha, A. Bernardino et al., “A fluorescent mutant of the NM domain of the yeast prion Sup35 provides insight into fibril formation and stability,” *Biochemistry*, vol. 48, no. 29, pp. 6811–6823, 2009.
- [61] Y. Liang, S. Z. Jasbi, S. Haftchenary, S. Morin, and D. J. Wilson, “Binding interactions in early- and late-stage amyloid aggregates of TTR(105–115),” *Biophysical Chemistry*, vol. 144, no. 1–2, pp. 1–8, 2009.
- [62] C. Lonescu-Zanetti, R. Khurana, J. R. Gillespie et al., “Monitoring the assembly of Ig light-chain amyloid fibrils by atomic force microscopy,” *Proceedings of the National Academy of Sciences of the United States of America*, vol. 96, no. 23, pp. 13175–13179, 1999.
- [63] S. Hess, S. L. Lindquist, and T. Scheibel, “Alternative assembly pathways of the amyloidogenic yeast prion determinant Sup35-NM,” *EMBO Reports*, vol. 8, no. 12, pp. 1196–1201, 2007.
- [64] M. Sandal, F. Valle, I. Tessari et al., “Conformational equilibria in monomeric α -synuclein at the single-molecule level,” *PLoS Biology*, vol. 6, no. 1, article e6, 2008.
- [65] G. Binnig, C. F. Quate, and C. Gerber, “Atomic force microscope,” *Physical Review Letters*, vol. 56, no. 9, pp. 930–933, 1986.
- [66] A. Alessandrini and P. Facci, “AFM: a versatile tool in biophysics,” *Measurement Science and Technology*, vol. 16, no. 6, pp. R65–R92, 2005.
- [67] W. A. Linke and A. Grützner, “Pulling single molecules of titin by AFM—recent advances and physiological implications,” *Pflügers Archiv: European Journal of Physiology*, vol. 456, no. 1, pp. 101–115, 2008.
- [68] Q. Li, J. Song, M. Saura-Múzquiz, F. Besenbacher, M. Christensen, and M. Dong, “Magnetic properties of strontium hexaferrite nanostructures measured with magnetic force microscopy,” *Scientific Reports*, vol. 6, Article ID 25985, 2016.
- [69] H. Liang, G. Zeng, Y. Li et al., “Exploring the complex mechanical properties of xanthan scaffolds by AFM-based force spectroscopy,” *Beilstein Journal of Nanotechnology*, vol. 5, no. 1, pp. 365–373, 2014.
- [70] F. Lippert, D. M. Parker, and K. D. Jandt, “In vitro demineralization/reminerallization cycles at human tooth enamel surfaces investigated by AFM and nanoindentation,” *Journal of Colloid and Interface Science*, vol. 280, no. 2, pp. 442–448, 2004.
- [71] D. Xia, S. Zhang, E. Nielsen et al., “The ultrastructures and mechanical properties of the descemet’s membrane in fuchs endothelial corneal dystrophy,” *Scientific Reports*, vol. 6, Article ID 23096, 2016.
- [72] J. P. Froning, D. Xia, S. Zhang, E. Lægsgaard, F. Besenbacher, and M. Dong, “Piezoelectric oscillation sensor based noncontact atomic force microscope for imaging in both ambient and liquid environments,” *Journal of Vacuum Science and Technology B: Nanotechnology and Microelectronics*, vol. 33, no. 2, Article ID 021801, 2015.
- [73] M. Andreasen, K. K. Skeby, S. Zhang et al., “The importance of being capped: terminal capping of an amyloidogenic peptide affects fibrillation propensity and fibril morphology,” *Biochemistry*, vol. 53, no. 44, pp. 6968–6980, 2014.
- [74] A. Ashkin, K. Schutze, J. M. Dziedzic, U. Euteneuer, and M. Schliwa, “Force generation of organelle transport measured *in vivo* by an infrared laser trap,” *Nature*, vol. 348, no. 6299, pp. 346–348, 1990.
- [75] E. Evans, K. Ritchie, and R. Merkel, “Sensitive force technique to probe molecular adhesion and structural linkages at biological interfaces,” *Biophysical Journal*, vol. 68, no. 6, pp. 2580–2587, 1995.
- [76] A. Kishino and T. Yanagida, “Force measurements by micromanipulation of a single actin filament by glass needles,” *Nature*, vol. 334, no. 6177, pp. 74–76, 1988.
- [77] S. B. Smith, L. Finzi, and C. Bustamante, “Direct mechanical measurements of the elasticity of single DNA molecules by using magnetic beads,” *Science*, vol. 258, no. 5085, pp. 1122–1126, 1992.
- [78] P. Hinterdorfer and Y. F. Dufrêne, “Detection and localization of single molecular recognition events using atomic force microscopy,” *Nature Methods*, vol. 3, no. 5, pp. 347–355, 2006.
- [79] M. S. Z. Kellermayer, Á. Karsai, Ü. Murvai, S. Erdélyi-Bótor, J. Kardos, and R. H. Pires, “Single-molecule studies of amyloidogenic proteins,” in *Single-Molecule Studies of Proteins*, A. F. Oberhauser, Ed., vol. 2 of *Biophysics for the Life Sciences*, pp. 169–210, Springer, New York, NY, USA, 2012.
- [80] M. Kellermayer and C. F. Hazlewood, *Traction Decreases (Table I.). The Increased Dry Mass of the AC, Water and Ions in Biological Systems*, 2013.
- [81] Y. Li, C. Zhu, J. Zhu et al., “Nanomechanics of phospholipid LB film studied layer by layer with AFM,” *Chemistry Central Journal*, vol. 8, no. 1, article 71, 2014.
- [82] D.-S. Yang, C. M. Yip, T. H. J. Huang, A. Chakrabarty, and P. E. Fraser, “Manipulating the amyloid- β aggregation pathway with chemical chaperones,” *The Journal of Biological Chemistry*, vol. 274, no. 46, pp. 32970–32974, 1999.
- [83] A. S. Mostaert, M. J. Higgins, T. Fukuma, F. Rindi, and S. P. Jarvis, “Nanoscale mechanical characterisation of amyloid fibrils discovered in a natural adhesive,” *Journal of Biological Physics*, vol. 32, no. 5, pp. 393–401, 2006.
- [84] P. Flory and M. Volkenstein, *Statistical Mechanics of Chain Molecules*, Wiley Online Library, 1969.
- [85] C. Bouchiat, M. D. Wang, J.-F. Allemand, T. Strick, S. M. Block, and V. Croquette, “Estimating the persistence length of a worm-like chain molecule from force-extension measurements,” *Biophysical Journal*, vol. 76, no. 1, pp. 409–413, 1999.
- [86] S. P. Sibley, K. Sosinsky, L. E. Gulian, E. J. Gibbs, and R. F. Pasternack, “Probing the mechanism of insulin aggregation with added metalloporphyrins,” *Biochemistry*, vol. 47, no. 9, pp. 2858–2865, 2008.
- [87] C. McAllister, M. A. Karymov, Y. Kawano et al., “Protein interactions and misfolding analyzed by AFM force spectroscopy,” *Journal of Molecular Biology*, vol. 354, no. 5, pp. 1028–1042, 2005.
- [88] F. Rúa, S. Bousert, T. Parella et al., “Self-assembly of a cyclobutane β -tetrapeptide to form nanosized structures,” *Organic Letters*, vol. 9, no. 18, pp. 3643–3645, 2007.
- [89] L. Liu, Q. Li, S. Zhang et al., “Identification of a novel parallel β -strand conformation within molecular monolayer of amyloid peptide,” *Advanced Science*, vol. 3, no. 6, 2016.
- [90] R. Kodali and R. Wetzel, “Polymorphism in the intermediates and products of amyloid assembly,” *Current Opinion in Structural Biology*, vol. 17, no. 1, pp. 48–57, 2007.
- [91] R. Gerber, K. Voitchovsky, C. Mitchel et al., “Inter-oligomer interactions of the human prion protein are modulated by the

- polymorphism at codon 129,” *Journal of Molecular Biology*, vol. 381, no. 1, pp. 212–220, 2008.
- [92] P. Marek, A. Abedini, B. Song et al., “Aromatic interactions are not required for amyloid fibril formation by islet amyloid polypeptide but do influence the rate of fibril formation and fibril morphology,” *Biochemistry*, vol. 46, no. 11, pp. 3255–3261, 2007.
- [93] R. Harada, N. Kobayashi, J. Kim et al., “The effect of amino acid substitution in the imperfect repeat sequences of α -synuclein on fibrillation,” *Biochimica et Biophysica Acta (BBA)—Molecular Basis of Disease*, vol. 1792, no. 10, pp. 998–1003, 2009.
- [94] R. Liu, C. McAllister, Y. Lyubchenko, and M. R. Sierks, “Residues 17–20 and 30–35 of beta-amyloid play critical roles in aggregation,” *Journal of Neuroscience Research*, vol. 75, no. 2, pp. 162–171, 2004.
- [95] W. Qi, A. Zhang, D. Patel et al., “Simultaneous monitoring of peptide aggregate distributions, structure, and kinetics using amide hydrogen exchange: application to $A\beta$ (1–40) fibrillogenesis,” *Biotechnology and Bioengineering*, vol. 100, no. 6, pp. 1214–1227, 2008.
- [96] J. Ryu, H.-A. Joung, M.-G. Kim, and B. P. Chan, “Surface plasmon resonance analysis of Alzheimer’s β -amyloid aggregation on a solid surface: from monomers to fully-grown fibrils,” *Analytical Chemistry*, vol. 80, no. 7, pp. 2400–2407, 2008.
- [97] N. Chaudhary, S. Singh, and R. Nagaraj, “Morphology of self-assembled structures formed by short peptides from the amyloidogenic protein tau depends on the solvent in which the peptides are dissolved,” *Journal of Peptide Science*, vol. 15, no. 10, pp. 675–684, 2009.
- [98] J. D. Harper, S. S. Wong, C. M. Lieber, and P. T. Lansbury Jr., “Observation of metastable $A\beta$ amyloid protofibrils by atomic force microscopy,” *Chemistry and Biology*, vol. 4, no. 2, pp. 119–125, 1997.
- [99] Á. Karsai, Ü. Murvai, K. Soós, B. Penke, and M. S. Z. Kellermayer, “Oriented epitaxial growth of amyloid fibrils of the N27C mutant β 25–35 peptide,” *European Biophysics Journal*, vol. 37, no. 7, pp. 1133–1137, 2008.
- [100] H. A. Lashuel, D. M. Hartley, B. M. Petre et al., “Mixtures of wild-type and a pathogenic (E22G) form of $A\beta$ 40 in vitro accumulate protofibrils, including amyloid pores,” *Journal of Molecular Biology*, vol. 332, no. 4, pp. 795–808, 2003.
- [101] K. A. Conway, S.-J. Lee, J.-C. Rochet, T. T. Ding, R. E. Williamson, and P. T. Lansbury Jr., “Acceleration of oligomerization, not fibrillation, is a shared property of both α -synuclein mutations linked to early-onset Parkinson’s disease: implications for pathogenesis and therapy,” *Proceedings of the National Academy of Sciences of the United States of America*, vol. 97, no. 2, pp. 571–576, 2000.
- [102] H. Heise, M. S. Celej, S. Becker et al., “Solid-state NMR reveals structural differences between fibrils of wild-type and disease-related A53T mutant α -synuclein,” *Journal of Molecular Biology*, vol. 380, no. 3, pp. 444–450, 2008.
- [103] K. Sathasivam, A. Lane, J. Legleiter et al., “Identical oligomeric and fibrillar structures captured from the brains of R6/2 and knock-in mouse models of Huntington’s disease,” *Human Molecular Genetics*, vol. 19, no. 1, pp. 65–78, 2009.
- [104] M. A. Poirier, H. Li, J. Macosko, S. Cai, M. Amzel, and C. A. Ross, “Huntingtin spheroids and protofibrils as precursors in polyglutamine fibrillation,” *Journal of Biological Chemistry*, vol. 277, no. 43, pp. 41032–41037, 2002.
- [105] G. Lodderstedt, S. Hess, G. Hause, T. Scheuermann, T. Scheibel, and E. Schwarz, “Effect of oropharyngeal muscular dystrophy-associated extension of seven alanines on the fibrillation properties of the N-terminal domain of PABPN1,” *The FEBS Journal*, vol. 274, no. 2, pp. 346–355, 2007.
- [106] N. M. Kad, N. H. Thomson, D. P. Smith, D. A. Smith, and S. E. Radford, “ β 2-microglobulin and its deamidated variant, N17D form amyloid fibrils with a range of morphologies in vitro,” *Journal of Molecular Biology*, vol. 313, no. 3, pp. 559–571, 2001.
- [107] J. D. Green, L. Kreplak, C. Goldsbury et al., “Atomic force microscopy reveals defects within mica supported lipid bilayers induced by the amyloidogenic human amylin peptide,” *Journal of Molecular Biology*, vol. 342, no. 3, pp. 877–887, 2004.
- [108] Q. Li, L. Liu, S. Zhang et al., “Modulating $a\beta$ 33–42 peptide assembly by graphene oxide,” *Chemistry—A European Journal*, vol. 20, no. 24, pp. 7236–7240, 2014.
- [109] M. Anderson, O. V. Bocharova, N. Makarava, L. Breydo, V. V. Salnikov, and I. V. Baskakov, “Polymorphism and ultrastructural organization of prion protein amyloid fibrils: an insight from high resolution atomic force microscopy,” *Journal of Molecular Biology*, vol. 358, no. 2, pp. 580–596, 2006.
- [110] J. D. Green, C. Goldsbury, J. Kistler, G. J. S. Cooper, and U. Aebi, “Human amylin oligomer growth and fibril elongation define two distinct phases in amyloid formation,” *The Journal of Biological Chemistry*, vol. 279, no. 13, pp. 12206–12212, 2004.
- [111] H. K. L. Blackley, G. H. W. Sanders, M. C. Davies, C. J. Roberts, S. J. B. Tendler, and M. J. Wilkinson, “In-situ atomic force microscopy study of β -amyloid fibrillation,” *Journal of Molecular Biology*, vol. 298, no. 5, pp. 833–840, 2000.
- [112] C. S. Goldsbury, G. J. S. Cooper, K. N. Goldie et al., “Polymorphic fibrillar assembly of human amylin,” *Journal of Structural Biology*, vol. 119, no. 1, pp. 17–27, 1997.
- [113] C. S. Goldsbury, S. Wirtz, S. A. Müller et al., “Studies on the *in vitro* assembly of $A\beta$ 1–40: implications for the search for $A\beta$ fibril formation inhibitors,” *Journal of Structural Biology*, vol. 130, no. 2–3, pp. 217–231, 2000.
- [114] R. H. Pires, Á. Karsai, M. J. Saraiva, A. M. Damas, and M. S. Z. Kellermayer, “Distinct annular oligomers captured along the assembly and disassembly pathways of transthyretin amyloid protofibrils,” *PLoS ONE*, vol. 7, no. 9, Article ID e44992, 2012.
- [115] Y. Han, C. He, M. Cao, X. Huang, Y. Wang, and Z. Li, “Facile disassembly of amyloid fibrils using gemini surfactant micelles,” *Langmuir*, vol. 26, no. 3, pp. 1583–1587, 2010.
- [116] M. O. Chaney, W. B. Stine, T. A. Kokjohn et al., “RAGE and amyloid beta interactions: atomic force microscopy and molecular modeling,” *Biochimica et Biophysica Acta—Molecular Basis of Disease*, vol. 1741, no. 1–2, pp. 199–205, 2005.
- [117] M. Dong, M. B. Hovgaard, W. Mamdouh, S. Xu, D. E. Otzen, and F. Besenbacher, “AFM-based force spectroscopy measurements of mature amyloid fibrils of the peptide glucagon,” *Nanotechnology*, vol. 19, no. 38, Article ID 384013, 2008.
- [118] L. Pazzagli, C. Zoppi, L. Carresi et al., “Characterization of ordered aggregates of cerato-platanin and their involvement in fungus-host interactions,” *Biochimica et Biophysica Acta (BBA)—General Subjects*, vol. 1790, no. 10, pp. 1334–1344, 2009.
- [119] M. Kanapathipillai, S. H. Ku, K. Girigoswami, and C. B. Park, “Small stress molecules inhibit aggregation and neurotoxicity of prion peptide 106–126,” *Biochemical and Biophysical Research Communications*, vol. 365, no. 4, pp. 808–813, 2008.
- [120] I. Cardoso, C. S. Goldsbury, S. A. Müller et al., “Transthyretin fibrillogenesis entails the assembly of monomers: a molecular model for *in vitro* assembled transthyretin amyloid-like fibrils,” *Journal of Molecular Biology*, vol. 317, no. 5, pp. 683–695, 2002.

- [121] W. S. Gosal, I. J. Morten, E. W. Hewitt, D. A. Smith, N. H. Thomson, and S. E. Radford, "Competing pathways determine fibril morphology in the self-assembly of β 2-microglobulin into amyloid," *Journal of Molecular Biology*, vol. 351, no. 4, pp. 850–864, 2005.
- [122] A. S. Mostaert, C. Giordani, R. Crockett, U. Karsten, R. Schumann, and S. P. Jarvis, "Characterisation of amyloid nanostructures in the natural adhesive of unicellular subaerial algae," *The Journal of Adhesion*, vol. 85, no. 8, pp. 465–483, 2009.
- [123] E. Rhoades and A. Gafni, "Micelle formation by a fragment of human islet amyloid polypeptide," *Biophysical Journal*, vol. 84, no. 5, pp. 3480–3487, 2003.
- [124] C. Bortolini, N. C. Jones, S. V. Hoffmann, F. Besenbacher, and M. Dong, "The influence of the localised charge of C- and N-termini on peptide self-assembly," *Soft Matter*, vol. 12, no. 2, pp. 373–379, 2015.
- [125] L. Niu, L. Liu, W. Xi et al., "Synergistic inhibitory effect of peptide-organic coassemblies on amyloid aggregation," *ACS Nano*, vol. 10, no. 4, pp. 4143–4153, 2016.
- [126] L. Liu, Y. Li, D. Xia et al., "A self-assembled nanopatch with peptide-organic multilayers and mechanical properties," *Nanoscale*, vol. 7, no. 6, pp. 2250–2254, 2015.
- [127] A. Chiovitti, P. Heraud, T. M. Dugdale et al., "Divalent cations stabilize the aggregation of sulfated glycoproteins in the adhesive nanofibers of the biofouling diatom *Toxarium undulatum*," *Soft Matter*, vol. 4, no. 4, pp. 811–820, 2008.
- [128] E. Žerovnik, M. Škarabot, K. Škerget et al., "Amyloid fibril formation by human stefin B: influence of pH and TFE on fibril growth and morphology," *Amyloid*, vol. 14, no. 3, pp. 237–247, 2007.
- [129] Y. Hong, M. D. Pritzker, R. L. Legge, and P. Chen, "Effect of NaCl and peptide concentration on the self-assembly of an ionic-complementary peptide EAK16-II," *Colloids and Surfaces B: Biointerfaces*, vol. 46, no. 3, pp. 152–161, 2005.
- [130] A. Keller, M. Fritzsche, Y.-P. Yu et al., "Influence of hydrophobicity on the surface-catalyzed assembly of the islet amyloid polypeptide," *ACS Nano*, vol. 5, no. 4, pp. 2770–2778, 2011.
- [131] F. Bellezza, A. Cipiciani, M. A. Quotadamo, S. Cinelli, G. Onori, and S. Tacchi, "Structure, stability, and activity of myoglobin adsorbed onto phosphate-grafted zirconia nanoparticles," *Langmuir*, vol. 23, no. 26, pp. 13007–13012, 2007.
- [132] S. Kumar, V. K. Ravi, and R. Swaminathan, "Suppression of lysozyme aggregation at alkaline pH by tri-*N*-acetylchitotriose," *Biochimica et Biophysica Acta (BBA)—Proteins and Proteomics*, vol. 1794, no. 6, pp. 913–920, 2009.
- [133] C. Bortolini, L. Liu, T. M. A. Gronewold, C. Wang, F. Besenbacher, and M. Dong, "The position of hydrophobic residues tunes peptide self-assembly," *Soft Matter*, vol. 10, no. 31, pp. 5656–5661, 2014.
- [134] S. Jun, J. R. Gillespie, B.-K. Shin, and S. Saxena, "The second Cu(II)-binding site in a proton-rich environment interferes with the aggregation of amyloid- β (1–40) into amyloid fibrils," *Biochemistry*, vol. 48, no. 45, pp. 10724–10732, 2009.
- [135] Á. Karsai, L. Grama, Ü. Murvai, K. Soós, B. Penke, and M. S. Z. Kellermayer, "Potassium-dependent oriented growth of amyloid β 25–35 fibrils on mica," *Nanotechnology*, vol. 18, no. 34, Article ID 345102, 2007.
- [136] E. Kvam, B. L. Nannenga, M. S. Wang, Z. Jia, M. R. Sierks, and A. Messer, "Conformational targeting of fibrillar polyglutamine proteins in live cells escalates aggregation and cytotoxicity," *PLoS ONE*, vol. 4, no. 5, Article ID e5727, 2009.
- [137] M. S. Z. Kellermayer, Á. Karsai, M. Benke, K. Soós, and B. Penke, "Stepwise dynamics of epitaxially growing single amyloid fibrils," *Proceedings of the National Academy of Sciences of the United States of America*, vol. 105, no. 1, pp. 141–144, 2008.
- [138] M. Kolsofszki, Á. Karsai, K. Soós, B. Penke, and M. S. Z. Kellermayer, "Thermally-induced effects in oriented network of amyloid β 25–35 fibrils," in *Colloids for Nano- and Biotechnology, Progress in Colloid and Polymer Science*, vol. 135, pp. 169–173, Springer, Berlin, Germany, 2008.
- [139] S. Jenko, M. Škarabot, M. Kenig et al., "Different propensity to form amyloid fibrils by two homologous proteins—human stefins A and B: searching for an explanation," *Proteins: Structure, Function, and Bioinformatics*, vol. 55, no. 2, pp. 417–425, 2004.
- [140] B. A. Chromy, R. J. Nowak, M. P. Lambert et al., "Self-assembly of A β 1–42 into globular neurotoxins," *Biochemistry*, vol. 42, no. 44, pp. 12749–12760, 2003.
- [141] M. Cao, Y. Han, J. Wang, and Y. Wang, "Modulation of fibrillogenesis of amyloid β (1–40) peptide with cationic gemini surfactant," *The Journal of Physical Chemistry B*, vol. 111, no. 47, pp. 13436–13443, 2007.
- [142] A. Parbhu, H. Lin, J. Thimm, and R. Lal, "Imaging real-time aggregation of amyloid beta protein (1–42) by atomic force microscopy," *Peptides*, vol. 23, no. 7, pp. 1265–1270, 2002.
- [143] Y. Miura, K. Yasuda, K. Yamamoto, M. Koike, Y. Nishida, and K. Kobayashi, "Inhibition of Alzheimer amyloid aggregation with sulfate glycopolymers," in *Advances in Science and Technology*, Trans Tech Publications, 2009.
- [144] S. Kumar, V. K. Ravi, and R. Swaminathan, "How do surfactants and DTT affect the size, dynamics, activity and growth of soluble lysozyme aggregates?" *Biochemical Journal*, vol. 415, no. 2, pp. 275–288, 2008.
- [145] W. D. Marcus, H. Wang, S. M. Lindsay, and M. R. Sierks, "Characterization of an antibody scFv that recognizes fibrillar insulin and β -amyloid using atomic force microscopy," *Nanomedicine: Nanotechnology, Biology, and Medicine*, vol. 4, no. 1, pp. 1–7, 2008.
- [146] L. Tang, H.-T. Li, H.-N. Du, F. Zhang, X.-F. Hu, and H.-Y. Hu, "Study of the disassembly-assembly process of α -synuclein fibrils by in situ atomic force microscopy," *Micron*, vol. 37, no. 7, pp. 675–679, 2006.
- [147] D. E. Dunstan, P. Hamilton-Brown, P. Asimakis, W. Ducker, and J. Bertolini, "Shear flow promotes amyloid- β fibrilization," *Protein Engineering, Design and Selection*, vol. 22, no. 12, pp. 741–746, 2009.
- [148] G. A. Kiselev, P. V. Kudrinskii, I. V. Yaminskii, and O. I. Vinogradova, "Studying intermolecular processes in thin surface layers with microcantilever transducers. Formation of protein fibrils on a solid support," *Protection of Metals*, vol. 44, no. 6, pp. 535–541, 2008.
- [149] C. M. Yip, A. A. Darabie, and J. McLaurin, "A β 42-peptide assembly on lipid bilayers," *Journal of Molecular Biology*, vol. 318, no. 1, pp. 97–107, 2002.
- [150] Ü. Murvai, J. Somkuti, L. Smeller, B. Penke, and M. S. Z. Kellermayer, "Structural and nanomechanical comparison of epitaxially and solution-grown amyloid β 25–35 fibrils," *Biochimica et Biophysica Acta (BBA)—Proteins and Proteomics*, vol. 1854, no. 5, pp. 327–332, 2015.
- [151] Y.-P. Yu, S. Zhang, Q. Liu et al., "2D amyloid aggregation of human islet amyloid polypeptide at the solid-liquid interface," *Soft Matter*, vol. 8, no. 5, pp. 1616–1622, 2012.

- [152] G. Maurstad, M. Prass, L. C. Serpell, and P. Sikorski, "Dehydration stability of amyloid fibrils studied by AFM," *European Biophysics Journal*, vol. 38, no. 8, pp. 1135–1140, 2009.
- [153] R. J. A. Hill, V. L. Sedman, S. Allen et al., "Alignment of aromatic peptide tubes in strong magnetic fields," *Advanced Materials*, vol. 19, no. 24, pp. 4474–4479, 2007.
- [154] P. E. Marszalek, H. Li, A. F. Oberhauser, and J. M. Fernandez, "Chair-boat transitions in single polysaccharide molecules observed with force-ramp AFM," *Proceedings of the National Academy of Sciences of the United States of America*, vol. 99, no. 7, pp. 4278–4283, 2002.
- [155] P. E. Marszalek, A. F. Oberhauser, Y.-P. Pang, and J. M. Fernandez, "Polysaccharide elasticity governed by chair-boat transitions of the glucopyranose ring," *Nature*, vol. 396, no. 6712, pp. 661–664, 1998.
- [156] T. Fukuma, A. S. Mostaert, and S. P. Jarvis, "Explanation for the mechanical strength of amyloid fibrils," *Tribology Letters*, vol. 22, no. 3, pp. 233–237, 2006.
- [157] A. S. Mostaert and S. P. Jarvis, "Beneficial characteristics of mechanically functional amyloid fibrils evolutionarily preserved in natural adhesives," *Nanotechnology*, vol. 18, no. 4, Article ID 044010, 2007.
- [158] Á. Karsai, Z. Mártonfalvi, A. Nagy, L. Grama, B. Penke, and M. S. Z. Kellermayer, "Mechanical manipulation of Alzheimer's amyloid β 1–42 fibrils," *Journal of Structural Biology*, vol. 155, no. 2, pp. 316–326, 2006.
- [159] R. M. A. Sullan, N. Gunari, A. E. Tanur et al., "Nanoscale structures and mechanics of barnacle cement," *Biofouling*, vol. 25, no. 3, pp. 263–275, 2009.
- [160] B. L. Smith, T. E. Schäffer, M. Vlani et al., "Molecular mechanistic origin of the toughness of natural adhesives, fibres and composites," *Nature*, vol. 399, no. 6738, pp. 761–763, 1999.
- [161] S. Guo and B. B. Akhremitchev, "Packing density and structural heterogeneity of insulin amyloid fibrils measured by AFM nanoindentation," *Biomacromolecules*, vol. 7, no. 5, pp. 1630–1636, 2006.
- [162] S. Guo and B. B. Akhremitchev, "Investigation of mechanical properties of insulin crystals by atomic force microscopy," *Langmuir*, vol. 24, no. 3, pp. 880–887, 2008.
- [163] J. Kardos, K. Yamamoto, K. Hasegawa, H. Naiki, and Y. Goto, "Direct measurement of the thermodynamic parameters of amyloid formation by isothermal titration calorimetry," *The Journal of Biological Chemistry*, vol. 279, no. 53, pp. 55308–55314, 2004.

Research Article

Micro-CT Imaging of RGD-Conjugated Gold Nanorods Targeting Tumor *In Vivo*

Xiaochao Qu, Xiaoxiao Li, Jingning Liang, Yanran Wang, Muhan Liu, and Jimin Liang

School of Life Science and Technology, Xidian University, Xi'an, Shaanxi 710071, China

Correspondence should be addressed to Xiaochao Qu; xiaochaoqu@gmail.com and Jimin Liang; jiminliang@gmail.com

Received 18 April 2016; Revised 21 June 2016; Accepted 22 June 2016

Academic Editor: Shuai Zhang

Copyright © 2016 Xiaochao Qu et al. This is an open access article distributed under the Creative Commons Attribution License, which permits unrestricted use, distribution, and reproduction in any medium, provided the original work is properly cited.

Gold nanomaterials as computed tomography (CT) contrast agents at lower X-ray dosage to get a higher contrast have advantages of longer imaging time and lower toxic side effects compared to current contrast agents. As a receptor for Cyclo (Arg-Gly-Asp-D-Phe-Lys) (RGD) peptide, integrin $\alpha_v\beta_3$ is overexpressed on some tumor cells and tumor neovasculature. In this paper, we conjugated the RGD peptide on the surface of gold nanorods (AuNRs), designated as RGD-AuNRs, a promising candidate in applications such as tumor targeting and imaging capability for micro-CT imaging. Integrin $\alpha_v\beta_3$ -positive U87 cells and integrin $\alpha_v\beta_3$ -negative HT-29 cells were chosen to establish animal models relatedly and then tested the tumor targeting ability and imaging capability of RGD-AuNRs *in vitro* and *in vivo*. The MTT assay and stability measurement showed that RGD-conjugation eliminated their cytotoxicity and improved their biocompatibility and stability. Dark-field imaging of U87 cells and HT-29 cells testified the binding affinities and uptake abilities of RGD-AuNRs, and the results showed that RGD-AuNRs were more specific to U87 cells. The enhanced micro-CT imaging contrast of intramuscular and subcutaneous injection illustrated the feasibility of RGD-AuNRs to be contrast agents. Furthermore, the micro-CT imaging of targeting U87 and HT-29 tumor models verified the targeting abilities of RGD-AuNRs.

1. Introduction

Medical imaging plays an important role in overall cancer diagnostics and planning and analysis of the therapeutic effect. Some structural imaging modalities, such as computed tomography (CT), magnetic resonance imaging (MRI), and ultrasound imaging, are used to study the different biological processes of tumor and provide some basic information regarding tumor location, size, and shape. However, these imaging modalities rarely detect tumors smaller than 0.5 cm, which limits their application in early clinical diagnosis [1]. In recent years, many different types of targeted nanomaterials, such as gold nanostructures [2–5], superparamagnetic nanoparticles [6–8], and ultrasound microbubbles [9, 10], have been developed for structural imaging modalities and help them acquire much higher resolution anatomic images.

Among all the imaging techniques, X-ray computed tomography (CT) is one of the most effective methods for the diagnosis and treatment of diseases in hospitals today for its availability, high efficiency, and low cost [11, 12]. There is no

doubt that CT is among the leading technologies in cancer management. CT is able to provide supplementary anatomical information to assist the diagnosis and treatment of the tumors [2]. Due to the fact that CT relies on the X-ray attenuation by the tissues, electron-dense parts could get better images. Compared to soft tissues, hard tissues have a higher X-ray attenuation. However, the contrast between soft tissues is not obvious due to their similar CT values in the range from 0 through 50 Hounsfield Units (HU) [13]. In terms of the limitations of current contrast agents, CT imaging results are not satisfied. Hence, a major challenge in CT imaging of biological tissues is to achieve a high concentration of contrast agents gathered at the lesion site [14, 15]. Iodine containing molecules as contrast agents are commonly used in conventional CT imaging [14]. Such contrast agents have advantages in absorbing X-ray, but they do not possess the function of specific targeting due to the fact that they cannot conjugate to most biological components or identify cancer markers [3]. It is impossible for iodine containing molecules to accumulate at focus of infection at a concentration high enough to be

detected by current CT scanners. High osmotic pressure and viscosity may cause side effects and renal toxicity; kidney failure has also been reported [16]. Moreover, due to the rapid renal clearance, they allow very short imaging times [17, 18]. Compared to traditional clinical CT equipment of high efficiency for conventional diagnosis in terms of their short response time (e.g., five seconds to capture effective information), micro-CT systems are often quite insensitive (e.g., ten minutes to scan a mouse) [16]. Therefore, X-ray contrast agents also need further development for better use.

It is imperative to develop contrast agents to overcome the shortcomings of current CT imaging. It is well known that CT contrast agents with high atomic number materials could produce better contrast effect than iodine-based contrast agents and have the ability to lower the radiation exposure to patients [19]. It has been reported that compared to iodine, gold has a higher attenuation coefficient and 2.7 times greater contrast effect than iodine at the same X-ray dose [20]. In addition to the advantages above, the applications of gold nanoparticles for cancer diagnosis and CT imaging are superior with the properties of easy modification in the surface to conjugate with specific functional molecules for targeting tumor cells (e.g., antibody and peptides) and the satisfactory biocompatibility [16]. In recent years, nanomaterials have obtained more attention due to its special optical properties and shape. With the change of the shape, gold nanorods (AuNRs) perform tunable optical properties which could be applied on biomedical targeting, photothermal therapy, and *in vivo* imaging [21, 22]. More recently, AuNRs as a potential X-ray contrast agent have been used in computed tomography (CT) imaging [23]. Although the CT contrast effect is not affected substantially by the shape of nanoparticles, gold nanorods have the advantage of being functionally modified. More importantly, the gold nanorods exhibit a better performance in evading clearance by phagocytes to get a longer circulation time than spherical nanoparticles [13]. Currently, iodine-based CT contrast agents imaging have a very short half-life time (<10 min), and there is no specific targeting of the tumor. In the literatures, it has been reported that PEGylated gold nanorods can lead to a prolonged half-life time of 19 h [24]. On the other hand, to increase targeting ability, AuNRs can be functionalized by chemical modification such as DNA, peptides, and antibodies [2, 21, 25]. It is well known that integrin $\alpha_v\beta_3$ plays a decisive role in tumor growth, invasion, and metastasis. Integrin $\alpha_v\beta_3$ has a negligible expression on epithelial cells and mature endothelial cells, but it is highly upregulated on the activated endothelial cells of tumor neovasculature and some tumor cells such as human glioblastoma cell line (U87) [26, 27]. It is noteworthy that peptides (RGD) could target integrin $\alpha_v\beta_3$, which can specifically track several kinds of tumors whereas antibody can only specifically recognize one certain kind of tumor.

Over the past decade, a series of (Arg-Gly-Asp-D-Phe-Lys) (RGD) peptides based probes has been managed in the use of multimodal molecular imaging of integrin $\alpha_v\beta_3$ expression, and the RGD sequence probes with radionuclide have been used in clinical study [27, 28]. Different from the extensive application of radiolabeled RGD peptide for tumor

imaging, the RGD-based nanoprobe with targeting ability are usually rare [28].

In this paper, we obtained RGD-AuNRs nanoprobe with an ability of targeting tumor cells by modification with a bifunctional PEG and conjugation with RGD peptide. By cell viability assay and dark-field imaging, we verified the biocompatibility of RGD-AuNRs which facilitated the subsequent *in vivo* experiments. First, the comparison of micro-CT imaging between AuNRs and iohexol showed the advantage of AuNRs in terms of CT contrast effect. Second, to verify the feasibility of RGD-AuNRs for CT imaging *in vivo*, *in vivo* micro-CT imaging of intramuscular and subcutaneous injection of RGD-AuNRs was managed. Last, RGD-AuNRs were tail vein injected into U87 tumor model (with integrin $\alpha_v\beta_3$ -positive tumor cells) and HT-29 tumor model (with integrin $\alpha_v\beta_3$ -negative tumor cells). Then, micro-CT imaging of two tumor models were performed to detect the targeting ability of RGD-AuNRs and the imaging effect of the tumor site.

2. Materials and Methods

2.1. Materials and Reagents. Hydrogen tetrachloroaurate (III) trihydrate ($\text{HAuCl}_4 \cdot 3\text{H}_2\text{O}$), cetyl trimethyl ammonium bromide (CTAB), poly(ethylene glycol) 2-mercaptoethyl ether acetic acid (HS-PEG-COOH), Thiazolyl Blue Tetrazolium Bromide (MTT), and Dimethyl Sulfoxide (DMSO) hybridmax were purchased from Sigma-Aldrich (St. Louis, USA). Sodium borohydride (NaBH_4) was purchased from Kermel Chemical Reagent Co. Ltd. (Tianjin, China). L-ascorbic acid (AA) was obtained from Tianli Chemical Reagent (Tianjin, China). Silver nitrate (AgNO_3) was obtained from Shanghai Chemical Reagent Co. Ltd. (Shanghai, China). 1-Ethyl-3-(3-dimethylaminopropyl)carbodiimide (EDC) and N-hydroxysulfosuccinimide (Sulfo-NHS) were purchased from Aladdin (Shanghai, China). Cyclo (Arg-Gly-Asp-D-Phe-Lys) (RGD) was prepared by GL Biochem Co. Ltd. (Shanghai, China). All the above chemicals were used without any further purification. Deionized water (Millipore Milli-Q grade) with a resistivity of $18.2 \text{ M}\Omega \text{ cm}^{-1}$ was used in all the preparations.

2.2. Preparation of AuNRs. AuNRs was prepared based on the seed-mediated growth method of Nikoobakht and El-Sayed [29]. Seed solution was needed to prepare AuNRs. 5 mL of HAuCl_4 (0.5 mM) was added into 5 mL of CTAB solution (0.2 M). Then, 0.6 mL of NaBH_4 (0.01 M) at 0°C was added. The seed solution was vigorously stirred for 2 min and kept at 25°C . Then, we prepared growth solution. 0.25 mL of AgNO_3 solution (0.004 M) was mixed with 5 mL of CTAB solution (0.2 M) at 25°C . 5 mL of HAuCl_4 (1 mM) was added into the mixture, and then 70 μL of ascorbic acid (0.0788 M) was added which changed the color of solution from yellow to colorless. Finally, 12 μL of the seed solution was injected into the growth solution, then standing for 3 h at 27.5°C . The product was kept at 4°C for further use.

2.3. PEGylation and RGD Conjugation. In order to prepare RGD-conjugated AuNRs, CTAB on the surface of the gold nanorods needed to be replaced with bifunctional PEG

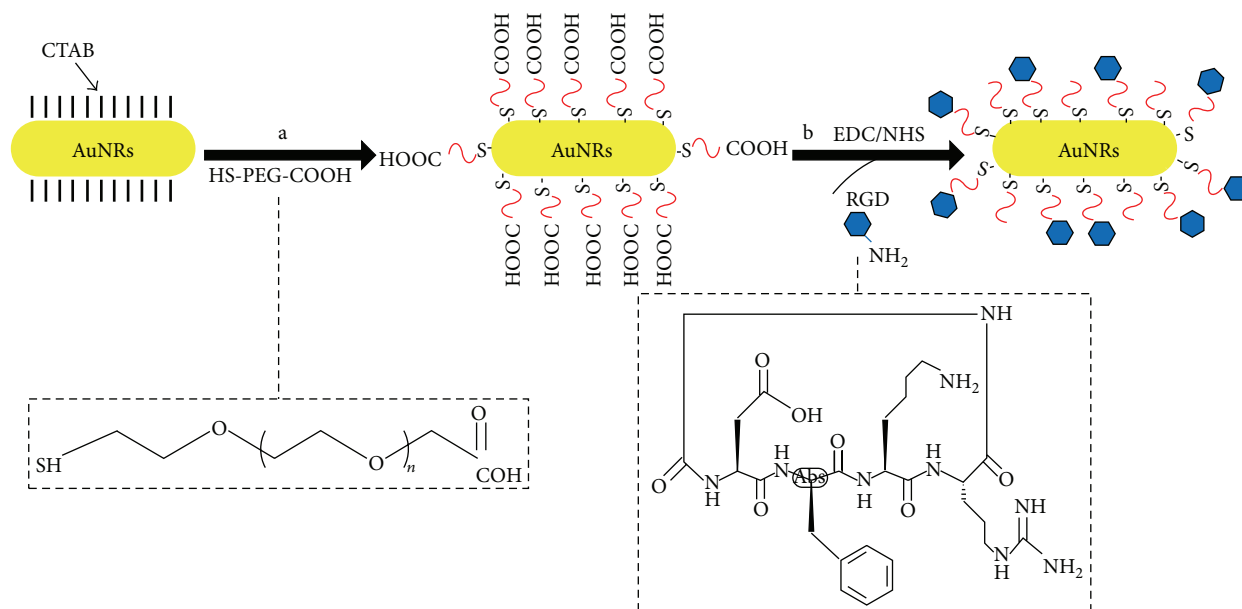


FIGURE 1: Schematic illustration of the synthesis of RGD-conjugated PEGylated AuNRs. a: CTAB was substituted for a bifunctional PEG. b: RGD was conjugated to PEG-AuNRs.

[30]. Figure 1 shows the synthetic pathway for preparing RGD-conjugated PEGylated AuNRs. (i) 30 mg of HS-PEG-COOH (MW = 5 k) was added into 2 mL of gold nanorods solution ($C_{\text{Au}} = 300 \mu\text{g/mL}$) and then stirred for 24 h at 25°C. To remove unreacted PEG, the mixture was centrifuged at 11,000 rpm for 10 min and then was resuspended in 2 mL of phosphate buffered saline (PBS) (pH = 7.4). (ii) 16.91 mg of EDC (1-ethyl-3-(3-dimethylaminopropyl)carbodiimide) and 10.15 mg of Sulfo-NHS (N-hydroxysulfosuccinimide) were added into the mixture for 30 min to activate the carboxyl groups on the surface of AuNRs and stabilize the activated groups of carboxyl. The mixture was centrifuged at 11,000 rpm for 10 min to remove the excess EDC and Sulfo-NHS and resuspended in 2 mL of PBS. (iii) The final step was to conjugate RGD (MW = 5 k). 500 μL of RGD (1.656 $\mu\text{mol/mL}$) was added to 2 mL of PEGylation-AuNRs (PEG-AuNRs) solution and reacted at 4°C for 6 h. After the reaction, excess RGD was removed by centrifugation at 11,000 rpm for 10 min and resuspended in 1 mL of PBS.

2.4. Characterization of Gold Nanomaterials. To characterize the gold nanomaterials, zeta potentials were measured with a Zetasizer Nano ZS in water (Malvern Zen 3690, United Kingdom) and UV-Vis spectrums were measured at 25°C by the SHMADZU UV-2450 UV-visible spectrophotometer with 1 cm quartz cell. Transmission electron microscope measurements were performed by H-600 (Hitachi, Japan) operated at 75 kV accelerating voltage.

2.5. Cell Culture. Human glioblastoma cell line (U87) (integrin $\alpha_v\beta_3$ -positive tumor cells) and human colon malignant tumor cell line (HT-29) (integrin $\alpha_v\beta_3$ -negative tumor cells) were cultured in 90% Dulbecco's Modified Eagle's Medium (DMEM) of high glucose culture medium (Hyclone,

Thermo Scientific, US) with the addition of 10% fetal bovine serum (Hyclone, Thermo Scientific, US) and 1% antibiotics (Hyclone, Thermo Scientific, US). Temperature and carbon dioxide content were maintained at 37°C, 5%.

2.6. MTT Assay. To certify the biocompatibility of gold nanomaterials, cell viability assays were managed. The U87 and HT-29 cells were inoculated into 96-well plates (5,000 cells per well), respectively, and incubated for 24 h. The sterile AuNRs and RGD-AuNRs were added to 96-well plates (200 μL per well) at different concentrations (100, 10, 1, 0.1, 0.01, and 0.001 nmol/mL, Au). Then, The U87 and HT-29 cells were incubated for another 72 h. After incubation, the cells were exhaustively washed with sterile PBS to remove residual gold nanomaterials. 20 μL MTT (5 mg/mL) was added to each well subsequently and incubated for 4 h. 150 μL DMSO was added to each well to dissolve the formazan crystals and then the medium was shocked for 15 min. Reading was taken in Spectramax 190 (Molecular Devices, China) at 490 nm.

2.7. Dark-Field Imaging. To evaluate integrin $\alpha_v\beta_3$ binding affinities and uptake abilities of gold nanomaterials with tumor cells, the U87 and HT-29 cells were chosen and incubated for 3 days. After trypsinized, the cells were centrifuged at 800 rpm for 5 min. The supernatant was discarded, and the solid was suspended in 2 mL culture medium which was then distributed into two sterile tubes homogeneously. 200 μL of PEG-AuNRs and RGD-AuNRs ($C_{\text{Au}} = 600 \mu\text{g/mL}$) were added to U87 cells, respectively, with HT-29 cells being the same case. Then, U87 and HT-29 cells were incubated in cell incubator for 30 min at 37°C. The cells were rinsed with PBS twice and then resuspended in 200 μL PBS to remove unbound nanomaterials. Glass slides were prepared and

fastened with clean-mounts. An Olympus IX70 microscope at 40x magnification was used to perform dark-field imaging.

2.8. Micro-CT Imaging of Gold Nanomaterials

2.8.1. Micro-CT Imaging of AuNRs. Different concentrations of AuNRs ($C_{Au} = 1, 5$ and 10 mg/mL), iohexol (10 mg/mL), and deionized water were prepared in 200 μ L tubes. Tubes were divided into three groups, including experiment group (AuNRs), control group (iohexol), and blank (deionized water), and then scanned by a micro-CT imaging system which consisted of a microfocus X-ray source (Apogee, Oxford Instruments) and an X-ray flat panel detector (C7921CA-02, Hamamatsu, Japan), with the following operating parameters of 50 kV, 1 mA with a 512×512 matrix size, and 360 views.

2.8.2. Feasibility Verification of In Vivo Micro-CT Imaging of RGD-AuNRs. Female mice weighing about 27 g were purchased from the Department of Experimental Animal of Xi'an Jiaotong University. The animals were treated in accordance with institutional animal use and care regulations. After the mouse was anesthetized (with 0.1 mL 10% chloral hydrate and 1% atropine), 100 μ L of RGD-AuNRs in PBS was intramuscularly injected into the right hind leg area ($C_{Au} = 10$ mg/mL) and subcutaneously injected into the back of mouse ($C_{Au} = 5$ mg/mL), respectively. The mouse was fixed on a homemade holder using the above micro-CT imaging system with parameter setting unchanged. As a control contrast, the mouse was scanned before RGD-AuNRs injection. And 10 days after injection, no proof of toxicity was observed.

2.8.3. In Vivo Micro-CT Imaging of RGD-AuNRs Targeting Tumor Mouse. Two nude mice were injected with cancer cells (2×10^6) into the right arm and divided into two groups including positive group (U87 cells) and negative group (HT-29 cells), until the tumor reached a diameter of over 0.5 cm. 100 μ L PBS solution of RGD-AuNRs ($C_{Au} = 3$ mg/mL) was tail vein injected into the two nude mice, respectively. The first scanning was carried out before (0 h) tail vein injection by NanoScan PET/CT (Mediso, Medical Imaging Systems, USA) with operating parameters of 55 kV and 146 μ A to determine the CT datum line. CT scanning was performed after tail vein injection of RGD-AuNRs at time points of 1 and 3 h. All CT scans were performed under gases of isoflurane anesthesia. The contrast effect was quantitatively determined by the differential contrast in CT values (in HU).

3. Results

3.1. Characterization of the Nanoparticles. The characteristics of the gold nanomaterials are shown in Figure 2. And the UV-visible absorption spectrums of gold nanomaterials are presented in Figure 2(a). Compared to the spectrum of AuNRs, there was a minimal redshift in the longitudinal peak when conjugated with RGD, similar to PEGylation-AuNRs (PEG-AuNRs). The absorption spectrums demonstrated that the AuNRs, even after modification with HS-PEG-COOH and RGD, were able to maintain their morphology and optical

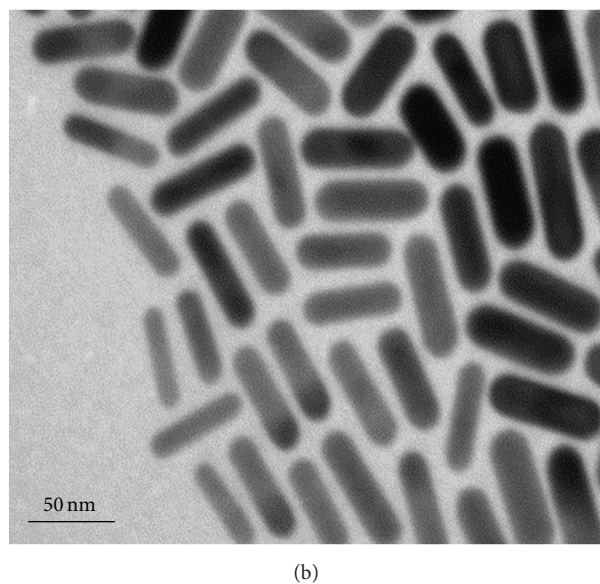
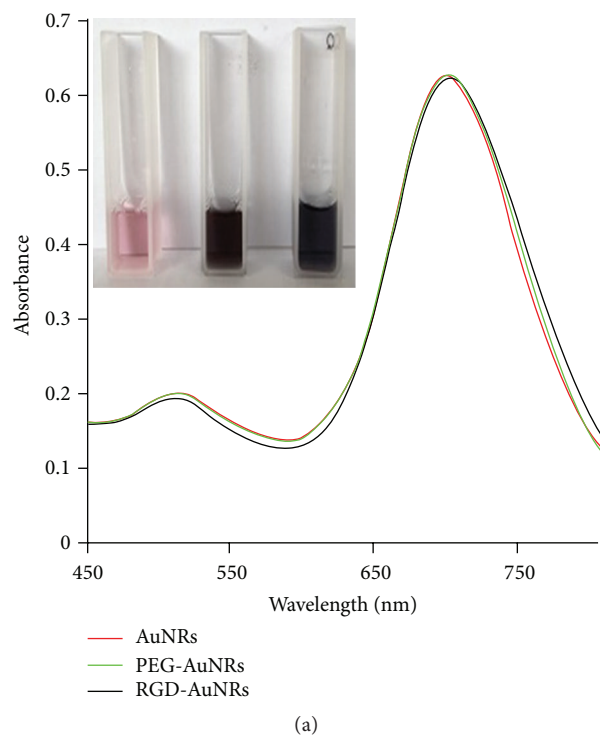


FIGURE 2: (a) UV-Vis spectrums of the AuNRs, PEG-AuNRs, and RGD-AuNRs (inset, the color changes from left to right are AuNRs, PEG-AuNRs, and RGD-AuNRs). (b) TEM image of AuNRs with plasmon band energies at 700 nm, and the scale bar is 50 nm.

properties in the NIR region. The structure and size of AuNRs were evaluated by TEM, as shown in Figure 2(b). The AuNRs had a good rod shape with a smooth surface, with aspect ratio (AR) of 2.5 . At each step, surface potentials of AuNRs which changed with surface ligands changing are shown in Table 1. As declared in Figure 1, the AuNRs were first stabilized by HS-PEG-COOH and then by RGD in a sequential manner. The surface of the synthesized AuNRs

TABLE I: Zeta potentials of gold nanomaterials.

Gold nanomaterials	Zeta potential	
	Mean (mV)	Standard deviation
AuNRs	40	± 5
PEG-AuNRs	-25	± 2
RGD-AuNRs	-17	± 2

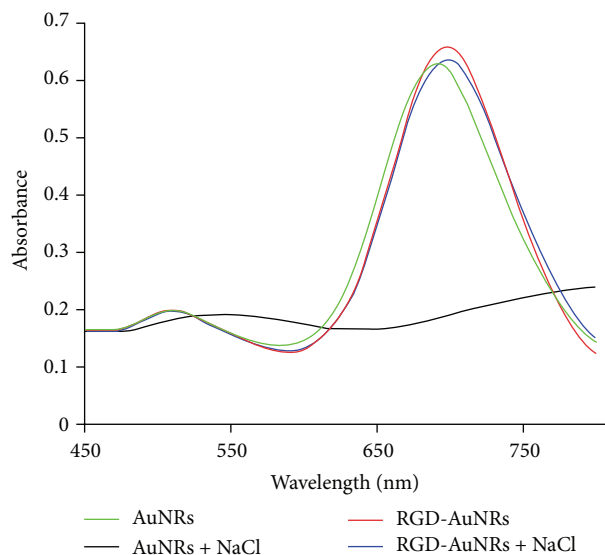


FIGURE 3: UV-Vis spectrums of AuNRs and RGD-AuNRs with different dispersants (deionized water and 10% NaCl solution) at 4°C.

was wrapped in CTAB with a positive surface charge of 40 mV. The HS-PEG-COOH substituting step decreased the surface potential to about -25 mV, whereas RGD conjugation increased the zeta potential roughly to a degree of -17 mV. The potential variation suggested that RGD was successfully conjugated with PEG-AuNRs.

3.2. Stability of RGD-AuNRs. The test of stability of RGD-AuNRs was very important for their applications *in vivo*. Gormley et al. [31] investigated that the aggregation extent of RGD-AuNRs could be reported by the different absorption properties in the UV-Vis spectrum. So the stability of RGD-AuNRs was analyzed via UV-Vis spectrometry (Figure 3). It could be seen that in the deionized water the spectrums of RGD-AuNRs and AuNRs did not show major changes. However, it was a different case when they were dispersed into 10% NaCl. RGD-AuNRs dispersed into 10% NaCl had a similar spectrum as deionized water. But the spectrum of AuNRs dispersed into 10% NaCl changed obviously, which suggested that AuNRs had aggregated and were unstable. The results indicated that RGD-conjugated AuNRs significantly improved the stability of the particles.

3.3. The Effects of RGD-AuNRs on Cytotoxicity In Vitro. After studying the RGD-AuNRs characteristics, we examined

the extent of cytotoxicity to tumor cells. During the AuNRs preparation process, the surface stabilizer CTAB has a strong cytotoxicity, so it was necessary to analyze the cytotoxicity of RGD-AuNRs. The MTT assay results of U87 and HT-29 cells, which are showed by open bars in Figure 4, both indicated that when the concentration of AuNRs (here, we actually referred to the concentration of Au) was higher than 0.1 nM, there was a high cytotoxicity (lower than 80% viability). When the concentration was greater than 1 nM, the cell viability decreased apparently. On the other hand, due to the conjugation of RGD, no significant effects on the cell viability (higher than 80% viability) were seen even at a high concentration of 10 nM, as shown by closed bars in Figure 4. The data indicated that RGD conjugation significantly improved the biocompatibility of AuNRs for biomedical applications, especially when the concentration of particles required was high. RGD-AuNRs possessed a property of noncytotoxicity in the given concentration range and should be suitable for CT imaging applications *in vivo*.

3.4. The Ability of RGD-AuNRs Binding Tumor Cells. The ability of RGD-AuNRs to binding with tumor cells was evaluated by dark-field imaging, as shown in Figure 5. In terms of some tumor cells that had an expression of integrin $\alpha_v\beta_3$ to varying degrees, our tests used human glioblastoma line, U87 (10^4 cells/mL, Figures 5(a), 5(c), and 5(e)), as a positive group and human colon cancer cell line, HT-29 (10^4 cells/mL, Figures 5(b), 5(d), and 5(f)), as a negative group for comparison purpose. 150 μ L of PEG-AuNRs and RGD-AuNRs ($C_{Au} = 0.4$ nM) were added to each group, respectively. Experimental results showed that integrin $\alpha_v\beta_3$ had a high expression in the positive group. And peptides RGD on the surface of AuNRs had a strong ability to identify U87 tumor cells, as shown in Figure 5(c). Especially in the amplified image, after incubation with RGD-AuNRs, U87 cells displayed an apparently golden color around the cells, indicating aggregation of gold nanomaterials in the cells (Figure 5(e)). However, in the negative group, HT-29 cells with a low expression of integrin $\alpha_v\beta_3$ led to a poor binding ability of RGD, as shown in Figures 5(d) and 5(f). Meanwhile, PEG-AuNRs could not effectively recognize tumor cells, so the cells in the two experiments did not show obvious binding in dark-field imaging (Figures 5(a) and 5(b)). Finally, the binding ability of the RGD peptide was directly related to the expression ability of integrin $\alpha_v\beta_3$. With the higher expression of integrin $\alpha_v\beta_3$ on the tumor cells, it was easier for RGD-AuNRs to recognize tumor cells which provided us with excellent supporting for *in vivo* tumor targeting micro-CT imaging.

3.5. Micro-CT Imaging of Gold Nanoparticles

3.5.1. Micro-CT Imaging of AuNRs. AuNRs have a strong X-ray attenuation, which are promising nanomaterials as contrast agents for CT imaging. In our study, the Hounsfield Units (HU) of AuNRs, iohexol, and deionized water were measured by micro-CT imaging system. Figure 6 shows the CT images and the attenuation values (in HU) of each

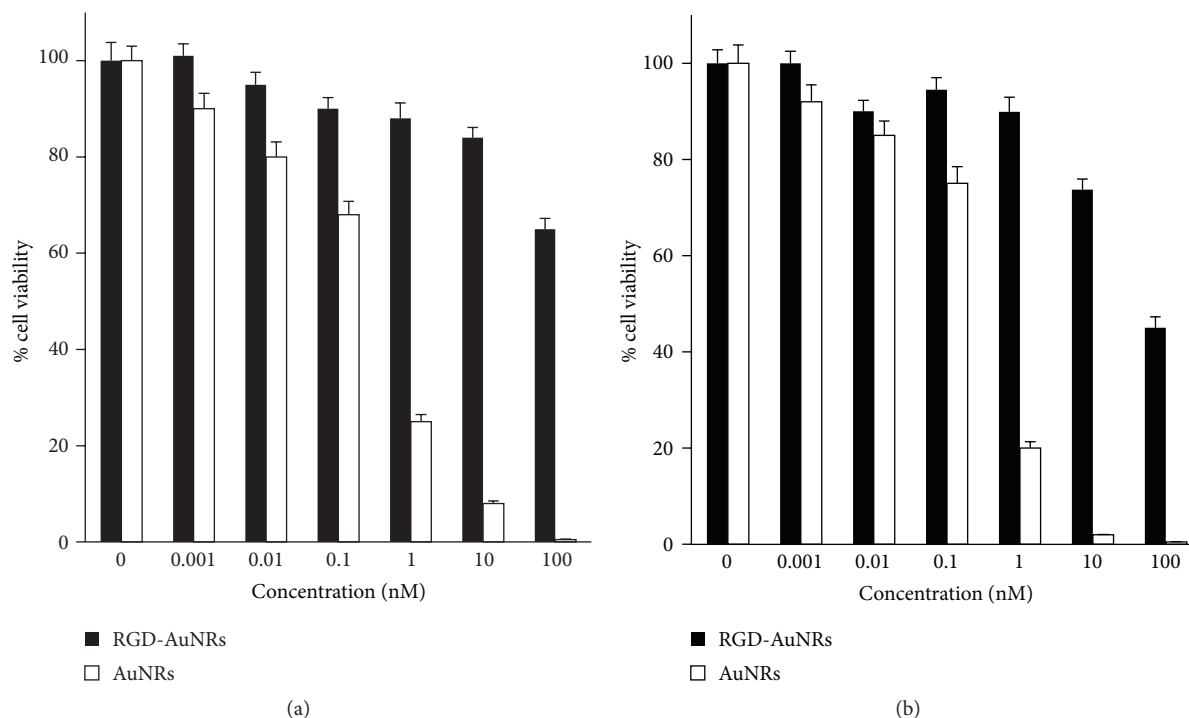


FIGURE 4: Viabilities of U87 cells (a) and HT-29 cells (b) after incubation with RGD-AuNRs (closed bars) and AuNRs (open bars). All data are averages for $n = 3$. The error bars represent one standard deviation.

sample. The higher the concentration of AuNRs was, the brighter the images were, which indicated an increased X-ray attenuation. HU quantitatively showed the proportional relationship between the concentration of AuNRs and CT signal intensity. When the concentration of iohexol and AuNRs kept the same level, a higher HU value of AuNRs was shown, which indicated that at the same X-ray dose, AuNRs would be more ideal as CT imaging contrast agents.

3.5.2. Feasibility Verification of In Vivo Micro-CT Imaging of RGD-AuNRs. To verify the feasibility of RGD-AuNRs for CT imaging *in vivo*, 100 μL RGD-AuNRs in PBS was intramuscularly injected into the right hind leg area ($C_{\text{Au}} = 10 \text{ mg/mL}$) and subcutaneously injected into the back of mouse ($C_{\text{Au}} = 5 \text{ mg/mL}$), respectively. And then the mouse was placed on a homemade holder after anesthesia and scanned by micro-CT imaging system. As shown in Figure 7, compared with other soft tissues, the back and leg area with injection had a contrast enhancement, which was attributed to the strong X-ray attenuation of AuNRs. Before and after injection, the CT values of the injection sites were illustrated in Figure 8. The corresponding injection sites of the mouse showed a clearly distinguished CT signal intensity and a significant change in brightness which indicated a direct evidence of the imaging effect of RGD-AuNRs as contrast agents for CT imaging. And with a higher concentration of RGD-AuNRs, the brightness of the injection site was higher. CT values (in HU) changed obviously from 11 to 100 (back) (Figures 8(a) and 8(c)) and 9 to 186 (right hind leg) (Figures 8(b) and 8(d)). Up to 10

days after injection, the mouse's behavior was normal which indicated that RGD-AuNRs were harmless to mouse.

3.5.3. In Vivo Micro-CT Imaging of RGD-AuNRs Targeting Tumor Mouse. Human glioblastoma cells (U87) as a positive group and human colon cancer cells (HT-29) as a negative group were inoculated in nude mice. In our study, CT imaging was used to detect the ability of RGD-AuNRs to target tumor cells and tumor neovasculature during the whole blood circulation. Figure 9 displayed micro-CT images before and after (1 and 3 h) intravenous injection of RGD-AuNRs in nude mice. 1 h after injection, tumor uptake of RGD-AuNRs was lower in HT-29 colon malignant tumor compared with U87 glioblastoma tumor, shown in Figures 9(c) and 9(g). After injection of RGD-AuNRs 3 h, there was a difference in brightness of images between positive group and negative group and the tumor site displayed an obvious contrast to be visualized compared with other soft tissues in positive group (Figures 9(d) and 9(h)). This result also showed U87 glioblastoma tumor had a higher expression of integrin $\alpha_v\beta_3$ than HT-29 colon malignant tumor. However, the contrast effects were still not as obvious as that in intramuscular and subcutaneous injection experiments (Figures 7 and 8). As shown in Figures 9(b)–9(d), with blood circulation, RGD-AuNRs gradually targeted the tumor tissue during 0–3 h, which was proved by the growing brightness of images. These results directly certified the practicality of U87 cells with high expression of integrin $\alpha_v\beta_3$ targeted by RGD-AuNRs with a high specificity. Meanwhile, AuNRs could be used as

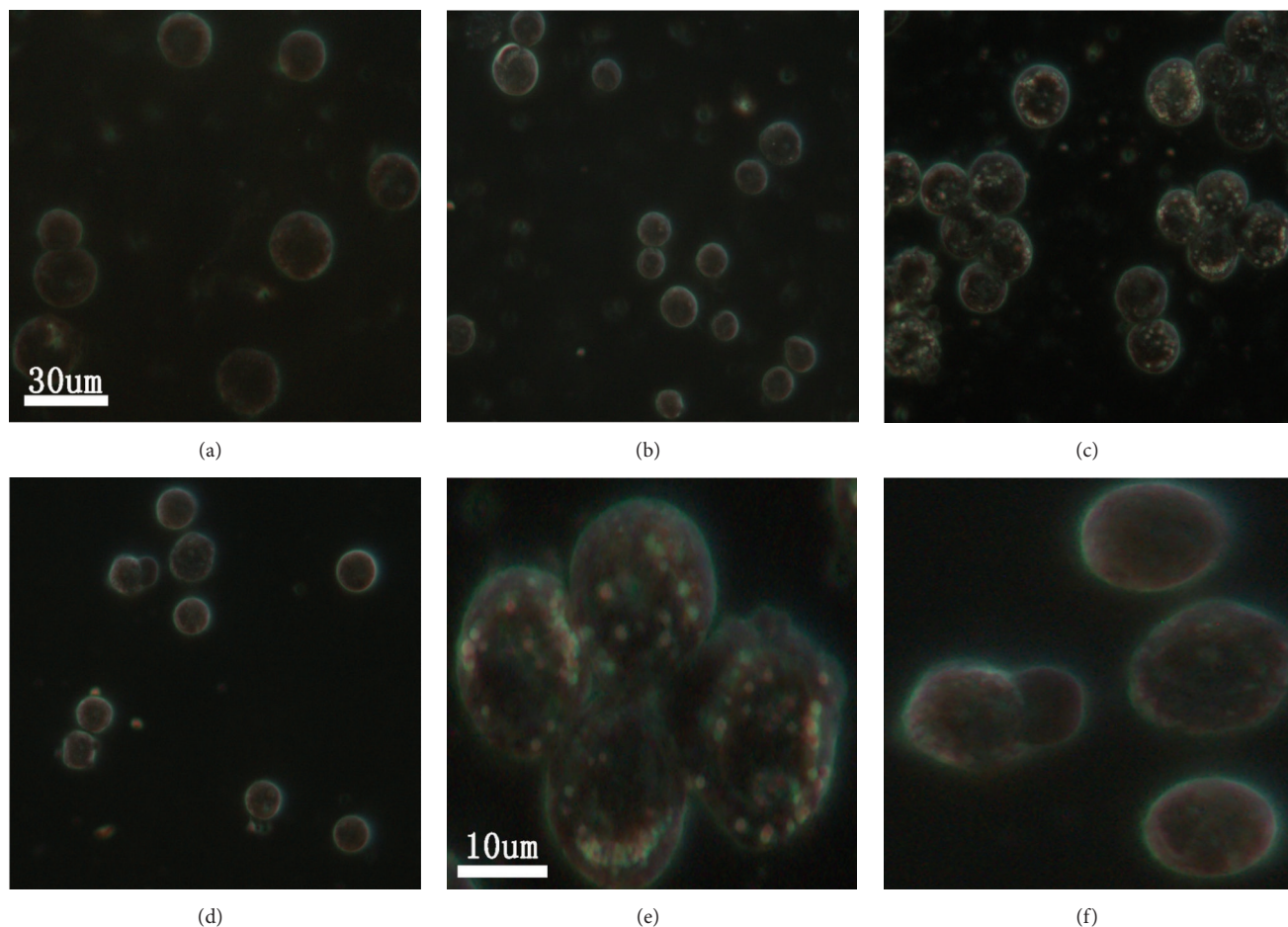


FIGURE 5: Dark-field imaging of U87 cells and HT-29 cells. (a) PEG-AuNRs with U87 cells. (b) PEG-AuNRs with HT-29 cells. (c) RGD-AuNRs with U87 cells. (d) RGD-AuNRs with HT-29 cells. (e) The corresponding amplified image of U87 cells in (c). (f) The corresponding amplified image of HT-29 cells in (d). Integrin $\alpha_v\beta_3$ expression in U87 cells is positive, so the brightness of the RGD-AuNRs targeting U87 cells in the dark-field imaging is highest. The scale bar of (a–d) is 30 μm with (e–f) 10 μm .

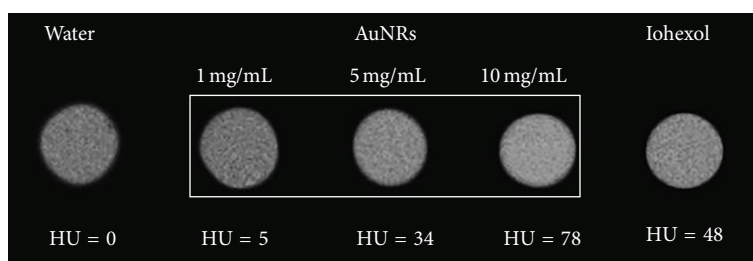


FIGURE 6: Tubes CT images of water, AuNRs, and iohexol. The concentration (mg/mL) of major elements (Au and I) in each tube is provided at the top of the image. The CT attenuation (in HU) in each tube is provided at the bottom of the image.

a potential contrast agent at the U87 tumor site to enhance X-ray signal for CT imaging.

4. Discussion

X-ray computed tomography has advantages of high spatial resolution, wide range of applications, easy operation, low cost, and so forth. So far CT imaging is still the most basic and

primary tumor pathological examination method, and even the preferred screening method for tumors on some parts of the bone tissues. Since the 1970s, iodine containing molecules as CT imaging contrast agents have been widely applied on CT imaging. But with the development of clinical medicine, iodine containing molecules as CT imaging contrast agents in imaging depth, imaging time, and specificity of imaging have been unable to satisfy existing imaging requirements. Since

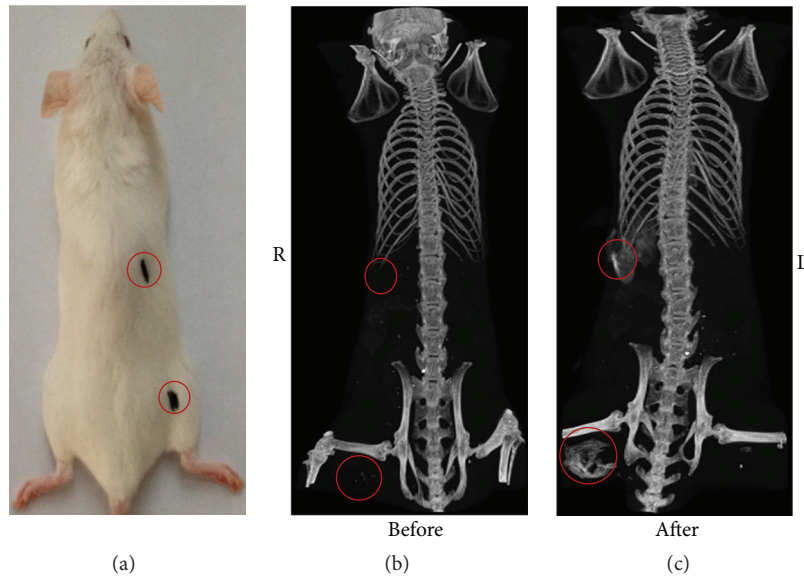


FIGURE 7: *In vivo* CT imaging of mouse before and after intramuscular and subcutaneous injection with different concentration of RGD-AuNRs at different sites. (a) The photograph of mouse. (b) CT image before injection. (c) CT image after injection.

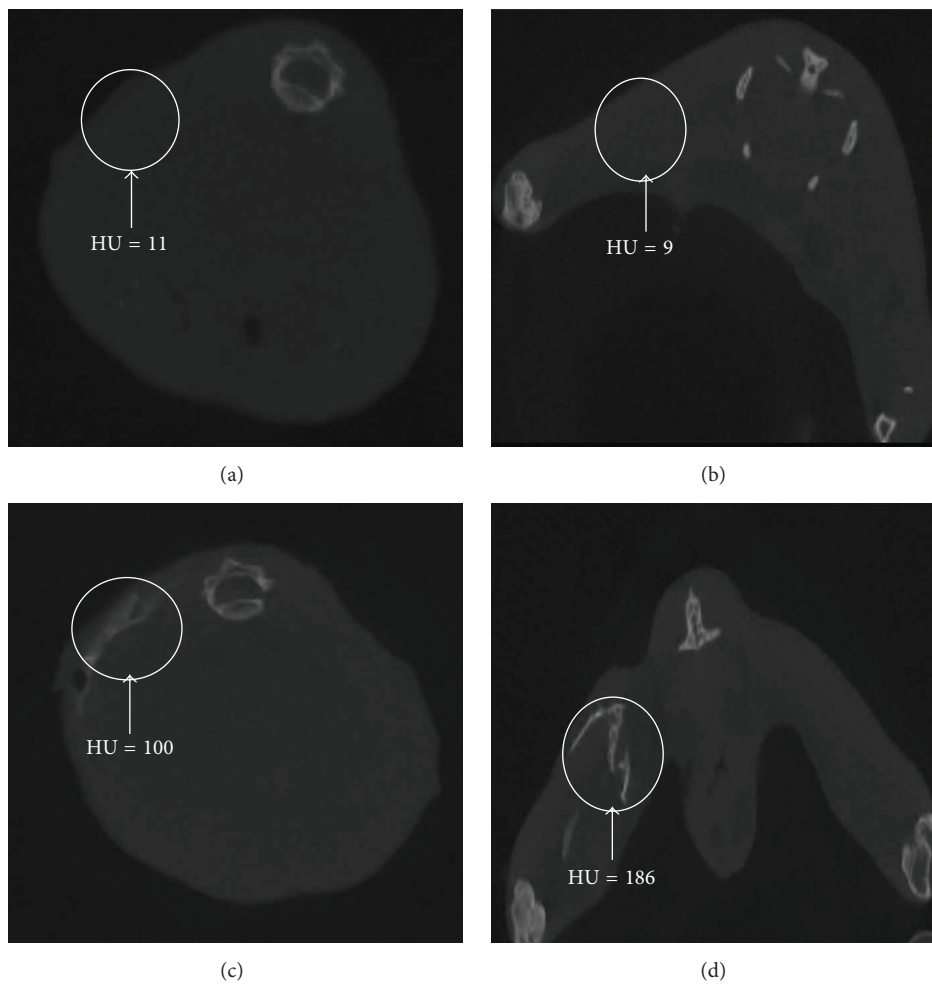


FIGURE 8: CT slices of mouse before and after injection with RGD-AuNRs. (a, c) The transverse slice images of the back area, the HU values of the injection site changed from 11 to 100. (b, d) The transverse slice images of the right hind leg, the HU values of the injection site changed from 9 to 186.

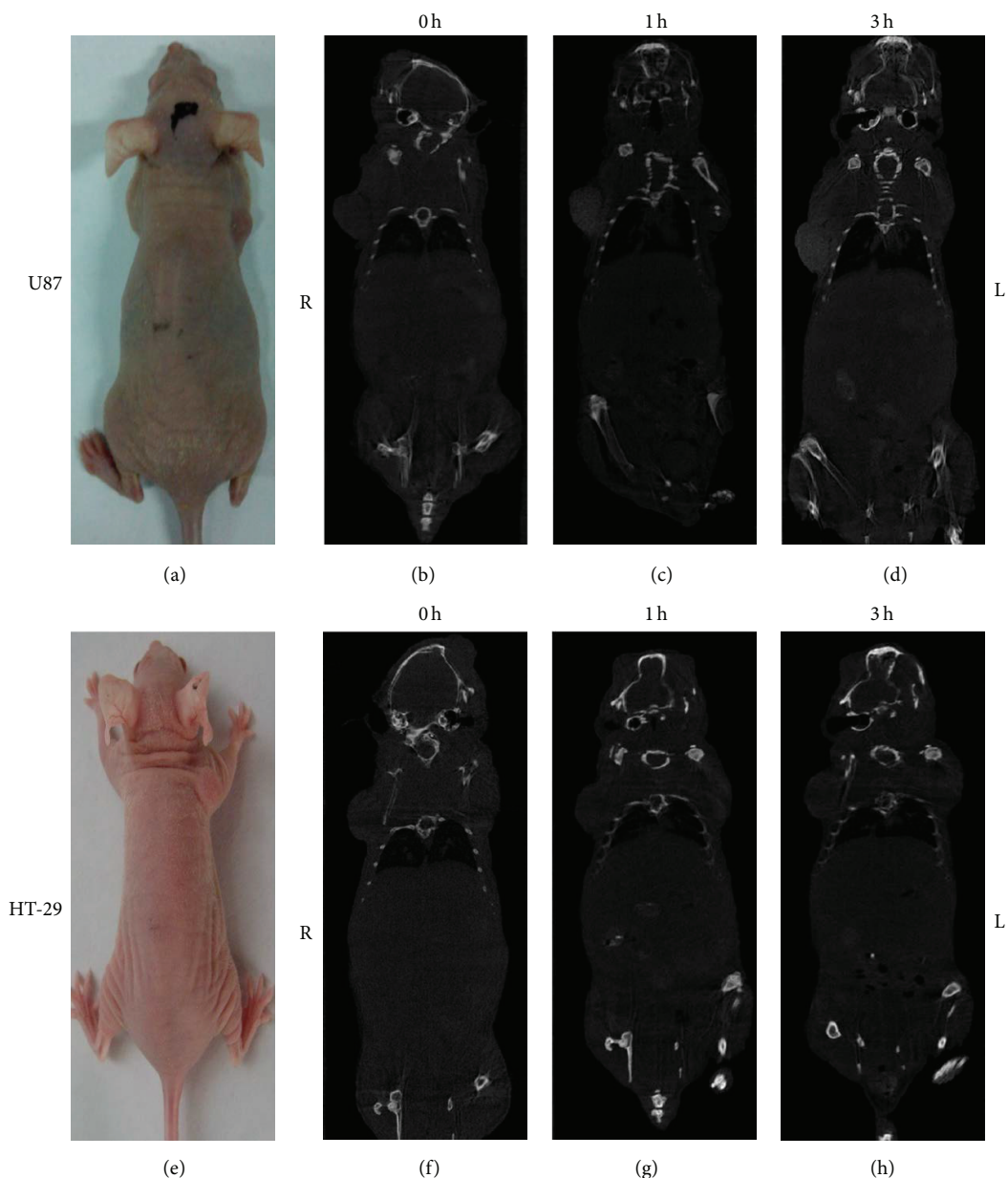


FIGURE 9: *In vivo* tumor targeting CT images of mice after intravenous injection with RGD-AuNRs at different time points. (a–d) The CT images of positive group. (e–h) The CT images of negative group. (a, e) The photographs of mice. (b, f) The CT images at 0 h. (c, g) The CT images at 1 h. (d, h) The CT images at 3 h.

2004, Hainfeld et al. [32] investigated the high atomic weight of gold in the field of X-ray imaging; most of the examination on inorganic nanoparticles-based X-ray contrasting agents is focused on gold nanoparticles or their hybrids. With lower X-ray dosage, gold has a better X-ray attenuation than iodine. Besides the characteristic that gold nanomaterials display a strong X-ray attenuation, researches have also focused on their use for X-ray CT and multimodal imaging in terms of the substantial control of their physical, chemical, and biological properties [33]. As emphasized above, the applications of gold nanomaterials for CT imaging and cancer diagnosis are superior with the properties of easy self-assembly with

specific functional molecules or targeting agents for targeting tumor cells (e.g., antibody, aptamers, and peptides), prolonged circulation time, enhanced renal clearance, noticeable optical properties that could be varied depending on their particle size and shape, and the satisfactory biocompatibility [20, 27, 29]. With the change of the shape, gold nanorods (AuNRs) perform tunable optical properties which could be applied on biomedical targeting, photothermal therapy, and *in vivo* imaging [30, 31]. More recently, AuNRs as a potential X-ray contrast agent have been used in CT imaging [34]. In the literatures, it has been reported that PEGylated gold nanorods can lead to a prolonged half-life time of 19 h [35].

Kim et al. [36] and Cai et al. [37] exploited *in vivo* applications of AuNPs as X-ray contrast agents with micro-CT. They managed PEGylated AuNPs as blood pool contrasting agents to provide apparent vascular contrast enhancement effect with plasma half-time around 12 h and 14.6 h, respectively. On the other hand, to enhance the targeting ability, AuNRs can be functionalized by chemical modification such as DNA, peptides, and antibodies.

In this study, we have prepared a new RGD-AuNRs probe for integrin $\alpha_v\beta_3$ targeting and tumor imaging. By PEG modification and small molecule peptides RGD conjugation, unspecific binding ability of AuNRs could be dramatically decreased while targeting ability was increased obviously which can benefit the accumulation of AuNRs in tumor tissues and prolonged the residence time in the biological tissues. Also the MTT assay and stability measurement showed that RGD conjugation eliminated their cytotoxicity and improved their biocompatibility and stability. RGD conjugation increased the *in vitro* integrin $\alpha_v\beta_3$ binding affinity by the contrast between RGD-AuNRs and PEG-AuNRs. The feasibility of RGD-AuNRs for the noninvasive detection of integrin $\alpha_v\beta_3$ expression was assessed in both U87 and HT-29 tumor models. And the tumor uptake of AuNRs-RGD was also significantly higher in integrin $\alpha_v\beta_3$ -positive U87 tumor model than in integrin $\alpha_v\beta_3$ -negative HT-29 tumor model.

Since AuNRs stabilized with CTAB show strong cytotoxicity, the management that barely depending on centrifugation will lead to aggregation of AuNRs. Several methods to eliminate the toxicity of AuNRs and stabilize them in physiological environment have been researched. Jain et al. [38] confirmed photothermal therapy and NIR cell imaging by anti-EGFR antibody-conjugated AuNRs which could bound to malignant cancer cells expressing EGFR as light scattering and photothermal therapy agents *in vitro*. There exist several other methods that have been reported to displace CTAB to modify the surface chemistry and decrease the cytotoxicity of AuNRs, including polyelectrolyte wrapping [39], substitution by a thiol-terminal PEG [25], and alternative by alkanethiols [40] and lipids [41]. Niidome et al. [35] demonstrated the feasibility to reduce the toxicity by PEG modification. In their study, they testified the cell viability of two kinds of AuNRs (stabilized by CTAB and modified with PEG). The results also verified the fact that PEG modification is an effective strategy for preparing biocompatible materials. Here, we managed to replace CTAB with PEG for biological applications. PEG modification was achieved by adding PEG in the AuNRs solution; then, excess PEG was removed by centrifugation. PEG-modified gold nanoparticles showed a nearly neutral surface and had little cytotoxicity *in vitro*. In our studies, the results suggested that the substitution of CTAB by polyethylene glycol eliminated the cytotoxicity of AuNRs to a large extent (Figure 4). It is well known that integrin $\alpha_v\beta_3$ plays a decisive role in tumor growth, invasion, and metastasis. Gladson [42] and Bello et al. [43] proved the fact that integrin $\alpha_v\beta_3$ expression occurs in glioma endothelial cells using relatively small numbers of tumor frozen sections. Integrin $\alpha_v\beta_3$ has a negligible expression on epithelial cells and mature endothelial cells, but it is highly upregulated on the activated endothelial cells of tumor neovasculature and some tumor

cells such as human glioblastoma cell line [44, 45]. It is noteworthy that peptides (RGD) could target integrin $\alpha_v\beta_3$, which can specifically track several kinds of tumors, whereas antibody can only specifically recognize one certain kind of tumor. Haubner et al. [46] studied for the first time the corresponding relationship between the tumor uptake ability of RGD probe and the integrin $\alpha_v\beta_3$ expression level. And U87 cells were chosen as the integrin $\alpha_v\beta_3$ -positive cells and HT-29 cells were chosen as the integrin $\alpha_v\beta_3$ -negative cells.

In vitro integrin $\alpha_v\beta_3$ receptor binding ability of RGD-AuNRs was analyzed by dark-field imaging experiments. The uptake efficiency of AuNRs-RGD by U87 cells was much higher than HT-29 cells. For U87 cells (positive group) that had a higher expression of integrin $\alpha_v\beta_3$ than HT-29 cells (negative group), the specific binding of RGD-AuNRs with U87 cells was more obvious (Figure 5). The RGD-AuNRs were tail vein injected into two nude mice tumor models of U87 (integrin $\alpha_v\beta_3$ -positive tumor) and HT-29 (integrin $\alpha_v\beta_3$ -negative tumor) for CT imaging. RGD-AuNRs were capable of specifically recognizing tumor cells and tumor neovasculature with a high expression of integrin $\alpha_v\beta_3$. The accumulation of RGD-AuNRs at the U87 tumor site was more significant than the HT-29 tumor site. The CT images of the tumor site with a higher contrast than other soft tissues due to the high X-ray attenuation of RGD-AuNRs specifically in the U87 tumor model (Figure 9). Because of the systemic circulation and metabolism *in vivo* and the character of nanomaterials themselves, some AuNRs intravenously injected could not finally arrive at the tumor site. So compared to the CT imaging of subcutaneous and intramuscular injection of RGD-AuNRs into the mouse (Figures 7 and 8), the results were less obvious. Some methods may be effective in making the imaging more clear and increasing the contrast effects. Adding large gold doses is an optional method [47]; thus, amounts suitable for accurate quantification can be used to provide noise-free images clearly. Another factor is the micro-CT unit. By tweaking these preferences, favorable contrast from gold can also be produced owing to its significantly greater attenuation coefficient than soft tissue [47]. Dou et al. demonstrated that the optimal sizes of spherical AuNPs for simultaneous CT imaging and radiosensitization could be selected and evaluated based on the distinctive size-dependent enhancement effects [48]. Regulating the aspect ratio and the size of the RGD-AuNRs that we synthesized may achieve the same goal. The contrast effects of subcutaneous and intramuscular injection of RGD-AuNRs into the mouse were bright enough to verify the feasibility of gold nanomaterials *in vivo* imaging. This may due to the resistance in other organs during the blood circulation. Niidome et al. [35] verified the biodistribution of surface modified AuNRs after intravenous injection by ICP mass spectrometry at different time points. AuNRs may accumulate in the liver and other major organs like kidney with the flow of blood. Yang et al. [49] investigated the interaction mechanism of nanomaterials with multiple biological tissues. By nanomaterials passivation, hydrophobicity/hydrophilicity, dissolution, and coating, particles may tend to interact with cell membranes and surrounding medium. Thus, due to the systemic circulation and metabolism *in vivo*, not all intravenously injected AuNRs could

finally arrive at the tumor site. This explained the phenomenon that the CT imaging of intravenous injection was not satisfied as subcutaneous and intramuscular injection of RGD-AuNRs. In subsequent study, we will focus on the research of the relationship between the best contrast agent loading or concentration and the multimodal imaging of gold nanomaterials.

5. Conclusion

The result is noteworthy for biomedicine applications of gold nanomaterials. And most researches have illustrated that the well-established application between strong X-ray attenuation, facile chemical and surface properties, and low toxicity has focused on gold nanoparticles-based systems. But for better clinical use, the targeting ability and multimodal imaging capability need to be further improved. Herein, first of all, compared with the existing iodine containing molecules contrast agents, gold nanorods (AuNRs) that we synthesized are more promising as CT contrast agents for its nontoxic, high contrast, long imaging time, and other advantages. In the second part, the modification of RGD peptide could improve biocompatibility and stability of AuNRs. RGD-AuNRs targeting tumor CT imaging has improved the resolution of tumor tissue. RGD-AuNRs could be excreted without toxic side effects. And the RGD-AuNRs based targeting therapy agents can be applied on various tumors with high expression of integrin $\alpha_v\beta_3$.

In a word, the RGD-AuNRs that we compounded as a significant potential candidate in biomedical applications possess many advantages. First, AuNRs have an adjustable optical property. The longitudinal plasma resonance absorption peaks of RGD-AuNRs that we synthesized was in the near-infrared light region. Second, the strong penetration of near-infrared light in tissues makes it possible to improve the imaging depth of AuNRs. Furthermore, the good biocompatibility and nontoxicity of RGD-AuNRs that we prepared have the capacity to improve the micro-CT imaging and the ability to target U87 glioblastoma tumor models. Due to these properties, their imaging capability has been greatly improved, including CT imaging and optical imaging. Therefore, RGD-AuNRs nanoprobe can be excellent materials in biomedical applications such as tumor targeting and imaging.

Competing Interests

The authors disclose no potential competing interests.

Acknowledgments

Authors are highly thankful for Professor Shouping Zhu, Jinwang Li, and Lei Xiong in Xidian University and Professor Jing Wang and Shu Zong in Xijing Hospital for their assistance during the CT data acquisition. This work is supported by the Program of the National Basic Research and Development Program of China (973) under Grant no. 2011CB707702, the National Natural Science Foundation of China under Grant nos. 81371589, 81090272, 81101084, 81227901, and

81530058, the Natural Science Basic Research Plan in Shaanxi Province of China under Grant no. 2015JZ019, and the Fundamental Research Funds for the Central Universities (NSIZ021402).

References

- [1] P. Ray, "Multimodality molecular imaging of disease progression in living subjects," *Journal of Biosciences*, vol. 36, no. 3, pp. 499–504, 2011.
- [2] P. Huang, L. Bao, C. Zhang et al., "Folic acid-conjugated silica-modified gold nanorods for X-ray/CT imaging-guided dual-mode radiation and photo-thermal therapy," *Biomaterials*, vol. 32, no. 36, pp. 9796–9809, 2011.
- [3] R. Popovtzer, A. Agrawal, N. A. Kotov et al., "Targeted gold nanoparticles enable molecular CT imaging of cancer," *Nano Letters*, vol. 8, no. 12, pp. 4593–4596, 2008.
- [4] L. Li, L. Zhang, T. Wang et al., "Facile and scalable synthesis of novel spherical Au nanocluster assemblies@polyacrylic acid/calcium phosphate nanoparticles for dual-modal imaging-guided cancer chemotherapy," *Small*, vol. 11, no. 26, pp. 3162–3173, 2015.
- [5] X. Qu, Y. Li, L. Li, Y. Wang, J. Liang, and J. Liang, "Fluorescent gold nanoclusters: synthesis and recent biological application," *Journal of Nanomaterials*, vol. 2015, Article ID 784097, 23 pages, 2015.
- [6] A. Antonelli, C. Sfara, E. Manuali, I. J. Bruce, and M. Magnani, "Encapsulation of superparamagnetic nanoparticles into red blood cells as new carriers of MRI contrast agents," *Nanomedicine*, vol. 6, no. 2, pp. 211–223, 2011.
- [7] X. Cui, S. Belo, D. Krüger et al., "Aluminium hydroxide stabilised $MnFe_2O_4$ and Fe_3O_4 nanoparticles as dual-modality contrasts agent for MRI and PET imaging," *Biomaterials*, vol. 35, no. 22, pp. 5840–5846, 2014.
- [8] K. Morishige, D. F. Kacher, P. Libby et al., "High-resolution magnetic resonance imaging enhanced with superparamagnetic nanoparticles measures macrophage burden in atherosclerosis," *Circulation*, vol. 122, no. 17, pp. 1707–1715, 2010.
- [9] C. R. Anderson, X. Hu, H. Zhang et al., "Ultrasound molecular imaging of tumor angiogenesis with an integrin targeted microbubble contrast agent," *Investigative Radiology*, vol. 46, no. 4, pp. 215–224, 2011.
- [10] J. K. Willmann, R. H. Kimura, N. Deshpande, A. M. Lutz, J. R. Cochran, and S. S. Gambhir, "Targeted contrast-enhanced ultrasound imaging of tumor angiogenesis with contrast microbubbles conjugated to integrin-binding knottin peptides," *Journal of Nuclear Medicine*, vol. 51, no. 3, pp. 433–440, 2010.
- [11] S. M. Janib, A. S. Moses, and J. A. MacKay, "Imaging and drug delivery using theranostic nanoparticles," *Advanced Drug Delivery Reviews*, vol. 62, no. 11, pp. 1052–1063, 2010.
- [12] T. Reuveni, M. Motiei, Z. Romman, A. Popovtzer, and R. Popovtzer, "Targeted gold nanoparticles enable molecular CT imaging of cancer: an in vivo study," *International Journal of Nanomedicine*, vol. 6, pp. 2859–2864, 2011.
- [13] N. Lee, S. H. Choi, and T. Hyeon, "Nano-sized CT contrast agents," *Advanced Materials*, vol. 25, no. 19, pp. 2641–2660, 2013.
- [14] T. Luo, P. Huang, G. Gao et al., "Mesoporous silica-coated gold nanorods with embedded indocyanine green for dual mode X-ray CT and NIR fluorescence imaging," *Optics Express*, vol. 19, no. 18, pp. 17030–17039, 2011.

- [15] J. Zhang, C. Li, X. Zhang et al., "In vivo tumor-targeted dual-modal fluorescence/CT imaging using a nanoprobe co-loaded with an aggregation-induced emission dye and gold nanoparticles," *Biomaterials*, vol. 42, pp. 103–111, 2015.
- [16] A. Jakhmola, N. Anton, and T. F. Vandamme, "Inorganic nanoparticles based contrast agents for X-ray computed tomography," *Advanced Healthcare Materials*, vol. 1, no. 4, pp. 413–431, 2012.
- [17] C. Haller and I. Hizoh, "The cytotoxicity of iodinated radiocontrast agents on renal cells in vitro," *Investigative Radiology*, vol. 39, no. 3, pp. 149–154, 2004.
- [18] I. Hizoh and C. Haller, "Radiocontrast-induced renal tubular cell apoptosis: hypertonic versus oxidative stress," *Investigative Radiology*, vol. 37, no. 8, pp. 428–434, 2002.
- [19] M. Shilo, T. Reuveni, M. Motiei, and R. Popovtzer, "Nanoparticles as computed tomography contrast agents: current status and future perspectives," *Nanomedicine*, vol. 7, no. 2, pp. 257–269, 2012.
- [20] <http://physics.nist.gov/PhysRefData/XrayMassCoef>.
- [21] A. Ding, Y. Chen, C. C. Wang, P. Li, and D. Shieh, "HER-2 antibody conjugated gold nano rod for in vivo photothermal therapy," in *Proceedings of the 8th IEEE Conference on Nanotechnology (NANO '08)*, pp. 882–885, IEEE, 2008.
- [22] C. J. Murphy, L. B. Thompson, A. M. Alkilany et al., "The many faces of gold nanorods," *The Journal of Physical Chemistry Letters*, vol. 1, no. 19, pp. 2867–2875, 2010.
- [23] P. Yan, N. Zhao, H. Hu, X. Lin, F. Liu, and F.-J. Xu, "A facile strategy to functionalize gold nanorods with polycation brushes for biomedical applications," *Acta Biomaterialia*, vol. 10, no. 8, pp. 3786–3794, 2014.
- [24] D. P. K. Lankveld, R. G. Rayavarapu, P. Krystek et al., "Blood clearance and tissue distribution of PEGylated and non-PEGylated gold nanorods after intravenous administration in rats," *Nanomedicine*, vol. 6, no. 2, pp. 339–349, 2011.
- [25] H. Liao and J. H. Hafner, "Gold nanorod bioconjugates," *Chemistry of Materials*, vol. 17, no. 18, pp. 4636–4641, 2005.
- [26] S. Liu, "Radiolabeled cyclic RGD peptides as integrin $\alpha_v\beta_3$ -targeted radiotracers: maximizing binding affinity via bivalency," *Bioconjugate Chemistry*, vol. 20, no. 12, pp. 2199–2213, 2009.
- [27] Z. Liu, B. Jia, J. Shi et al., "Tumor uptake of the RGD dimeric probe Tc^{99m} -G₃-2P₄-RGD2 is correlated with integrin $\alpha_v\beta_3$ expressed on both tumor cells and neovasculature," *Bioconjugate Chemistry*, vol. 21, no. 3, pp. 548–555, 2010.
- [28] Z. Liu, J. Shi, B. Jia et al., "Two 90Y-labeled multimeric RGD peptides RGD4 and 3PRGD2 for integrin targeted radionuclide therapy," *Molecular Pharmaceutics*, vol. 8, no. 2, pp. 591–599, 2011.
- [29] B. Nikoobakht and M. A. El-Sayed, "Preparation and growth mechanism of gold nanorods (NRs) using seed-mediated growth method," *Chemistry of Materials*, vol. 15, no. 10, pp. 1957–1962, 2003.
- [30] J. Choi, J. Yang, J. Park et al., "Specific near-IR absorption imaging of glioblastomas using integrin-targeting gold nanorods," *Advanced Functional Materials*, vol. 21, no. 6, pp. 1082–1088, 2011.
- [31] A. J. Gormley, A. Malugin, A. Ray, R. Robinson, and H. Ghandehari, "Biological evaluation of RGDfK-gold nanorod conjugates for prostate cancer treatment," *Journal of Drug Targeting*, vol. 19, no. 10, pp. 915–924, 2011.
- [32] J. F. Hainfeld, D. N. Slatkin, and H. M. Smilowitz, "The use of gold nanoparticles to enhance radiotherapy in mice," *Physics in Medicine and Biology*, vol. 49, no. 18, pp. N309–N315, 2004.
- [33] H.-X. Xia, X.-Q. Yang, J.-T. Song et al., "Folic acid-conjugated silica-coated gold nanorods and quantum dots for dual-modality CT and fluorescence imaging and photothermal therapy," *Journal of Materials Chemistry B*, vol. 2, no. 14, pp. 1945–1953, 2014.
- [34] J. F. Hainfeld, D. N. Slatkin, T. M. Focella, and H. M. Smilowitz, "Gold nanoparticles: a new X-ray contrast agent," *The British Journal of Radiology*, vol. 79, no. 939, pp. 248–253, 2006.
- [35] T. Niidome, M. Yamagata, Y. Okamoto et al., "PEG-modified gold nanorods with a stealth character for in vivo applications," *Journal of Controlled Release*, vol. 114, no. 3, pp. 343–347, 2006.
- [36] D. Kim, S. Park, J. H. Lee, Y. Y. Jeong, and S. Jon, "Antibiofouling polymer-coated gold nanoparticles as a contrast agent for in vivo X-ray computed tomography imaging," *Journal of the American Chemical Society*, vol. 129, no. 24, pp. 7661–7665, 2007.
- [37] Q.-Y. Cai, S. H. Kim, K. S. Choi et al., "Colloidal gold nanoparticles as a blood-pool contrast agent for X-ray computed tomography in mice," *Investigative Radiology*, vol. 42, no. 12, pp. 797–806, 2007.
- [38] P. K. Jain, K. S. Lee, I. H. El-Sayed, and M. A. El-Sayed, "Calculated absorption and scattering properties of gold nanoparticles of different size, shape, and composition: applications in biological imaging and biomedicine," *The Journal of Physical Chemistry B*, vol. 110, no. 14, pp. 7238–7248, 2006.
- [39] A. Gole and C. J. Murphy, "Polyelectrolyte-coated gold nanorods: synthesis, characterization and immobilization," *Chemistry of Materials*, vol. 17, no. 6, pp. 1325–1330, 2005.
- [40] Z. Sun, W. Ni, Z. Yang, X. Kou, L. Li, and J. Wang, "pH-controlled reversible assembly and disassembly of gold nanorods," *Small*, vol. 4, no. 9, pp. 1287–1292, 2008.
- [41] Y. Niidome, K. Honda, K. Higashimoto et al., "Surface modification of gold nanorods with synthetic cationic lipids," *Chemical Communications*, no. 36, pp. 3777–3779, 2007.
- [42] C. L. Gladson, "Expression of integrin $\alpha v\beta 3$ in small blood vessels of glioblastoma tumors," *Journal of Neuropathology & Experimental Neurology*, vol. 55, no. 11, pp. 1143–1149, 1996.
- [43] L. Bello, M. Francolini, P. Marthyn et al., " $\alpha v\beta 3$ and $\alpha v\beta 5$ integrin expression in glioma periphery," *Neurosurgery*, vol. 49, no. 2, pp. 380–390, 2001.
- [44] M. Bartneck, H. A. Keul, M. Wambach et al., "Effects of nanoparticle surface-coupled peptides, functional endgroups, and charge on intracellular distribution and functionality of human primary reticuloendothelial cells," *Nanomedicine: Nanotechnology, Biology, and Medicine*, vol. 8, no. 8, pp. 1282–1292, 2012.
- [45] Z. Li, P. Huang, X. Zhang et al., "RGD-conjugated dendrimer-modified gold nanorods for in vivo tumor targeting and photothermal therapy," *Molecular Pharmaceutics*, vol. 7, no. 1, pp. 94–104, 2010.
- [46] R. Haubner, W. A. Weber, A. J. Beer et al., "Noninvasive visualization of the activated $\alpha v\beta 3$ integrin in cancer patients by positron emission tomography and [¹⁸F]Galacto-RGD," *PLoS Medicine*, vol. 2, no. 3, article e70, 2005.
- [47] J. F. Hainfeld, M. J. O'Connor, F. A. Dilmanian, D. N. Slatkin, D. J. Adams, and H. M. Smilowitz, "Micro-CT enables microlocalisation and quantification of Her2-targeted gold nanoparticles within tumour regions," *British Journal of Radiology*, vol. 84, no. 1002, pp. 526–533, 2011.

- [48] Y. Dou, Y. Guo, X. Li et al., "Size-tuning ionization to optimize gold nanoparticles for simultaneous enhanced CT imaging and radiotherapy," *ACS Nano*, vol. 10, no. 2, pp. 2536–2548, 2016.
- [49] R. S. H. Yang, L. W. Chang, J.-P. Wu et al., "Persistent tissue kinetics and redistribution of nanoparticles, quantum dot 705, in mice: ICP-MS quantitative assessment," *Environmental Health Perspectives*, vol. 115, no. 9, pp. 1339–1343, 2007.

Review Article

Niosomes as Nanoparticulate Drug Carriers: Fundamentals and Recent Applications

Didem Ag Seleci, Muharrem Seleci, Johanna-Gabriela Walter, Frank Stahl, and Thomas Scheper

Institute for Technical Chemistry, Leibniz University Hannover, 30167 Hannover, Germany

Correspondence should be addressed to Frank Stahl; stahl@iftc.uni-hannover.de

Received 21 April 2016; Accepted 23 May 2016

Academic Editor: Lei Liu

Copyright © 2016 Didem Ag Seleci et al. This is an open access article distributed under the Creative Commons Attribution License, which permits unrestricted use, distribution, and reproduction in any medium, provided the original work is properly cited.

Drug delivery systems are defined as formulations aiming for transportation of a drug to the desired area of action within the body. The basic component of drug delivery systems is an appropriate carrier that protects the drug from rapid degradation or clearance and thereby enhances drug concentration in target tissues. Based on their biodegradable, biocompatible, and nonimmunogenic structure, niosomes are promising drug carriers that are formed by self-association of nonionic surfactants and cholesterol in an aqueous phase. In recent years, numerous research articles have been published in scientific journals reporting the potential of niosomes to serve as a carrier for the delivery of different types of drugs. The present review describes preparation methods, characterization techniques, and recent studies on niosomal drug delivery systems and also gives up to date information regarding recent applications of niosomes in drug delivery.

1. Introduction

Delivering drug with a controlled rate and targeted delivery received much attention in recent years. The application of nanotechnology to medicine has provided the development of multifunctional nanoparticles that, acting as drug carriers, can be loaded with different drugs. Nanocarriers present a great approach in drug delivery with promising features such as protection of drug from degradation and cleavage, controlled release, and in case of targeted delivery approaches the delivery of drug molecules to the target sites [1].

Niosomes are one of the promising drug carriers that have a bilayer structure and are formed by self-association of nonionic surfactants and cholesterol in an aqueous phase. Niosomes are biodegradable, biocompatible, and nonimmunogenic. They have long shelf life, exhibit high stability, and enable the delivery of drug at target site in a controlled and/or sustained manner [2]. In recent years, the potential of niosomes as a drug carrier has been extensively studied [3–5]. Various types of nonionic surfactants have been reported to form niosomes and enable the entrapment of a large number of drugs with a wide range of solubility [6–8]. The

composition, size, number of lamellae, and surface charge of niosomes can be varied and optimized to enhance the performance of niosomes for drug delivery.

The aim of this review is to present the fundamentals of niosome preparation and characterization as well as a description of their use in drug delivery, with particular attention to more recent studies. This review will provide an overview on the increasing interest on niosomes in the field of drug delivery.

2. Structure and Components of Niosomes

The main components of niosomes are nonionic surfactants, hydration medium and lipids such as cholesterol. The list of materials used in the preparation of niosomes has been shown in Table 1. The self-assembly of nonionic surfactants in aqueous media results in closed bilayer structures (Figure 1). A high interfacial tension between water and the hydrophobic tails of the amphiphile causes them to associate. The steric and hydrophilic repulsion between the head groups of nonionic surfactant ensure that hydrophilic termini point outwards and are in contact with water. The assembly into closed

TABLE 1: The materials used in niosome preparation.

Nonionic surfactants	Examples	References
<i>Alkyl ethers</i>		
(i) Alkyl glycerol ethers	Hexadecyl diglycerol ether (C16G2)	[9]
(ii) Polyoxyethylene glycol alkyl ethers (Brij)	Brij 30, Brij 52, Brij 72, Brij 76, Brij 78	[10–12]
<i>Crown ethers</i>	Bola	[13, 14]
<i>Alkyl esters</i>		
(i) Sorbitan fatty acid esters (Spans)	Span 20, Span 40, Span 60, Span 80, Span 65, Span 85	[15–18]
(ii) Polyoxyethylene sorbitan fatty acid esters (Tweens)	Tween 20, Tween 40, Tween 60, Tween 80, Tween 65, Tween 85	[7, 19, 20]
<i>Alkyl amides</i>		
(i) Glycosides	C-Glycoside derivative surfactant (BRM-BG)	[21]
(ii) Alkyl polyglucosides	Octyl-decyl polyglucoside (OrCG110), decyl polyglucoside (OrNS10)	[22]
<i>Fatty alcohols or fatty acids</i>		
(i) Fatty alcohols	Stearyl alcohol, cetyl alcohol, myristyl alcohol	[23]
(ii) Fatty acids	Stearic acid, palmitic acid, myristic acid	[23]
<i>Block copolymer</i>		
(i) Pluronic	Pluronic L64, Pluronic 105	[24, 25]
<i>Lipidic components</i>		
<i>Cholesterol</i>		[26]
<i>l-α-Soya phosphatidyl choline</i>		[27]
<i>Charged molecule</i>		
<i>Negative charge</i>	Diacetyl phosphate, phosphatidic acid, lipoamino acid, dihexadecyl phosphate	[28, 29]
<i>Positive charge</i>	Stearylamine, stearyl pyridinium chloride, cetyl pyridinium chloride	[29]

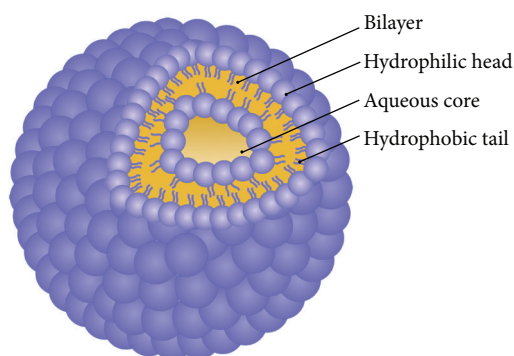


FIGURE 1: Structure of niosomes.

bilayers usually requires some input of energy such as mechanical or heat. Niosomes can be categorized in three groups according to their sizes and bilayers. Small unilamellar vesicles (SUV) (10–100 nm), large unilamellar vesicles (LUV) (100–3000 nm), and multilamellar vesicles (MLV) where more than one bilayer is present.

2.1. Nonionic Surfactants. Nonionic surfactants are a class of surfactants, which have no charged groups in their

hydrophilic heads. They are more stable and biocompatible and less toxic compared to their anionic, amphoteric, or cationic counterparts [41]. Therefore they are preferred for formation of stable niosome for *in vitro* and *in vivo* applications. Nonionic surfactants are amphiphilic molecules that comprise two different regions: one of them is hydrophilic (water-soluble) and the other one is hydrophobic (organic-soluble). Alkyl ethers, alkyl esters, alkyl amides, fatty acids are the main nonionic surfactant classes used for niosome production. The hydrophilic-lipophilic balance (HLB) and critical packing parameter (CPP) values play a critical role in the selection of surfactant molecules for niosome preparation.

2.1.1. Hydrophilic-Lipophilic Balance (HLB). HLB is a dimensionless parameter, which is the indication of the solubility of the surfactant molecule. The HLB value describes the balance between the hydrophilic portion to the lipophilic portion of the nonionic surfactant. The HLB range is from 0 to 20 for nonionic surfactants. The lower HLB refers to more lipophilic surfactant and the higher HLB to more hydrophilic surfactant. Surfactants with a HLB between 4 and 8 can be used for preparation of vesicle [42]. Hydrophilic surfactants with a HLB value ranging from 14 to 17 are not suitable to form a bilayer membrane due to their high aqueous solubility [43].

However with the addition of an optimum level of cholesterol, niosomes are indeed formed from polysorbate 80 (HLB value = 15) and Tween 20 (HLB value = 16.7) [44, 45]. Tween 20 forms stable niosome in the presence of equimolar cholesterol concentration. The interaction occurs between the hydrophobic part of the amphiphile next to head group and the 3-OH group of cholesterol at an equimolar ratio and this interaction could explain the effect of cholesterol on the formation and hydration behavior of Tween 20 niosomal membranes [46, 47].

Drug entrapment efficiency of the niosomes is also affected by HLB value of surfactant [48]. Shahiwala et al. have incorporated nimesulide into niosomes using lipid film hydration technique by changing the HLB. They found that as the HLB value of surfactant decreases from 8.6 to 1.7, entrapment efficiency decreases [43, 49].

2.1.2. Critical Packing Parameter (CPP). During the niosomal preparation, the geometry of the vesicle depends upon the critical packing parameter. On the basis of the CPP of a surfactant, the shape of nanostructures formed by self-assembly of amphiphilic molecules can be predicted. Critical packing parameter depends on the symmetry of the surfactant and can be defined using following equation [50, 51]:

$$\text{CPP} = \frac{\nu}{l_c \times a_0}, \quad (1)$$

where ν is hydrophobic group volume, l_c is the critical hydrophobic group length, and a_0 is the area of hydrophilic head group. If $\text{CPP} \leq 1/3$ corresponding, for example, to a bulky head group, small hydrophobic tail spherical micelles may form. Nonspherical micelles may form if $1/3 \leq \text{CPP} \leq 1/2$, and bilayer vesicles can occur if $1/2 \leq \text{CPP} \leq 1$. Inverted micelles form if $\text{CPP} \geq 1$ when the surfactant is composed of a voluminous tail and a small hydrophobic tail [47]. CPP could be considered as a tool for realizing, rationalizing, and predicting the self-assembled structure and its morphological transition in amphiphilic solutions [52].

2.2. Cholesterol. In the bilayer structure of niosomes, cholesterol forms hydrogen bonds with hydrophilic head of a surfactant [19, 53]. Cholesterol content of niosomes thereby influences the structures of niosomes and physical properties such as entrapment efficiency, long time stability, release of payload, and biostability [17, 46]. Cholesterol improves the rigidity of vesicles and stabilizes niosomes towards destabilizing effects induced by plasma and serum components and decreases the permeability of vesicles for entrapped molecules thus inhibiting leakage [54].

Drug entrapment efficiency plays an important role in niosomal formulations and it can be altered by varying the content of cholesterol. Agarwal et al. demonstrated that cholesterol improves the stability of enoxacin loaded niosome with increasing cholesterol content, resulting in increases of entrapment efficiency [55]. The effect of cholesterol on flurbiprofen entrapment was studied by Mokhtar et al. and cholesterol was found to have little effect on the flurbiprofen entrapment into Span 20 and Span 80 niosomes. However,

a significant increase in entrapment efficiency of flurbiprofen was obtained when 10% of cholesterol was incorporated into niosomes prepared from Span 40 and Span 60 followed by a decrease in encapsulation efficiency of the drug upon further increase in cholesterol content [56]. According to the reported results, the addition of cholesterol and its amounts needs to be optimized depending on the physical-chemical characteristic of surfactants and loaded drugs.

2.3. Charged Molecule. Charged molecules increase the stability of the vesicles by the addition of charged groups to the bilayer of vesicles. They increase surface charge density and thereby prevent vesicles aggregation. Dicetyl phosphate and phosphatidic acid are most used negatively charged molecules for niosome preparation and, similarly, stearylamine and stearyl pyridinium chloride are well-known positively charged molecules used in niosomal preparations. Normally, the charged molecule is added in niosomal formulation in an amount of 2.5–5 mol%. However increasing the amount of charged molecules can inhibit niosome formation [29].

3. Methods of Preparation

3.1. Thin-Film Hydration Method (TFH). Thin-film hydration method is a simple and well-known preparation method. In this method, the surfactants, cholesterol, and some additives such as charged molecules are dissolved in an organic solvent in a round bottomed flask. Then the organic solvent is removed using a rotary vacuum evaporator to obtain thin film on the inside wall of the flask. An aqueous solution of drug is added and the dry film is hydrated above the transition temperature (T_c) of the surfactant for specified time with constant shaking [57, 58]. Multilamellar niosomes are formed by this method.

3.2. Ether Injection Method (EIM). In ether injection method, the surfactants with additives are dissolved in diethyl ether and injected slowly through a needle in an aqueous drug solution maintained at a constant temperature, which is above the boiling point of the organic solvent. The organic solvent is evaporated using a rotary evaporator. During the vaporization the formation of single layered vesicles occurs [59–61].

3.3. Reverse Phase Evaporation Method (REV). In this method, niosomal ingredients are dissolved in a mixture of ether and chloroform and added to aqueous phase containing the drug. The resulting mixture is sonicated in order to form an emulsion and the organic phase is evaporated. Large unilamellar vesicles are formed during the evaporation of the organic solvent [62–64].

3.4. Microfluidization Method. The microfluidization method is based on submerged jet principle. In this method, the drug and the surfactant fluidized streams interact at ultrahigh velocities, in precisely defined micro channels within the interaction chamber. The high speed impingement and the energy involved leads to formation of niosomes. This method

offers greater uniformity, smaller size, unilamellar vesicles, and high reproducibility in the formulation of niosomes [65, 66].

3.5. Supercritical Carbon Dioxide Fluid (*scCO*₂). Manosroi et al. have described the supercritical reverse phase evaporation technique for niosome formation [67, 68]. They added Tween 61, cholesterol, glucose, PBS, and ethanol into the view cell and the CO₂ gas was introduced into the view cell. After magnetic stirring until equilibrium, the pressure was released and niosomal dispersions were obtained [67]. This method enables one step production and easy scale-up.

3.6. Proniosome. Proniosome technique includes the coating of a water-soluble carrier such as sorbitol and mannitol with surfactant. The coating process results in the formation of a dry formulation. This preparation is termed “Proniosomes” which requires to be hydrated before being used. The niosomes are formed by the addition of the aqueous phase. This method helps in reducing physical stability problems such as the aggregation, leaking, and fusion problem and provides convenience in dosing, distribution, transportation, and storage showing improved results compared to conventional niosomes [69].

3.7. Transmembrane pH Gradient. In this method, surfactant and cholesterol are dissolved in chloroform and evaporated to form a thin lipid film on the wall of a round bottomed flask. The film is hydrated with a solution of citric acid (pH = 4) by vortex mixing and the resulting product is freeze-thawed for niosome formation. The aqueous solution of drug is added to this niosomal suspension, after that phosphate buffer is added to maintain pH between 7.0 and 7.2 [70]. According to this method, the interior of niosome has a more acidic pH value than the outer medium. The added unionized drug passes through the niosome membrane and enters into the niosome. The drug ionizes in an acidic medium and cannot escape from the niosomal bilayer [71].

3.8. Heating Method. This is a patented method which was created by Mozafari et al. [72, 73]. Surfactants and cholesterol are separately hydrated in buffer and the solution is heated to 120°C with stirring to dissolve cholesterol. The temperature is reduced and surfactants and other additives are then added to the buffer in which cholesterol is dissolved while stirring continues. Niosomes form at this stage, are left at room temperature, and then are kept at 4–5°C under nitrogen atmosphere until use [53].

3.9. The “Bubble” Method. In this method, surfactants, additives, and the buffer are added into a glass flask with three necks. Niosome components are dispersed at 70°C and the dispersion is mixed with homogenizer. After that, immediately the flask is placed in a water bath followed by the bubbling of nitrogen gas at 70°C. Nitrogen gas is passed through a sample of homogenized surfactants resulting in formation of large unilamellar vesicles [74].

4. Characterization of Niosomes

The characterization of niosome is essential for the clinical applications. Characterization parameters have a direct impact on the stability of niosomes and a significant effect on their *in vivo* performance. Therefore these parameters such as morphology, size, polydispersity index (PI), number of lamellae, zeta potential, encapsulation efficiency, and stability must be evaluated.

4.1. Size and Morphology. Dynamic light scattering (DLS) [75], scanning electron microscopy (SEM) [76], transmission electron microscopy (TEM) [77], freeze fracture replication-electron microscopy (FF-TEM) [68], and cryotransmission electron microscopy (cryo-TEM) [67] are the most used methods for the determination of niosome sizes and morphology. DLS provides simultaneously cumulative information of particle size and valuable information on the homogeneity of the solution. A single sharp peak in the DLS profile implies existence of a single population of scatterers. The PI is helpful in this respect. It less than 0.3 corresponds to a homogenous population for colloidal systems [75]. The microscopic approaches are generally used to characterize the morphology of the niosomes.

4.2. Zeta Potential. Surface zeta potential of niosomes can be determined using zetasizer and DLS instruments. The surface charge of niosome plays an important role in the behavior of niosomes. In general, charged niosomes are more stable against aggregation than uncharged vesicles. Bayindir and Yuksel prepared paclitaxel loaded niosomes and investigated the physicochemical properties such as zeta potential of niosomes. They found that negative zeta potential values ranging between –41.7 and –58.4 mV are sufficiently high for electrostatic stabilization of niosomes [12].

4.3. Bilayer Characterization. Bilayer characteristics of niosomes have an importance on drug entrapment efficiency. The number of lamellae can be determined by AFM, NMR, and small angle X-ray scattering (SAXS) for multilamellar vesicles [54]. Membrane rigidity of niosomal formulations can be measured by means of the mobility of fluorescence probe as a function of temperature [20]. DPH (1,6 diphenyl-1,3,5-hexatriene) is most used fluorescent probe and added to niosomal dispersion. DPH normally exists in hydrophobic region in the bilayer membrane. The microviscosity of niosomal membrane is determined by fluorescence polarization. High fluorescence polarization means high microviscosity of the membrane [78]. Moreover, the bilayer thickness can be characterized using the latter method, together with the *in situ* energy-dispersive X-ray diffraction (EDXD) [79].

4.4. Entrapment Efficiency. Entrapment efficiency (EE%) is defined as the portion of the applied drug which is entrapped by the niosomes. Unencapsulated free drug can be removed from the niosomal solution using centrifugation [80], dialysis [24], or gel chromatography [81]. After this step the loaded drug can be released from niosomes by destruction of

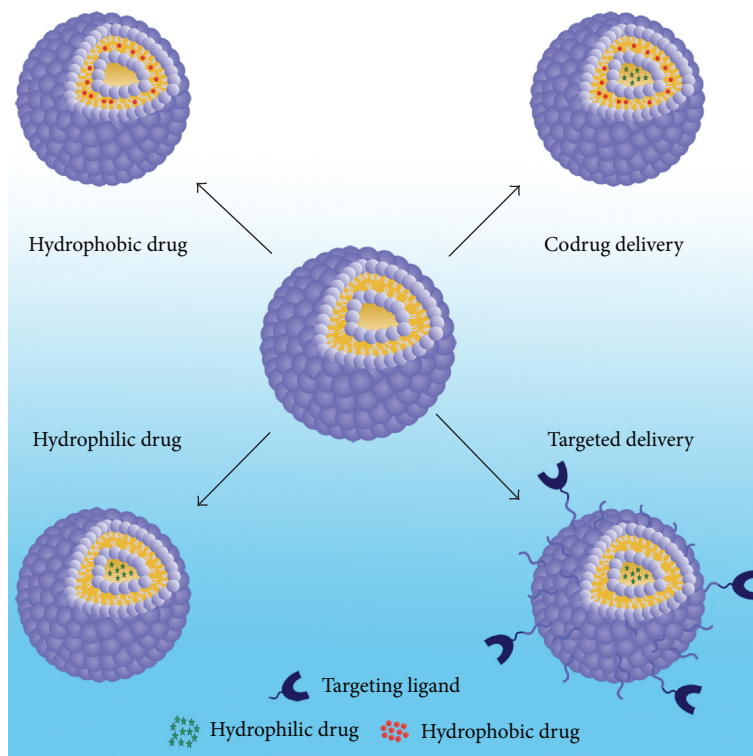


FIGURE 2: Niosomes in drug delivery.

vesicles. Niosomes can be destroyed with the addition of 0.1% Triton X-100 or methanol to niosomal suspension. The loaded and free drug concentration can be determined by a spectrophotometer [82] or high-performance liquid chromatography (HPLC) [83].

4.5. Stability. The stability of niosomes can be evaluated by determining mean vesicle size, size distribution, and entrapment efficiency over several month storage periods at different temperatures. During storage the niosomes are sampled at regular intervals of time and the percentage of drug which is retained into the niosomes is analyzed by UV spectroscopy or HPLC methods [82, 84].

4.6. In Vitro Release. One often applied method to study *in vitro* release is based on using of dialysis tubing. A dialysis bag is washed and soaked in distilled water. After 30 mins, the drug loaded niosomal suspension is transferred, into this bag. The bag containing the vesicles is immersed in buffer solution with constant shaking at 25°C or 37°C. At specific time intervals, samples were removed from the outer buffer (release medium) and replaced with the same volume of fresh buffer. The samples are analyzed for the drug content by an appropriate assay method [17].

5. Niosomes as Drug Carriers

Niosomes are very promising carriers for the delivery of numerous pharmacological and diagnostic agents. A number

of publications have reported the preparation, characterization, and use of niosomes as drug carriers. Because of their nonionic nature, they offer excellent biocompatibility and low toxicity. The unique structure of niosomes allows the development of effective novel drug delivery systems with ability of loading both hydrophilic and lipophilic drugs. Hydrophilic drugs and lipophilic drugs are entrapped into the aqueous core and membrane bilayer of niosome respectively (Figure 2).

5.1. Anticancer Drug Delivery. The current treatment for cancer is usually chemotherapy. The therapeutic efficacy of many anticancer drugs is limited by their poor penetration into tumor tissue and by their severe side effects on healthy cells. Various attempts have been made to overcome these drawbacks, including the use of niosomes as a novel drug delivery system.

5.1.1. Melanoma. Artemisone is a 10-amino-artemisinin derivative exhibiting antimalarial activity and also possessing antitumor activity. Dwivedi et al. encapsulated artemisone in niosomes using thin-film hydration method. The formulations showed highly selective cytotoxicity towards the melanoma cells with negligible toxicity towards the normal skin cells [85]. 5-Fluorouracil (5-FU), largely used in the treatment of different forms of skin cancers, was encapsulated in an innovative bola-niosomal system made up of α,ω -hexadecyl-bis-(1-aza-18-crown-6) (bola-surfactant), Span 80, and cholesterol. The percutaneous permeation of 5-FU-loaded bola-niosomes was evaluated by using human stratum

corneum and epidermis membranes. Bola-niosomes provided an increase of the drug penetration of 8- and 4-fold with respect to free drug aqueous solution [13]. The use of cisplatin is limited due to its severe toxic effects. Gude et al. synthesized niosomal cisplatin by using Span 60 and cholesterol and investigated the antimetastatic activity in experimental metastatic model of B16F10 melanoma. Their results suggest that cisplatin encapsulated in niosomes has significant antimetastatic activity and reduced toxicity when compared to free cisplatin [86].

5.1.2. Breast Cancer. 5-FU-loaded polyethylene glycol- (PEG-) coated and uncoated bola-niosomes were prepared by Cosco et al. and were tested on breast cancer cell lines (MCF-7 and T47D). Both bola-niosome formulations provided an increase in the cytotoxic effect with respect to the free drug. *In vivo* experiments on MCF-7 xenograft tumor SCID mice models showed a more effective antitumor activity of the PEGylated niosomal 5-FU at a concentration ten times lower (8 mg/kg) than that of the free solution of the drug (80 mg/kg) after a treatment of 30 days [87]. Cantharidin-entrapped niosomes were prepared by injection method. Their potential in enhancing the antitumor activities of the drug and reducing its toxicity was evaluated on human breast cancer cell line MCF-7. Moreover, *in vivo* therapeutic efficacy was investigated in S_{180} tumor-bearing mice. Mice treated with 1.0 mg/kg niosomal cantharidin showed the most effective antitumor activity, with an inhibition rate of 52.76%, which was significantly higher than that of the same concentration of free cantharidin (1.0 mg/kg, 31.05%) [88]. Recently, tamoxifen citrate niosomes were prepared by film hydration technique for localized cancer therapy through *in vitro* breast cancer cytotoxicity as well as *in vivo* solid antitumor efficacy. The optimized niosomal formulation of tamoxifen showed significantly enhanced cellular uptake (2.8-fold) and exhibited significantly greater cytotoxic activity on MCF-7 breast cancer cell line. *In vivo* experiments showed enhanced tumor volume reduction induced by niosomal tamoxifen when compared to free tamoxifen [89].

5.1.3. Ovarian Cancer. Uchegbu et al. prepared doxorubicin loaded niosomes. The activity of doxorubicin in hexadecyl diglycerol ether ($C_{16}G_2$) and Span 60 niosomes was studied against a human ovarian cancer cell line and its doxorubicin resistant subline. According to the results, there was a slight reduction in the IC_{50} against the resistant cell line when the drug was encapsulated in Span 60 niosomes in comparison to the free drug in solution [90].

5.1.4. Lung Cancer. Adriamycin was encapsulated into the niosome using a monoalkyl triglycerol ether by Kerr et al. and the activity of niosomal adriamycin compared with free adriamycin solution on human lung tumor cells grown in monolayer and spheroid culture and in tumor xenografted nude mice. The growth delay (i.e., the time taken for the tumor volume to double) was significantly longer for adriamycin (15 days) and niosomal adriamycin (11 days) than for control (5.8 days). It is possible that the therapeutic ratio of adriamycin could be further enhanced by

administration in niosomal form [91]. In another study, pentoxifylline loaded niosomes were prepared by lipid film hydration method. Intravenous administration of niosomal pentoxifylline (6 mg/kg and 10 mg/kg) resulted in significant reduction in lung nodules in an experimental metastatic B16F10 model suggesting accumulation of pentoxifylline in a distant target. Light microscopic observation of histologic sections showed a decrease in number of tumor islands in the lung [92].

5.2. Targeted Delivery. The efficiency and particularly the specificity of cellular targeting of niosomal drug delivery systems can be further improved by active targeting for tumor therapy, by using a ligand coupled to the surface of niosomes, which could be actively taken up, for example, via a receptor-mediated endocytosis. Niosome surfaces can be conjugated with small molecules and/or macromolecular targeting ligands to enable cell specific targeting [93]. Proteins and peptides, carbohydrates, aptamers, antibodies, and antibody fragments are the most commonly used molecules that bind specifically to an overexpressed target on the cell surface [94–96]. Bragagni et al. developed brain targeted niosomal formulation using with the glucose-derivative as a targeting ligand. They formulated niosomal doxorubicin composed of span : cholesterol : solulan : N-palmitoylglucosamine. Preliminary *in vivo* studies in rats showed that intravenous administration of a single dose of the developed targeted-niosomal formulation with respect to the commercial one was able to significantly reduce the hearth accumulation of the drug and to keep it longer in the blood circulation and also to allow the achievement of well detectable doxorubicin brain concentrations [30]. Moreover, an efficient tumor-targeted niosomal delivery system was designed by Tavano et al. Niosomes were prepared from a mixture of Pluronic L64 surfactant and cholesterol and doxorubicin was entrapped into the niosome. After the preparation, transferrin was conjugated to niosomes surface using EDC (N-[3-(dimethylamino)propyl]-N-ethylcarbodiimide hydrochloride) chemistry. Doxorubicin-loaded niosome anticancer activity was achieved against MCF-7 and MDA-MB-231 tumor cell lines, and a significant reduction in viability in a dose and time related manner was observed [24]. The information about some recent studies on niosomal targeted drug delivery is summarized in Table 2.

5.3. Codrug Delivery. In recent years, nanoparticles have emerged as a promising class of carriers in codelivery of multiple drugs for combination therapy [97]. Combinational therapies enhance therapeutic efficacy and decrease dosage while obtaining equal or greater levels of efficacy and reducing drug resistance [98]. Anticancer drugs often have serious side effects. With multidrug delivery system Pasut et al. achieved higher anticancer activity for carcinoma cells, whereas multidrug delivery system decreased cytotoxicity against endothelial cells and cardiomyocytes, with respect to free drug treatment. In their system, they have developed simultaneous anticancer drug epirubicin and nitric oxide carrying system, in which nitric oxide and epirubicin were covalently conjugated to each terminal of PEG. Nitric oxide acts

TABLE 2: Niosomes in targeted drug delivery.

Targeted tissue	Loaded therapeutic agent	Composition	Preparation method	Surface modification	Targeting molecule	References
Brain	Doxorubicin	Span 60, cholesterol, solulan C24, N-palmitoyl glucosamine	TLE-paddle method	—	N-Palmitoyl glucosamine	[30]
	Dynorphin-B	Span 60, cholesterol, solulan C24, N-palmitoyl glucosamine	Sonication	—	N-Palmitoyl glucosamine	[26]
	Vasoactive intestinal peptide	Span 60, cholesterol, solulan C24, N-palmitoyl glucosamine	Sonication	—	N-Palmitoyl glucosamine	[31]
Breast cancer	Doxorubicin	Oxidate pluronic L64, cholesterol	Thin-film hydration	EDC Chemistry	Transferrin	[24]
Chronic myelogenous leukemia	Doxorubicin	Tween 60, pluronic L64	Thin-film hydration	—	Magnetite	[32]
Epidermoid carcinoma	Hydroxycamptothecin	Span 60, cholesterol	Thin-film hydration	Periodate oxidation	Transferrin	[33]
	Doxorubicin	Span 60, cholesterol, solulan C24, N-palmitoyl glucosamine	Sonication	—	N-Palmitoyl glucosamine	[34]
Melanoma	Doxorubicin	Span 60, cholesterol, dicetyl phosphate, N-lauryl glucosamine	Ethanol injection method	—	N-Lauryl glucosamine	[35]

as not only protecting reagent against anthracycline induced cardiomyopathy but also sensitizer of anticancer drug treatment. In order to increase anticancer efficacy and enhance cardiocyte protecting ability of codelivery system, they used branched PEG as polymer backbone instead of linear one [99]. Multidrug resistance (MDR) of malignant neoplasm is the survival ability of cancer cells under the treatment with structurally and functionally diverse anticancer drugs. Increased drug efflux is mostly mediated by ATP-driven extrusion pump proteins of the ATP-binding cassette (ABC) superfamily, such as P-glycoprotein (P-gp) encoded by MDR-1, multidrug resistance (MDR) proteins (MRPs/ABCC) and breast cancer resistance protein (BCRP/ABCG2). These drug efflux pumps noticeably decrease the intracellular concentration of numerous therapeutic agents [100]. Chemosensitizers, such as Verapamil, Elacridar, Tariquidar, and cyclosporine A mainly act as antagonist for P-gp and suppress drug efflux and consequently recover chemosensitivity of MDR cancer cells. Paclitaxel was coencapsulated with cyclosporine A within actively targeted polymeric lipid-core micelles. P-gp inhibition with cyclosporine A caused an enhanced cytotoxicity of paclitaxel. Micelles loaded with this dual cargo demonstrated significantly higher cytotoxicity in the MDCKII-MDR1 cells than micelles loaded with paclitaxel alone [101].

Niosomes are promising nanocarriers in multidrug delivery applications [102]. Recently Sharma et al. reported the dual encapsulation of hydrophobic curcumin and hydrophilic doxorubicin in niosomes for cancer multidrug delivery [44]. Results showed that dual-drug loaded niosomes had higher cytotoxicity on HeLa cells when compared to free drugs. In another study, gallic acid, ascorbic acid, curcumin, and quercetin were encapsulated into the niosome as single agents or in combination and the effect of the drugs coencapsulation on the physicochemical properties of the carriers, on their antioxidant properties and capability to release the encapsulated materials, was evaluated [103]. Furthermore, Marianecci et al. prepared, characterized, and applied multidrug niosomes using lidocaine and ibuprofen. Results suggest the potential application of niosomes in dermal administration of the two drugs at the same time in the same pharmaceutical formulation, as useful carriers for the treatment of various skin diseases, such as acute and chronic inflammations in presence of pain [104].

5.4. Antibiotics. Niosomal carriers are also suitable for the delivery of antibiotics and anti-inflammatory agents. These carriers have been used extensively to improve poor skin penetration and as well as enhance skin retention of the drugs. Begum and coworkers designed rifampicin, a broad spectrum antibiotic, encapsulated in a niosomal delivery system. They investigated the activity of this system in *in vitro* conditions and this study showed that niosomal formulation of rifampicin is able to provide consistent and prolonged release of the drug [105]. In another study to increase efficacy of the antibiotics and reduce the dose, Akbari et al. synthesized ciprofloxacin loaded niosomes using different non-ionic surfactants and cholesterol in various concentrations by film hydration method. Drug release through bilayers and antibacterial activity of the niosomes were examined.

The results showed that cholesterol content and phase transition temperature of the surfactants influenced the performance of niosomes. Besides, all formulations presented more antibacterial activity as compared to free ciprofloxacin [106].

Vesicular systems, niosomes and liposomes, are mostly used in ophthalmic controlled delivery. Abdelbary and El-Gendy examined the feasibility of the niosomes as a carrier for the ophthalmic controlled delivery of gentamicin antibiotic. Various surfactants (Tween 60, Tween 80, or Brij 35) were combined with cholesterol and a negative charge inducer dicetyl phosphate in different molar ratios. The ability of these vesicles to entrap the selected drug was evaluated and the obtained results showed that entrapment efficiency and the release rate of gentamicin is affected by cholesterol content, type of surfactant, and the presence of charge inducer. Gentamicin loaded niosomes composed of Tween 60, cholesterol, and dicetyl phosphate were the most effective in terms of prolongation of *in vitro* drug release [107].

5.5. Anti-Inflammatory Drugs. Nonsteroidal anti-inflammatory drugs (NSAIDs) loaded niosomes have been prepared by several groups. These drugs may cause adverse effects such as mucosal irritation. Topically applied NSAIDs loaded niosomes can substantially improve drug permeation. To investigate the potential application of the niosomes for delivery of anti-inflammatory agents, Marianecci et al. synthesized ammonium glycyrrhizinate (AG) loaded niosomes using several surfactants and cholesterol at various concentrations. Drug entrapment efficiency, anisotropy, cytotoxicity and skin tolerability, and some further analysis have been performed for characterization. The AG-loaded niosomes demonstrated no toxicity and good skin tolerability and were able to improve the anti-inflammatory activity in mice. Moreover, an enhancement of the anti-inflammatory activity of the niosome delivered drug was observed on chemically induced skin erythema in humans [7].

5.6. Antiviral Drugs. Niosomes have also demonstrated the capability to deliver various antiviral agents. Ruckmani and Sankar synthesized zidovudine, which is the first anti-HIV compound approved for clinical use, encapsulated niosomes, and examined their entrapment efficiency and as well as sustainability of release. The niosomes were formulated by combining the proportions of Tween, Span, and cholesterol. Niosomes composed Tween 80 entrapped large amounts of zidovudine and the addition of dicetyl phosphate enhanced drug release for a longer time [108]. The drug leakage from Tween 80 formulations stored at room temperature was significant compared to niosomes stored at 4°C for 90 days. Besides, the results of a pharmacokinetic study in rabbits also confirmed that Tween 80 formulations with dicetyl phosphate were cleared from the circulation within five hours [109].

6. Recent Studies

Over the past three decades, niosomes have been successfully used as a drug carriers to overcome some major biopharmaceutical problems such as insolubility, side effects, and

TABLE 3: Recent studies on niosomes in drug delivery.

Type of the drug	Name of the drug	Composition	Experimental model	Year	References
Angiotensin receptor blockers	Candesartan cilexetil	Span 60, cholesterol, dicetyl phosphate, maltodextrin	<i>In vitro</i> dissolution test for proniosomal tablets, <i>in vivo</i> evaluation of proniosomal tablets, pharmacokinetic analysis	2016	[36]
Anti-inflammatory	Naproxen	Tween 80, Tween 20, cholesterol	<i>In vitro</i> drug release study, preformulation study	2016	[37]
	Dexamethasone	Span 60, cholesterol	Characterization of niosomes, <i>in vitro</i> release studies, stability test	2015	[38]
Antibacterial	Moxifloxacin	Tween 60, cholesterol	<i>In vitro</i> release studies, antimicrobial activity	2016	[39]
	Cefixime	C-Glycoside derivative surfactant, cholesterol	<i>In vitro</i> release study, biocompatibility and bioavailability studies using experimental animals	2016	[21]
Anticancer	Doxorubicin	Span 60, cholesterol, dicetyl phosphate, N-lauryl glucosamine	Optimization studies for formulation, skin irritancy, histopathological investigation of rat skin	2016	[35]
	Paclitaxel	Span 40, cholesterol, dicetyl phosphate	Formulation studies, Pharmacokinetic and tissue distribution studies	2015	[6]
Antiviral	Nevirapine	Tyloxapol, cholesterol	Diffusion kinetics of drug, microviscosity studies, <i>in vitro</i> release study	2015	[8]
H ₂ receptor antagonist	Famotidine	Span 60, cholesterol	Kinetic analysis of drug-release profiles, <i>ex vivo</i> permeability study	2016	[40]

poor chemical stability of drug molecules [110]. Table 3 summarizes the most recent applications of niosomes as drug delivery systems.

7. Strengths and Limitations of Niosomes in Drug Delivery

One of the most important strengths of niosomes compared with liposomes is their chemical stability. Niosomes are more stable against chemical degradation or oxidation and have long storage time compared to liposomes [51]. The surfactants which are used for niosomes preparation are biodegradable, biocompatible, and nonimmunogenic [83]. Handling and storage conditions of surfactants do not need any specifications. Moreover composition, size, lamellarity, stability, and surface charge of niosomes can be controlled by the type of preparation method, surfactant, cholesterol content, surface charge additives, and suspension concentration [66].

On the other hand niosomes show physical stability problems. During storage of dispersion niosomes are at risk of aggregation, fusion, drug leakage, or hydrolysis of encapsulated drugs. Furthermore the sterilization of niosomes needs much effort. Heat sterilization and membrane filtration are unsuitable for niosomes. Thus, these areas need further research to produce commercially niosomal preparations.

8. Conclusion

Niosomes are novel nano drug carriers to design effective drug delivery systems. They offer a great opportunity for loading hydrophilic, lipophilic drugs, or both drugs together.

Numbers of studies have been performed with different types of niosomes in delivery of the anticancer agents, anti-inflammatory agents, anti-infective agents, and so forth. The relevant studies demonstrated that niosomes improve the stability of the entrapped drug, reduce the dose, and enable targeted delivery to a specific type of tissue. The structural properties and characteristics of the niosomes can be enhanced by using novel preparations, loading, and modification methods for particular routes of administration. Thus, niosomes present itself as promising tools in commercially available therapeutics.

Competing Interests

The authors declare that there are no competing interests regarding the publication of this paper.

Acknowledgments

Konrad Adenauer Foundation is acknowledged for the financial support to Didem Ag Seleci. The publication of this paper was funded by the Open Access Fund of the Leibniz Universität Hannover.

References

- [1] M. Seleci, D. Ag Seleci, R. Jonczyk, F. Stahl, C. Blume, and T. Scheper, "Smart multifunctional nanoparticles in nanomedicine," *BioNanoMaterials*, vol. 17, no. 1-2, pp. 33-41, 2016.
- [2] N. B. Mahale, P. D. Thakkar, R. G. Mali, D. R. Walunj, and S. R. Chaudhari, "Niosomes: novel sustained release nonionic

- stable vesicular systems—an overview,” *Advances in Colloid and Interface Science*, vol. 183, pp. 46–54, 2012.
- [3] L. Tavano, L. Gentile, C. Oliviero Rossi, and R. Muzzalupo, “Novel gel-niosomes formulations as multicomponent systems for transdermal drug delivery,” *Colloids and Surfaces B: Biointerfaces*, vol. 110, pp. 281–288, 2013.
 - [4] K. B. Bini, D. Akhilesh, P. Prabhakara, and K. Jv, “Development and characterization of non-ionic surfactant vesicles (niosomes) for oral delivery of lornoxicam,” *International Journal of Drug Development and Research*, vol. 4, no. 3, pp. 147–154, 2012.
 - [5] Q. Li, Z. Li, W. Zeng et al., “Proniosome-derived niosomes for tacrolimus topical ocular delivery: in vitro cornea permeation, ocular irritation, and in vivo anti-allograft rejection,” *European Journal of Pharmaceutical Sciences*, vol. 62, pp. 115–123, 2014.
 - [6] Z. S. Bayindir, A. Beşikci, and N. Yüksel, “Paclitaxel-loaded niosomes for intravenous administration: pharmacokinetics and tissue distribution in rats,” *Turkish Journal of Medical Sciences*, vol. 45, no. 6, pp. 1403–1412, 2015.
 - [7] C. Marianecci, F. Rinaldi, M. Mastriota et al., “Anti-inflammatory activity of novel ammonium glycyrrhizinate/niosomes delivery system: human and murine models,” *Journal of Controlled Release*, vol. 164, no. 1, pp. 17–25, 2012.
 - [8] S. K. Mehta and N. Jindal, “Tyloxapol niosomes as prospective drug delivery module for antiretroviral drug nevirapine,” *AAPS PharmSciTech*, vol. 16, no. 1, pp. 67–75, 2014.
 - [9] P. Arunothayanun, M.-S. Bernard, D. Q. M. Craig, I. F. Uchegbu, and A. T. Florence, “The effect of processing variables on the physical characteristics of non-ionic surfactant vesicles (niosomes) formed from a hexadecyl diglycerol ether,” *International Journal of Pharmaceutics*, vol. 201, no. 1, pp. 7–14, 2000.
 - [10] A. Pardakhty, J. Varshosaz, and A. Rouholamini, “In vitro study of polyoxyethylene alkyl ether niosomes for delivery of insulin,” *International Journal of Pharmaceutics*, vol. 328, no. 2, pp. 130–141, 2007.
 - [11] M. Manconi, D. Valenti, C. Sinico, F. Lai, G. Loy, and A. M. Fadda, “Niosomes as carriers for tretinoin: II. Influence of vesicular incorporation on tretinoin photostability,” *International Journal of Pharmaceutics*, vol. 260, no. 2, pp. 261–272, 2003.
 - [12] Z. S. Bayindir and N. Yuksel, “Characterization of niosomes prepared with various nonionic surfactants for paclitaxel oral delivery,” *Journal of Pharmaceutical Sciences*, vol. 99, no. 4, pp. 2049–2060, 2010.
 - [13] D. Paolino, D. Cosco, R. Muzzalupo, E. Trapasso, N. Picci, and M. Fresta, “Innovative bola-surfactant niosomes as topical delivery systems of 5-fluorouracil for the treatment of skin cancer,” *International Journal of Pharmaceutics*, vol. 353, no. 1–2, pp. 233–242, 2008.
 - [14] D. Paolino, R. Muzzalupo, A. Ricciardi, C. Celia, N. Picci, and M. Fresta, “In vitro and in vivo evaluation of Bola-surfactant containing niosomes for transdermal delivery,” *Biomedical Microdevices*, vol. 9, no. 4, pp. 421–433, 2007.
 - [15] T. Yoshioka, B. Sternberg, and A. T. Florence, “Preparation and properties of vesicles (niosomes) of sorbitan monoesters (Span 20, 40, 60 and 80) and a sorbitan triester (Span 85),” *International Journal of Pharmaceutics*, vol. 105, no. 1, pp. 1–6, 1994.
 - [16] V. C. Okore, A. A. Attama, K. C. Ofokansi, C. O. Esimone, and E. B. Onuigbo, “Formulation and evaluation of niosomes,” *Indian Journal of Pharmaceutical Sciences*, vol. 73, no. 3, pp. 323–328, 2011.
 - [17] D. Akhilesh, K. B. Bini, and J. V. Kamath, “Review on span-60 based non-ionic surfactant vesicles (niosomes) as novel drug delivery,” *International Journal of Research in Pharmaceutical and Biomedical Sciences*, vol. 3, pp. 6–12, 2012.
 - [18] C. P. Jain and S. P. Vyas, “Preparation and characterization of niosomes containing rifampicin for lung targeting,” *Journal of Microencapsulation*, vol. 12, no. 4, pp. 401–407, 1995.
 - [19] S. Mandal, C. Banerjee, S. Ghosh, J. Kuchlyan, and N. Sarkar, “Modulation of the photophysical properties of curcumin in nonionic surfactant (Tween-20) forming micelles and niosomes: a comparative study of different microenvironments,” *The Journal of Physical Chemistry B*, vol. 117, no. 23, pp. 6957–6968, 2013.
 - [20] L. Di Marzio, C. Marianecci, M. Petrone, F. Rinaldi, and M. Carafa, “Novel pH-sensitive non-ionic surfactant vesicles: comparison between Tween 21 and Tween 20,” *Colloids and Surfaces B: Biointerfaces*, vol. 82, no. 1, pp. 18–24, 2011.
 - [21] M. Imran, M. R. Shah, F. Ullah et al., “Glycoside-based niosomal nanocarrier for enhanced in-vivo performance of Cefixime,” *International Journal of Pharmaceutics*, vol. 505, no. 1–2, pp. 122–132, 2016.
 - [22] M. Manconi, C. Sinico, D. Valenti, F. Lai, and A. M. Fadda, “Niosomes as carriers for tretinoin: III. A study into the in vitro cutaneous delivery of vesicle-incorporated tretinoin,” *International Journal of Pharmaceutics*, vol. 311, no. 1–2, pp. 11–19, 2006.
 - [23] P. Bandyopadhyay and M. Johnson, “Fatty alcohols or fatty acids as niosomal hybrid carrier: effect on vesicle size, encapsulation efficiency and in vitro dye release,” *Colloids and Surfaces B: Biointerfaces*, vol. 58, no. 1, pp. 68–71, 2007.
 - [24] L. Tavano, R. Muzzalupo, L. Mauro, M. Pellegrino, S. Andò, and N. Picci, “Transferrin-conjugated Pluronic niosomes as a new drug delivery system for anticancer therapy,” *Langmuir*, vol. 29, no. 41, pp. 12638–12646, 2013.
 - [25] R. Muzzalupo, L. Tavano, R. Cassano, S. Trombino, T. Ferrarelli, and N. Picci, “A new approach for the evaluation of niosomes as effective transdermal drug delivery systems,” *European Journal of Pharmaceutics and Biopharmaceutics*, vol. 79, no. 1, pp. 28–35, 2011.
 - [26] M. Bragagni, N. Mennini, S. Furlanetto, S. Orlandini, C. Ghelardini, and P. Mura, “Development and characterization of functionalized niosomes for brain targeting of dynorphin-B,” *European Journal of Pharmaceutics and Biopharmaceutics*, vol. 87, no. 1, pp. 73–79, 2014.
 - [27] S. P. Vyas, R. P. Singh, S. Jain et al., “Non-ionic surfactant based vesicles (niosomes) for non-invasive topical genetic immunization against hepatitis B,” *International Journal of Pharmaceutics*, vol. 296, no. 1–2, pp. 80–86, 2005.
 - [28] A. Sankhyan and P. Pawar, “Recent trends in niosome as vesicular drug delivery system,” *Journal of Applied Pharmaceutical Science*, vol. 2, no. 6, pp. 20–32, 2012.
 - [29] V. B. Junyaprasert, V. Teeranachaiidekul, and T. Supaperm, “Effect of charged and non-ionic membrane additives on physicochemical properties and stability of niosomes,” *AAPS PharmSciTech*, vol. 9, no. 3, pp. 851–859, 2008.
 - [30] M. Bragagni, N. Mennini, C. Ghelardini, and P. Mura, “Development and characterization of niosomal formulations of doxorubicin aimed at brain targeting,” *Journal of Pharmacy and Pharmaceutical Sciences*, vol. 15, no. 1, pp. 184–196, 2012.
 - [31] C. Dufes, F. Gaillard, I. F. Uchegbu, A. G. Schätzlein, J.-C. Olivier, and J.-M. Muller, “Glucose-targeted niosomes deliver vasoactive intestinal peptide (VIP) to the brain,” *International Journal of Pharmaceutics*, vol. 285, no. 1–2, pp. 77–85, 2004.

- [32] L. Tavano, M. Vivacqua, V. Carito, R. Muzzalupo, M. C. Caroleo, and F. Nicoletta, "Doxorubicin loaded magneto-niosomes for targeted drug delivery," *Colloids and Surfaces B: Biointerfaces*, vol. 102, pp. 803–807, 2013.
- [33] M. Hong, S. Zhu, Y. Jiang, G. Tang, and Y. Pei, "Efficient tumor targeting of hydroxycamptothecin loaded PEGylated niosomes modified with transferrin," *Journal of Controlled Release*, vol. 133, no. 2, pp. 96–102, 2009.
- [34] C. Dufes, J.-M. Muller, W. Couet, J.-C. Olivier, I. F. Uchegbu, and A. G. Schätzlein, "Anticancer drug delivery with transferrin targeted polymeric chitosan vesicles," *Pharmaceutical Research*, vol. 21, no. 1, pp. 101–107, 2004.
- [35] S. Pawar and P. Vavia, "Glucosamine anchored cancer targeted nano-vesicular drug delivery system of doxorubicin," *Journal of Drug Targeting*, vol. 24, no. 1, pp. 68–79, 2016.
- [36] N. Yuksel, Z. S. Bayindir, E. Aksakal, and A. T. Ozcelikay, "In situ niosome forming maltodextrin proniosomes of candesartan cilexetil: in vitro and in vivo evaluations," *International Journal of Biological Macromolecules*, vol. 82, pp. 453–463, 2016.
- [37] N. Shah, "Characterization, optimization and formulation of niosome containing naproxen," *Journal of Biomedical and Pharmaceutical Research*, vol. 5, no. 1, pp. 1–6, 2016.
- [38] M. A. Mavaddati, F. Moztaazadeh, and F. Baghbani, "Effect of formulation and processing variables on dexamethasone entrapment and release of niosomes," *Journal of Cluster Science*, vol. 26, no. 6, pp. 2065–2078, 2015.
- [39] S. Sohrabi, A. Haeri, A. Mahboubi, A. Mortazavi, and S. Dadashzadeh, "Chitosan gel-embedded moxifloxacin niosomes: an efficient antimicrobial hybrid system for burn infection," *International Journal of Biological Macromolecules*, vol. 85, pp. 625–633, 2016.
- [40] V. J. Mokale, H. I. Patil, A. P. Patil, P. R. Shirude, and J. B. Naik, "Formulation and optimisation of famotidine proniosomes: an in vitro and ex vivo study," *Journal of Experimental Nanoscience*, vol. 11, no. 2, pp. 97–110, 2016.
- [41] J. Jiao, "Polyoxyethylated nonionic surfactants and their applications in topical ocular drug delivery," *Advanced Drug Delivery Reviews*, vol. 60, no. 15, pp. 1663–1673, 2008.
- [42] I. F. Uchegbu and A. T. Florence, "Non-ionic surfactant vesicles (niosomes): physical and pharmaceutical chemistry," *Advances in Colloid and Interface Science*, vol. 58, no. 1, pp. 1–55, 1995.
- [43] A. Shahiwala and A. Misra, "Studies in topical application of niosomally entrapped nimesulide," *Journal of Pharmacy and Pharmaceutical Sciences*, vol. 5, no. 3, pp. 220–225, 2002.
- [44] V. Sharma, S. Anandhakumar, and M. Sasidharan, "Self-degrading niosomes for encapsulation of hydrophilic and hydrophobic drugs: an efficient carrier for cancer multi-drug delivery," *Materials Science and Engineering: C*, vol. 56, pp. 393–400, 2015.
- [45] G. Caracciolo, D. Pozzi, R. Caminiti et al., "Effect of hydration on the structure of solid-supported Niosomal membranes investigated by in situ energy dispersive X-ray diffraction," *Chemical Physics Letters*, vol. 462, no. 4–6, pp. 307–312, 2008.
- [46] B. Nasser, "Effect of cholesterol and temperature on the elastic properties of niosomal membranes," *International Journal of Pharmaceutics*, vol. 300, no. 1–2, pp. 95–101, 2005.
- [47] C. Marianecchi, L. Di Marzio, F. Rinaldi et al., "Niosomes from 80s to present: the state of the art," *Advances in Colloid and Interface Science*, vol. 205, pp. 187–206, 2014.
- [48] G. P. Kumar and P. Rajeshwarrao, "Nonionic surfactant vesicular systems for effective drug delivery-an overview," *Acta Pharmaceutica Sinica B*, vol. 1, no. 4, pp. 208–219, 2011.
- [49] S. Biswal, P. N. Murthy, J. Sahu, P. Sahoo, and F. Amir, "Vesicles of non-ionic surfactants (niosomes) and drug delivery potential," *International Journal of Pharmaceutical Sciences and Nanotechnology*, vol. 1, no. 1, pp. 1–8, 2008.
- [50] J. N. Israelachvili, *Intermolecular and Surface Forces*, 1985, Academic Press, New York, NY, USA, 1985.
- [51] I. F. Uchegbu and S. P. Vyas, "Non-ionic surfactant based vesicles (niosomes) in drug delivery," *International Journal of Pharmaceutics*, vol. 172, no. 1–2, pp. 33–70, 1998.
- [52] R. A. Khalil and A.-H. A. Zarari, "Theoretical estimation of the critical packing parameter of amphiphilic self-assembled aggregates," *Applied Surface Science*, vol. 318, pp. 85–89, 2014.
- [53] S. Moghhassemi and A. Hadjizadeh, "Nano-niosomes as nanoscale drug delivery systems: an illustrated review," *Journal of Controlled Release*, vol. 185, no. 1, pp. 22–36, 2014.
- [54] T. Liu, R. Guo, W. Hua, and J. Qiu, "Structure behaviors of hemoglobin in PEG 6000/Tween 80/Span 80/H₂O niosome system," *Colloids and Surfaces A: Physicochemical and Engineering Aspects*, vol. 293, no. 1–3, pp. 255–261, 2007.
- [55] S. Agarwal, V. Bakshi, P. Vitta, A. P. Raghuram, S. Pandey, and N. Udupa, "Effect of cholesterol content and surfactant HLB on vesicle properties of niosomes," *Indian Journal of Pharmaceutical Sciences*, vol. 66, no. 1, pp. 121–123, 2004.
- [56] M. Mokhtar, O. A. Sammour, M. A. Hammad, and N. A. Megrab, "Effect of some formulation parameters on flurbiprofen encapsulation and release rates of niosomes prepared from proniosomes," *International Journal of Pharmaceutics*, vol. 361, no. 1–2, pp. 104–111, 2008.
- [57] S. Bhaskaran and P. K. Lakshmi, "Comparative evaluation of niosome formulations prepared by different techniques," *Acta Pharmaceutica Scientia*, vol. 51, no. 1, pp. 27–32, 2009.
- [58] A. J. Baillie, A. T. Florence, L. R. Hume, G. T. Muirhead, and A. Rogerson, "The preparation and properties of niosomes non-ionic surfactant vesicles," *The Journal of Pharmacy and Pharmacology*, vol. 37, no. 12, pp. 863–868, 1985.
- [59] A. Marwa, S. Omaira, E. L. G. Hanaa, and A.-S. Mohammed, "Preparation and in-vitro evaluation of diclofenac sodium niosomal formulations," *International Journal of Pharmaceutical Sciences and Research*, vol. 4, no. 5, pp. 1757–1765, 2013.
- [60] A. Rogerson, J. Cummings, N. Willmott, and A. T. Florence, "The distribution of doxorubicin in mice following administration in niosomes," *Journal of Pharmacy and Pharmacology*, vol. 40, no. 5, pp. 337–342, 1988.
- [61] S. Srinivas, Y. A. Kumar, A. Hemanth, and M. Anitha, "Preparation and evaluation of niosomes containing aceclofenac," *Digest Journal of Nanomaterials and Biostructures*, vol. 5, no. 1, pp. 249–254, 2010.
- [62] S. Moghhassemi, E. Parnian, A. Hakamivala et al., "Uptake and transport of insulin across intestinal membrane model using trimethyl chitosan coated insulin niosomes," *Materials Science and Engineering C*, vol. 46, pp. 333–340, 2015.
- [63] A. Budhiraja and G. Dhingra, "Development and characterization of a novel antiacne niosomal gel of rosmarinic acid," *Drug Delivery*, vol. 22, no. 6, pp. 723–730, 2015.
- [64] H. Kiwada, H. Niimura, Y. Fujisaki, S. Yamada, and Y. Kato, "Application of synthetic alkyl glycoside vesicles as drug carriers. I. Preparation and physical properties," *Chemical and Pharmaceutical Bulletin*, vol. 33, no. 2, pp. 753–759, 1985.
- [65] A. S. Zidan, Z. Rahman, and M. A. Khan, "Product and process understanding of a novel pediatric anti-HIV tenofovir niosomes with a high-pressure homogenizer," *European Journal of Pharmaceutical Sciences*, vol. 44, no. 1–2, pp. 93–102, 2011.

- [66] S. Verma, S. K. Singh, N. Syan, P. Mathur, and V. Valecha, "Nanoparticle vesicular systems: a versatile tool for drug delivery," *Journal of Chemical and Pharmaceutical Research*, vol. 2, no. 2, pp. 496–509, 2010.
- [67] A. Manosroi, R. Chutoprapt, M. Abe, and J. Manosroi, "Characteristics of niosomes prepared by supercritical carbon dioxide (scCO₂) fluid," *International Journal of Pharmaceutics*, vol. 352, no. 1-2, pp. 248–255, 2008.
- [68] A. Manosroi, W. Ruksiriwanich, M. Abe, H. Sakai, W. Manosroi, and J. Manosroi, "Biological activities of the rice bran extract and physical characteristics of its entrapment in niosomes by supercritical carbon dioxide fluid," *The Journal of Supercritical Fluids*, vol. 54, no. 2, pp. 137–144, 2010.
- [69] V. R. Yasam, S. L. Jakki, J. Natarajan, and G. Kuppusamy, "A review on novel vesicular drug delivery: proniosomes," *Drug Delivery*, vol. 21, no. 4, pp. 243–249, 2014.
- [70] L. D. Mayer, M. B. Bally, and P. R. Cullis, "Uptake of adriamycin into large unilamellar vesicles in response to a pH gradient," *Biochimica et Biophysica Acta (BBA)—Biomembranes*, vol. 857, no. 1, pp. 123–126, 1986.
- [71] A. K. Verma and J. C. Bindal, "A vital role of niosomes on controlled and novel drug delivery," *Indian Journal of Novel Drug Delivery*, vol. 3, pp. 238–246, 2011.
- [72] M. R. Mozafari, "A new technique for the preparation of non-toxic liposomes and nanoliposomes: the heating method," in *Nanoliposomes: From Fundamentals to Recent Developments*, pp. 91–98, Trafford Publishing, Oxford, UK, 2005.
- [73] M. R. Mozafari, C. J. Reed, and C. Rostron, "Cytotoxicity evaluation of anionic nanoliposomes and nanolipoplexes prepared by the heating method without employing volatile solvents and detergents," *Die Pharmazie*, vol. 62, no. 3, pp. 205–209, 2007.
- [74] H. Talsma, M. J. Van Steenberg, J. C. H. Borchert, and D. J. A. Crommelin, "A novel technique for the one-step preparation of liposomes and nonionic surfactant vesicles without the use of organic solvents. Liposome formation in a continuous gas stream: the 'bubble' method," *Journal of Pharmaceutical Sciences*, vol. 83, no. 3, pp. 276–280, 1994.
- [75] L. Tavano, R. Aiello, G. Ioele, N. Picci, and R. Muzzalupo, "Niosomes from glucuronic acid-based surfactant as new carriers for cancer therapy: preparation, characterization and biological properties," *Colloids and Surfaces B: Biointerfaces*, vol. 118, pp. 7–13, 2014.
- [76] A. Pripem, K. Janpim, S. Nualkaew, and P. Mahakunakorn, "Topical niosome gel of *Zingiber cassumunar* Roxb. extract for anti-inflammatory activity enhanced skin permeation and stability of compound D," *AAPS PharmSciTech*, vol. 17, no. 3, pp. 631–639, 2016.
- [77] W. Hua and T. Liu, "Preparation and properties of highly stable innocuous niosome in Span 80/PEG 400/H₂O system," *Colloids and Surfaces A: Physicochemical and Engineering Aspects*, vol. 302, no. 1, pp. 377–382, 2007.
- [78] A. Manosroi, P. Wongtrakul, J. Manosroi et al., "Characterization of vesicles prepared with various non-ionic surfactants mixed with cholesterol," *Colloids and Surfaces B: Biointerfaces*, vol. 30, no. 1-2, pp. 129–138, 2003.
- [79] D. Pozzi, R. Caminiti, C. Marianecchi et al., "Effect of cholesterol on the formation and hydration behavior of solid-supported niosomal membranes," *Langmuir*, vol. 26, no. 4, pp. 2268–2273, 2010.
- [80] D. Pando, G. Gutiérrez, J. Coca, and C. Pazos, "Preparation and characterization of niosomes containing resveratrol," *Journal of Food Engineering*, vol. 117, no. 2, pp. 227–234, 2013.
- [81] M. Tabbakhian, S. Daneshamouz, N. Tavakoli, and M. R. Jaafari, "Influence of liposomes and niosomes on the in vitro permeation and skin retention of finasteride," *Iranian Journal of Pharmaceutical Sciences*, vol. 1, no. 3, pp. 119–130, 2005.
- [82] S. K. Mehta and N. Jindal, "Formulation of Tyloxapol niosomes for encapsulation, stabilization and dissolution of anti-tubercular drugs," *Colloids and Surfaces B: Biointerfaces*, vol. 101, pp. 434–441, 2013.
- [83] A. Y. Waddad, S. Abbad, F. Yu et al., "Formulation, characterization and pharmacokinetics of Morin hydrate niosomes prepared from various non-ionic surfactants," *International Journal of Pharmaceutics*, vol. 456, no. 2, pp. 446–458, 2013.
- [84] Y. Hao, F. Zhao, N. Li, Y. Yang, and K. Li, "Studies on a high encapsulation of colchicine by a niosome system," *International Journal of Pharmaceutics*, vol. 244, no. 1-2, pp. 73–80, 2002.
- [85] A. Dwivedi, A. Mazumder, L. du Plessis, J. L. du Preez, R. K. Haynes, and J. du Plessis, "In vitro anti-cancer effects of artemisone nano-vesicular formulations on melanoma cells," *Nanomedicine: Nanotechnology, Biology, and Medicine*, vol. 11, no. 8, pp. 2041–2050, 2015.
- [86] R. P. Gude, M. G. Jadhav, S. G. A. Rao, and A. G. Jagtap, "Effects of niosomal cisplatin and combination of the same with theophylline and with activated macrophages in murine B16F10 melanoma model," *Cancer Biotherapy and Radiopharmaceuticals*, vol. 17, no. 2, pp. 183–192, 2002.
- [87] D. Cosco, D. Paolino, R. Muzzalupo et al., "Novel PEG-coated niosomes based on bola-surfactant as drug carriers for 5-fluorouracil," *Biomedical Microdevices*, vol. 11, no. 5, pp. 1115–1125, 2009.
- [88] W. Han, S. Wang, R. Liang et al., "Non-ionic surfactant vesicles simultaneously enhance antitumor activity and reduce the toxicity of cantharidin," *International Journal of Nanomedicine*, vol. 8, pp. 2187–2196, 2013.
- [89] D. S. Shaker, M. A. Shaker, and M. S. Hanafy, "Cellular uptake, cytotoxicity and *in-vivo* evaluation of Tamoxifen citrate loaded niosomes," *International Journal of Pharmaceutics*, vol. 493, no. 1-2, pp. 285–294, 2015.
- [90] I. F. Uchehgbu, J. A. Double, L. R. Kelland, J. A. Turton, and A. T. Florence, "The activity of doxorubicin niosomes against an ovarian cancer cell line and three in vivo mouse tumour models," *Journal of Drug Targeting*, vol. 3, no. 5, pp. 399–409, 1996.
- [91] D. J. Kerr, A. Rogerson, G. J. Morrison, A. T. Florence, and S. B. Kaye, "Antitumour activity and pharmacokinetics of niosome encapsulated adriamycin in monolayer, spheroid and xenograft," *British Journal of Cancer*, vol. 58, no. 4, pp. 432–436, 1988.
- [92] S. Y. Gaikwad, A. G. Jagtap, A. D. Ingle, S. G. A. Ra, and R. P. Gude, "Antimetastatic efficacy of niosomal pentoxifylline and its combination with activated macrophages in murine B16F10 melanoma model," *Cancer Biotherapy & Radiopharmaceuticals*, vol. 15, no. 6, pp. 605–615, 2000.
- [93] M. Kong, H. Park, C. Feng, L. Hou, X. Cheng, and X. Chen, "Construction of hyaluronic acid niosome as functional transdermal nanocarrier for tumor therapy," *Carbohydrate Polymers*, vol. 94, no. 1, pp. 634–641, 2013.
- [94] A. Narang and R. Mahato, *Targeted Delivery of Small and Macromolecular Drugs*, CRC Press, 2010.
- [95] D. Ag, R. Bongartz, L. E. Dogan et al., "Biofunctional quantum dots as fluorescence probe for cell-specific targeting," *Colloids and Surfaces B: Biointerfaces*, vol. 114, pp. 96–103, 2014.

- [96] M. Selecki, D. A. Selecki, M. Ciftci et al., "Nanostructured amphiphilic star-hyperbranched block copolymers for drug delivery," *Langmuir*, vol. 31, no. 15, pp. 4542–4551, 2015.
- [97] S. Gadde, "Multi-drug delivery nanocarriers for combination therapy," *MedChemComm*, vol. 6, no. 11, pp. 1916–1929, 2015.
- [98] B. Al-Lazikani, U. Banerji, and P. Workman, "Combinatorial drug therapy for cancer in the post-genomic era," *Nature Biotechnology*, vol. 30, no. 7, pp. 679–692, 2012.
- [99] G. Pasut, F. Greco, A. Mero et al., "Polymer-drug conjugates for combination anticancer therapy: investigating the mechanism of action," *Journal of Medicinal Chemistry*, vol. 52, no. 20, pp. 6499–6502, 2009.
- [100] Y. D. Livney and Y. G. Assaraf, "Rationally designed nanovehicles to overcome cancer chemoresistance," *Advanced Drug Delivery Reviews*, vol. 65, no. 13–14, pp. 1716–1730, 2013.
- [101] C. Sarisozen, I. Vural, T. Levchenko, A. A. Hincal, and V. P. Torchilin, "PEG-PE-based micelles co-loaded with paclitaxel and cyclosporine A or loaded with paclitaxel and targeted by anticancer antibody overcome drug resistance in cancer cells," *Drug Delivery*, vol. 19, no. 4, pp. 169–176, 2012.
- [102] M. Thakkar and S. Brijesh, "Opportunities and challenges for niosomes as drug delivery systems," *Current Drug Delivery*, vol. 13, pp. 1–15, 2016.
- [103] L. Tavano, R. Muzzalupo, N. Picci, and B. De Cindio, "Co-encapsulation of antioxidants into niosomal carriers: gastrointestinal release studies for nutraceutical applications," *Colloids and Surfaces B: Biointerfaces*, vol. 114, pp. 82–88, 2014.
- [104] C. Marianecchi, F. Rinaldi, L. D. Marzio, A. Ciogli, S. Esposito, and M. Carafa, "Polysorbate 20 vesicles as multi-drug carriers: in vitro preliminary evaluations," *Letters in Drug Design and Discovery*, vol. 10, no. 3, pp. 212–218, 2013.
- [105] K. Begum, A. F. Khan, H. K. Hana, J. Sheak, and R. U. Jalil, "Rifampicin niosome: preparations, characterizations and antibacterial activity against staphylococcus aureus and staphylococcus epidermidis isolated from acne," *Dhaka University Journal of Pharmaceutical Sciences*, vol. 14, no. 1, pp. 117–123, 2015.
- [106] V. Akbari, D. Abedi, A. Pardakhty, and H. Sadeghi-Aliabadi, "Release studies on ciprofloxacin loaded non-ionic surfactant vesicles," *Avicenna Journal of Medical Biotechnology*, vol. 7, no. 2, pp. 69–75, 2015.
- [107] G. Abdelbary and N. El-Gendy, "Niosome-encapsulated gentamicin for ophthalmic controlled delivery," *AAPS PharmSciTech*, vol. 9, no. 3, pp. 740–747, 2008.
- [108] K. Ruckmani and V. Sankar, "Formulation and optimization of zidovudine niosomes," *AAPS PharmSciTech*, vol. 11, no. 3, pp. 1119–1127, 2010.
- [109] K. Ruckmani, V. Sankar, and M. Sivakumar, "Tissue distribution, pharmacokinetics and stability studies of zidovudine delivered by niosomes and proniosomes," *Journal of Biomedical Nanotechnology*, vol. 6, no. 1, pp. 43–51, 2010.
- [110] H. Abdelkader, A. W. G. Alani, and R. G. Alany, "Recent advances in non-ionic surfactant vesicles (niosomes): self-assembly, fabrication, characterization, drug delivery applications and limitations," *Drug Delivery*, vol. 21, no. 2, pp. 87–100, 2014.

Research Article

Enhanced Stem Cell Osteogenic Differentiation by Bioactive Glass Functionalized Graphene Oxide Substrates

Xiaoju Mo,^{1,2} Yan Wei,¹ Xuehui Zhang,³ Qing Cai,⁴ Yang Shen,⁵ Xiaohan Dai,⁶
Song Meng,¹ Xing Liu,¹ Yun Liu,¹ Zhewen Hu,¹ and Xuliang Deng^{1,7,8}

¹Department of Geriatric Dentistry, Peking University School and Hospital of Stomatology, Beijing 100081, China

²Department of Prosthodontics, Peking University School and Hospital of Stomatology, Beijing 100081, China

³Department of Dental Materials, Peking University School and Hospital of Stomatology, Beijing 100081, China

⁴State Key Laboratory of Organic-Inorganic Composites, Key Laboratory of Carbon Fiber and Functional Polymers, Ministry of Education, Beijing University of Chemical Technology, Beijing 100029, China

⁵State Key Laboratory of New Ceramics and Fine Processing and Department of Materials Science and Engineering, Tsinghua University, Beijing 100084, China

⁶Key Laboratory of Zoonosis, Ministry of Education, Institute of Zoonosis, College of Veterinary Medicine, Jilin University, Changchun 130062, China

⁷National Engineering Laboratory for Digital and Material Technology of Stomatology, Beijing 100081, China

⁸Beijing Laboratory of Biomedical Materials, Peking University School and Hospital of Stomatology, Beijing 100081, China

Correspondence should be addressed to Xuliang Deng; kqdengxuliang@bjmu.edu.cn

Received 30 March 2016; Accepted 19 May 2016

Academic Editor: Shuai Zhang

Copyright © 2016 Xiaoju Mo et al. This is an open access article distributed under the Creative Commons Attribution License, which permits unrestricted use, distribution, and reproduction in any medium, provided the original work is properly cited.

An unmet need in engineered bone regeneration is to develop scaffolds capable of manipulating stem cells osteogenesis. Graphene oxide (GO) has been widely used as a biomaterial for various biomedical applications. However, it remains challenging to functionalize GO as ideal platform for specifically directing stem cell osteogenesis. Herein, we report facile functionalization of GO with dopamine and subsequent bioactive glass (BG) to enhance stem cell adhesion, spreading, and osteogenic differentiation. On the basis of graphene, we obtained dopamine functionalized graphene oxide/bioactive glass (DGO/BG) hybrid scaffolds containing different content of DGO by loading BG nanoparticles on graphene oxide surface using sol-gel method. To enhance the dispersion stability and facilitate subsequent nucleation of BG in GO, firstly, dopamine (DA) was used to modify GO. Then, the modified GO was functionalized with bioactive glass (BG) using sol-gel method. The adhesion, spreading, and osteoinductive effects of DGO/BG scaffold on rat bone marrow mesenchymal stem cells (rBMSCs) were evaluated. DGO/BG hybrid scaffolds with different content of DGO could influence rBMSCs' behavior. The highest expression level of osteogenic markers suggests that the DGO/BG hybrid scaffolds have great potential or elicit desired bone reparative outcome.

1. Introduction

Graphene oxide (GO), a two-dimensional monolayer of carbon atoms intimately packed into a honeycomb lattice, has shown great promise for biomedical applications [1, 2], such as cell imaging [3], drug delivery [4, 5], and biomedical device [5, 6]. Furthermore, due to its unique nanostructures, remarkable mechanical properties, and large surface area [7–9], GO has gained tremendous attentions as a new nanoplatform for stem cell culture. Lee et al. indicated that

GO substrates could promote adipogenic differentiation of MSCs because of their high affinity to insulin [10]. Kim et al. demonstrated that GO substrates provide a suitable environment for ASCs adhesion, proliferation, and differentiation with presence of osteogenic chemical inducers [11, 12]. Recent work also demonstrated that GO can act as both an effective reinforcement and a bioactivator of biopolymers such as gelatin [13] and chitosan [14], offering the biopolymer-GO composites the possibility to manipulate bone cells behavior. However, in terms of stem cells osteogenesis, it remains

a great challenge to functionalize GO as ideal substrate for the effective specification of stem cell fate to enhance bone repair.

Bioactive glasses (BG), with biomimetic composition and significant degradation [15], have been contemporarily confirmed to possess high efficiency in bonding with bone. *In vivo* experiments results showed that implanted BG produced no systemic or local toxicity [16, 17], no inflammatory affection, and no repulsive response. Some *in vitro* studies suggested that the bioactivity of BG was associated with the formation of a crystalline hydroxyapatite surface layer and controlled release of ionic dissolution products [18, 19]. Furthermore, these ion dissolution and release of BG could exert a genetic control over the osteoblast cell cycle and the rapid expression of osteogenic genes [20, 21]. These discoveries have stimulated more extensive investigations of BG utilization for bone defect repair. BG decoration on carbon fibers has been demonstrated to promote hydroxyapatite nucleation, biomineralization, and cellular ALP activity [22]. BG incorporation in PLGA was also reported to induce BG-dose-dependent cell proliferation and ALP expression [23]. As such, we hypothesized that the BG might present as a prospective candidate to functionalize GO so as to provide effective environments to modulate structure and function of GO and facilitate stem cells' osteogenic differentiation.

In this study, we designed and fabricated DGO/BG hybrid scaffold using sol-gel method as osteoinductive substrates to manipulate stem cell fate. SEM, Raman, and EDS characterization confirmed the incorporation of BG on GO without compromising their characteristic bands. The cellular activities analysis demonstrated that DGO/BG hybrid scaffolds could significantly promote the adhesion, spreading, and osteogenic differentiation of mesenchymal stem cells, due to their unique nanoscale topography, biomimetic composition, and mechanical cues.

2. Materials and Methods

2.1. Preparation and Characterization of Graphene. Graphene oxide (GO) and its reduzate have been successfully prepared using an improved Hummers' method [24] and a reduction process using hydrazine hydrate and a chemical method for the simultaneous reduction and surface functionalization of GO using dopamine hydrochloride. TEM (HRTEM, H-7650B, Hitachi, Japan) was chosen to observe the structure and morphology of the samples. The composition and phase purity of the products were examined by X-ray diffraction spectroscopy (XRD, Rigaku D/max 2500 VB2+/PC, Japan), Raman spectra (LabRAM HR Evolution, HORIBA Jobin Yvon, France), and Fourier transform infrared spectroscopy (FTIR, Avatar 360, Nicolet Co., USA).

2.2. Synthesis and Characterization of Dopamine Functionalized Graphene Oxide/Bioactive Glass (DGO/BG). DGO/BG composite with 1 wt.% and 5 wt.% GO was synthesized by sol-gel-melting method through the following steps just as Figure 1. Tetraethoxysilane (TEOS, Aldrich, USA), calcium

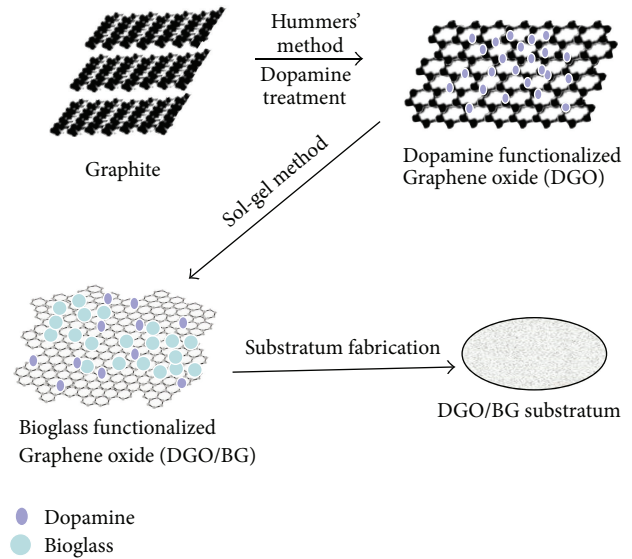


FIGURE 1: Schematic of process to synthesis DGO/BG by sol-gel-melting method in this study.

nitrate tetrahydrate (CN, Aldrich, USA), and triethyl phosphate (TEP, Aldrich, USA) were used to prepare 58S type BG by sol-gel solution. Briefly, TEP was added into a mixed solvent of distilled water, absolute ethyl alcohol, and ammonia water and stirred at 80°C for 24 h to obtain a hydrolyzed TEP solution. CN and TEOS were then dissolved into the hydrolyzed TEP solution and stirred continuously at room temperature for 120 h to generate a sol-gel solution. The DGO was dissolved in dimethylformamide (DMF, analytic pure, 99.5 wt.%, Tianjin Fine Chemical Co., China), followed by ultrasonication for 2 h. The prepared sol-gel solution was added into the solution of DGO to a total concentration of 1 wt.% and 5 wt.% DGO with different ratios. After 2 h of magnetic stirring, suspensions were dried on a hotplate at 80°C for 12 h. The composite was carbonized at 300°C for 1 h, 750°C for 2 h, and then at 1000°C for 3 h in N₂ atmosphere. Surface topography and elementary composition were observed by SEM and EMAX EX-300 system (Horiba, Japan) to confirm the successful reduction of resulting material as well as its immobilization with dopamine.

2.3. Preparation of DGO/BG-Based Substrates. Coating of glass coverslips with DGO/BG was performed as described below. In order to clean substrate, the glass coverslip with 14 mm diameter was first immersed into the piranha solution (hydrogen peroxide/sulfuric acid with the volumetric ratio of 1:3) for 10 minutes at 120°C, rinsed with ethanol and water for 5 minutes, and then blown dried by nitrogen gas at room temperature. Then the coverslip was immersed in 3% toluene solution of 3-aminopropyltriethoxysilane (3-APTES) for 30 min for functionalization. At last, it was baked with nitrogen at 125°C after being rinsed with toluene, ethanol, and water for 5 minutes again. 30 μL DGO/BG was uniformly coated on a coverslip surface by Spin Processor (Smart Coater 100, Analysis China Co., LTD) and then dried with

TABLE 1: Primers sequences utilized for real time RT-PCR.

Target gene	Forward primer sequence (5'-3')	Reverse primer sequence (5'-3')
BMP2	TGCTCAGCTTCCATCACGAAG	TCTGGAGCTCTGCAGATGTGA
BSP	GAGAACGCCACACTCTCAGG	GAGCCTTGCCCTCTGCATCT
OPN	TTTGCTTTTGCCTGTTCGGC	AGTCATCCGTTTCTTCAGAGGAC
RUNX2	AATGCCTCCGCTGTTATG	TTCTGTCTGTGCCTTCTTG

high temperature. The other samples were handled with the same way. Finally, substrates coated with these composite nanomaterial come into being four different samples: (i) functionalized graphene oxide with dopamine (DGO), (ii) 1 wt.% DGO/BG, (iii) 5 wt.% DGO/BG, and (iv) BG.

2.4. Cell Cultures and Conditions. Rat bone marrow mesenchymal stem cells (rBMSCs, Cyagen Biosciences, Inc., China) were routinely maintained in mesenchymal stem cell basal medium supplemented with 10% fetal bovine serum (FBS), 100 IU/mL penicillin-streptomycin, and 2 mM glutamine (Cyagen Biosciences, Inc., China) at 37°C in a humidified atmosphere of 5 wt.% CO₂ in air. Cells were seeded at 2.5×10^4 cells per cm² after two passages.

2.5. Immunofluorescence Staining for Cell Adhesion, Spreading, and Osteogenic Differentiation. Initial adhesion can be measured in early time ranging from 2 h to 1 d and the osteogenic differentiation usually in 7 d [25–27]. To assess the initial adhesion and osteogenic differentiation of rBMSCs, the cells were incubated with DGO/BG disks for 3 h, 1 d, and 7 d. Immunocytochemistry samples were harvested at each time point and then cells were fixed with 4.0% (w/v) paraformaldehyde for 30 min, permeabilized with 0.1 wt.% (w/v) TritonX-100 for 10 min, and blocked with 3 wt.% bovine serum albumin (BSA) for 1 h at room temperature. Samples were incubated with primary antibodies in 1 wt.% BSA for 2 h against BMP2 (abcam, ab14933), OPN (abcam, ab8448), RUNX2 (abcam, ab76956), and/or vinculin (abcam, ab18058). After removing the primary antibody, samples were incubated with secondary antibodies for 1 h at room temperature: goat anti-rabbit IgG H&L (TRITC) preadsorbed (abcam, ab50598) and goat anti-mouse IgG H&L (FITC) (abcam, ab6785). Then cells were treated with Phalloidin-Atto 565 (Sigma) for 1 h at room temperature and then stained with DAPI (Roche) for 10 min. The figures were captured by laser scanning confocal microscopy (Zeiss, LSM 780, Germany). DAPI was used to quantify cell number. The initial adhesion was evaluated by counting the number of live cells per unit area on each substrate and each group was repeated for three times.

2.6. Quantitative Real-Time PCR Analysis. rBMSCs were harvested after 7 days by TRIzol (Invitrogen) cultured on different samples. Then the isolated RNA was reverse-transcribed into cDNA utilizing the Reverse Transcription System (Promega, Madison, WI) with the manufacturer's instructions (Toyobo). Bone morphogenetic protein 2 (BMP2), bone sialoprotein (BSP), runt-related transcription

factor 2 (RUNX2), and osteopontin (OPN) were performed on the Applied ABI PRISM 7500 Real Time PCR System (Applied Biosystems, Foster City, CA) utilizing the QuantiTect SYBR Green Kit (Qiagen). The primer sequences of osteogenic genes are listed in Table 1.

2.7. Statistical Analysis. Fluorescence microscopy images were analyzed utilizing Matlab (MathWorks, Inc., R2011b) software. All quantitative data were expressed as mean \pm standard deviation (SD). The one-way ANOVA was performed for statistical analysis. Differences between groups of $*p < 0.05$ were considered statistically significant and $**p < 0.01$ was considered highly significant.

3. Results

3.1. Characteristics of Graphene. TEM images and digital photographs of graphene before and after the modification are shown in Figure 2(a). The GO sheets and DGO were smooth with folded shapes at the edges and aqueous dispersions of DGO showed a homodisperse state (Figure 2(a)(A), (B)). While following the chemical reduction, G sheets displayed a crumpled and wrinkled structure and the aqueous dispersions appeared to precipitate (Figure 2(a)(C)).

The composition and phase purity of the products were examined by XRD (Figure 2(b)). After reduction and modification, the typical GO peak at 11.28° disappears, and a new broad diffraction peak appears at 25°, corresponding to a decrease of interlayer spacing from 0.78 nm to 0.39 nm. Further characterization of the products was carried out by Raman. GO showed a D band at 1336 cm⁻¹ and G band at 1586 cm⁻¹, respectively. After modification and reduction of GO, the intensity ratio of the D band and G band (ID/IG) increased significantly (Figure 2(c) and Supplementary Figure S1 in Supplementary Material available online at <http://dx.doi.org/10.1155/2016/5613980>). FTIR was also used to characterize the products in Figure 2(d). The FTIR spectra of GO and DGO showed broad bands ranging from 3400 to 3500 cm⁻¹. The oxygen-containing functional groups of GO were revealed by the bands at 1054, 1226, 1617, and 1719 cm⁻¹.

3.2. Characterization of DGO/BG. SEM images showed topography and distribution of pure BG and BG in DGO/BG composites with different loading ratio and reaction temperature (Figures 3 and 4(a), Supplementary Figure S2). In all cases the BG particles showed a round shape. As indicated, BG particles only emerged above reaction temperature of 600°C with sol-gel method (Figure 3(a)(A)). At 1000°C, even distribution of BG particles with diameter ranging from 50 to

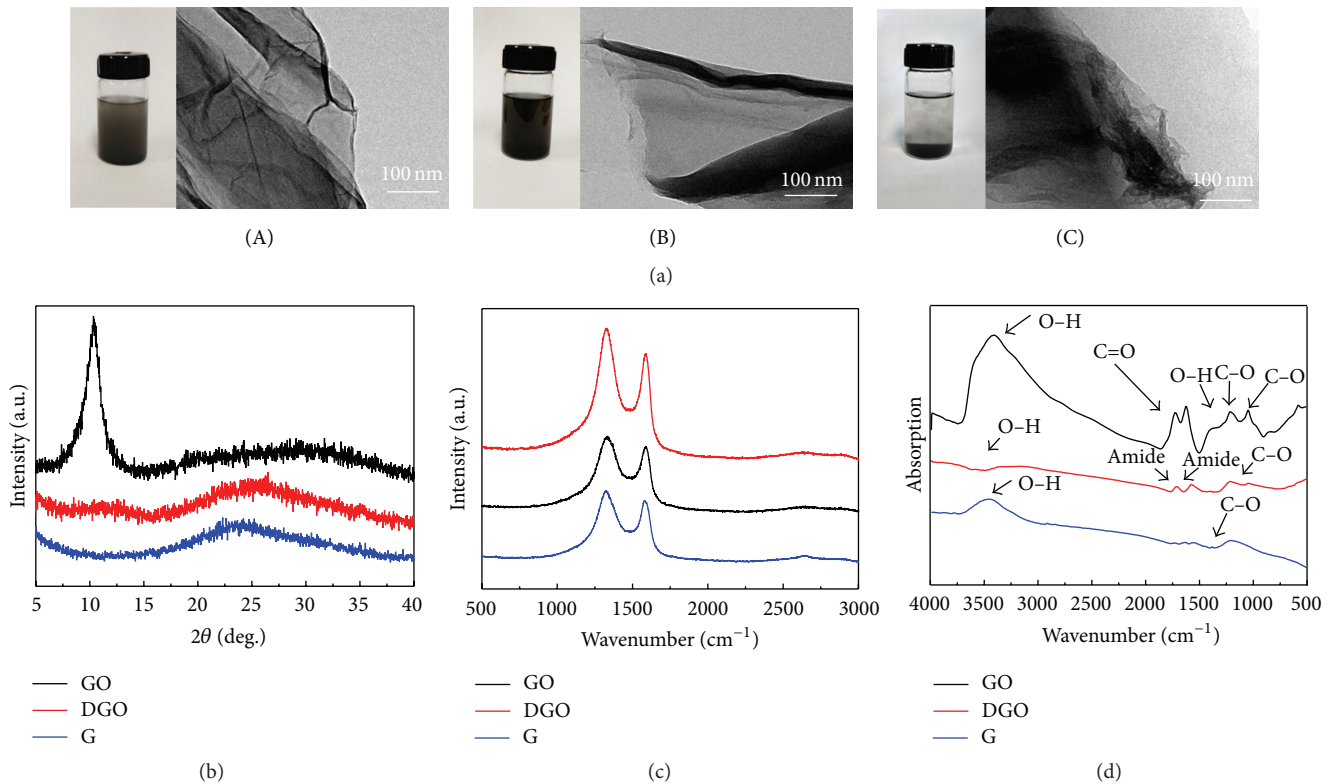


FIGURE 2: Characterization of GO, DGO, and G. (a) Digital photographs of aqueous dispersions (left) and TEM images (right) of (A) GO, (B) DGO, and (C) G. (b) XRD patterns. (c) Raman spectra. (d) FTIR spectra of GO, DGO, and G.

100 nm was achieved on 1 wt.% DGO/BG; relatively speaking, 5 wt.% DGO/BG composite resulted in more heterogeneous microscale topography with nucleation of BG particles on GO (Figures 3(b)(C) and 3(c)(C)). It should be notified that BG particles appeared to be melted and more aggregated and at 1200°C, besides fusion and densification, there is also an increase in the particles' size (Figure 3(a)(D)).

Raman spectrum (Figure 4(c)) showed that the characteristic peak of BG is at $\sim 850 \text{ cm}^{-1}$. DGO has two broad peaks known as G and D bands ($\sim 1590 \text{ cm}^{-1}$ and $\sim 1335 \text{ cm}^{-1}$, resp.). Both 1 wt.% DGO/BG and 5 wt.% DGO/BG have three broad peaks including the characteristic peaks of DGO and BG without apparent shift, suggesting that these characteristic bands were not destroyed during the functionalization process. EDS spectra (Figure 4(b)) showed that C and O elements were detected in pure DGO, the elements of C, O, Si, and Ca were detected in pure BG, and all of these elements can be detected in 1 wt.% DGO/BG and 5 wt.% DGO/BG with different ratio. These results indicated that functionalization of GO with BG has yielded DGO/BG composite scaffold.

3.3. Evaluation and Biological Properties of DGO/BG

3.3.1. Adhesion and Spreading Patterns of rBMSCs on Bioactive DGO/BG. rBMSCs cell morphology on different substrates after 3 h and 1 day of culture was observed and counted by CLSM after immunofluorescent staining (Figure 5). At 3 h, the rBMSCs presented a round shape on all substrates

(Figure 5(a)). The cell area was slightly wider on the 1 wt.% DGO/BG scaffold than other groups. After 1 day, cells cultivated on 1 wt.% and 5 wt.% DGO/BG scaffold showed more spreading, larger area, and more confluence. Cells on DGO and BG substrates showed spindle-shaped morphology with constricted cell area (Figures 5(a) and 5(c)).

3.3.2. rBMSCs Viability on DGO/BG. Figure 5(e) showed the cell viability of rBMSCs cultured on various samples at 3 h and 1 day. Cell initial adhesion on 1 wt.% DGO/BG yielded the best results followed by 5 wt.% DGO/BG. There was no significant difference between pure BG and 5 wt.% DGO/BG; both of them facilitate the cell initial adhesion, while the cell initial adhesion showed decrease on pure DGO.

3.3.3. Osteogenic Differentiation of rBMSCs on DGO/BG. BMP2, BSP, RUNX2, and OPN mRNA expression profiles at 7 days are shown in Figure 6. DGO/BG composites promoted higher expression of selected osteogenic genes. When compared to pure DGO and BG, 1 wt.% DGO/BG yielded the best results. BMP2, OPN, and RUNX2 were chosen to have immunofluorescence staining (Figure 7). All of samples allowed for osteogenic differentiation of rBMSCs but led to different differentiation characteristics. The quantitative results demonstrated that 1 wt.% DGO/BG induced significantly higher expression levels of OPN and RUNX2 compared to other samples. DGO and BG substrates show similar osteogenic differentiation propensity.

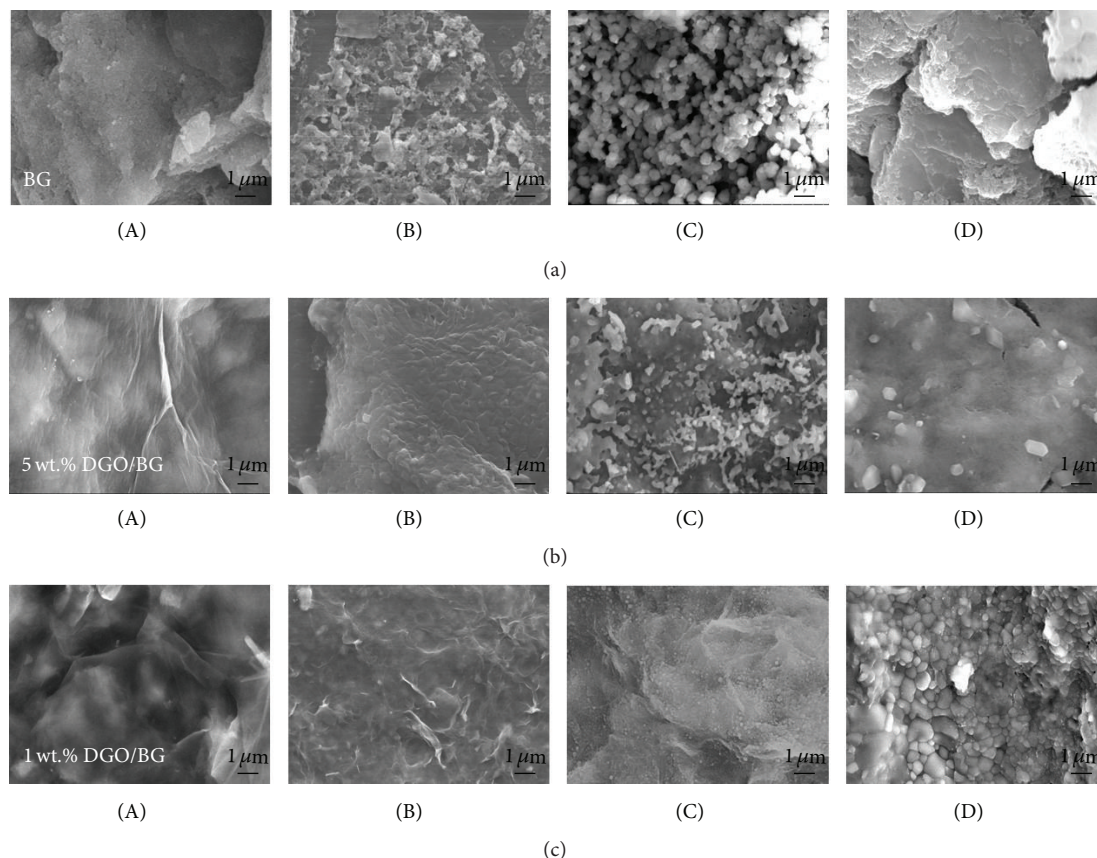


FIGURE 3: SEM images of DGO/BG composites with different loading ratio and reaction temperature. BG (a), 5 wt.% DGO/BG (b), and 1 wt.% DGO/BG (c) synthesized with different reaction temperatures: (A) 600°C, (B) 800°C, (C) 1000°C, and (D) 1200°C.

4. Discussion

Since the discovery of GO, much attention has been paid on improvement of its potential risks to biological systems so as to extend its application in biomedicine. The GO resulted hemolysis and cytotoxicity could be directly associated with its surfactant-like chemical structure with hydrophilic edges (ionized carboxyl groups) and hydrophobic plane (unoxidized sp^2 carbon skeleton), leading to strong electrostatic and hydrophobic interactions between GO and cell membrane. To enhance the biocompatibility of GO, dopamine (DA), a mussel-adhesive-protein inspired molecule, was used to partly reduce the ionized carboxyl groups on GO in this work.

TEM showed GO and DGO sheets have the typical fold morphology. While following the chemical reduction, G sheets displayed a more crumpled and wrinkled structure than GO and DGO, which is due to the lack of mutually exclusive polar groups; graphene atomic layers can stick together more easily by the van der Waals force.

The XRD showed a decrease of interlayer spacing from 0.78 nm to 0.39 nm, indicating that removal of oxygen and water from the interlayer occurred during reduction and modification. This broad peak also suggested a loss of the long range order in graphene. As indicated in Raman, the increase of the intensity ratio of the D band and G band

(ID/IG) was corresponding to high level defects with the insertion of functional groups during the modification of graphite oxide. Furthermore, the broad bands of GO and DGO ranging from 3400 to 3500 cm^{-1} shown in FTIR were corresponding to the O-H stretching vibration of adsorbed water molecules. The oxygen-containing functional groups of GO were revealed by the bands at 1054, 1226, 1617, and 1719 cm^{-1} . These bands can be assigned to the C-O stretching vibration, C-O-H deformation vibration, C=C stretching vibration, and C=O stretching vibration of COOH group, respectively [28, 29]. The bands associated with oxygen-containing functional groups decreased or disappeared significantly after reduction. Peak located at 1635 and 1558 cm^{-1} in the FTIR spectrum of DGO corresponds to the vibration of amide. Furthermore, the absorption peak of hydroxyl and epoxy group decreased after modification because of the reaction of phenolic hydroxyl group on amide and functional groups on GO and the part reduction of GO by amide. The FTIR results further agree with the XRD analyses results. Taken together, the XRD, Raman, and FTIR spectrums indicated that successful removal of oxygen and water from the interlayer occurred during reduction and high level defects with the insertion of functional groups during the modification of graphite oxide. As an amphiphilic molecule, DA has been modified onto various biopolymers,

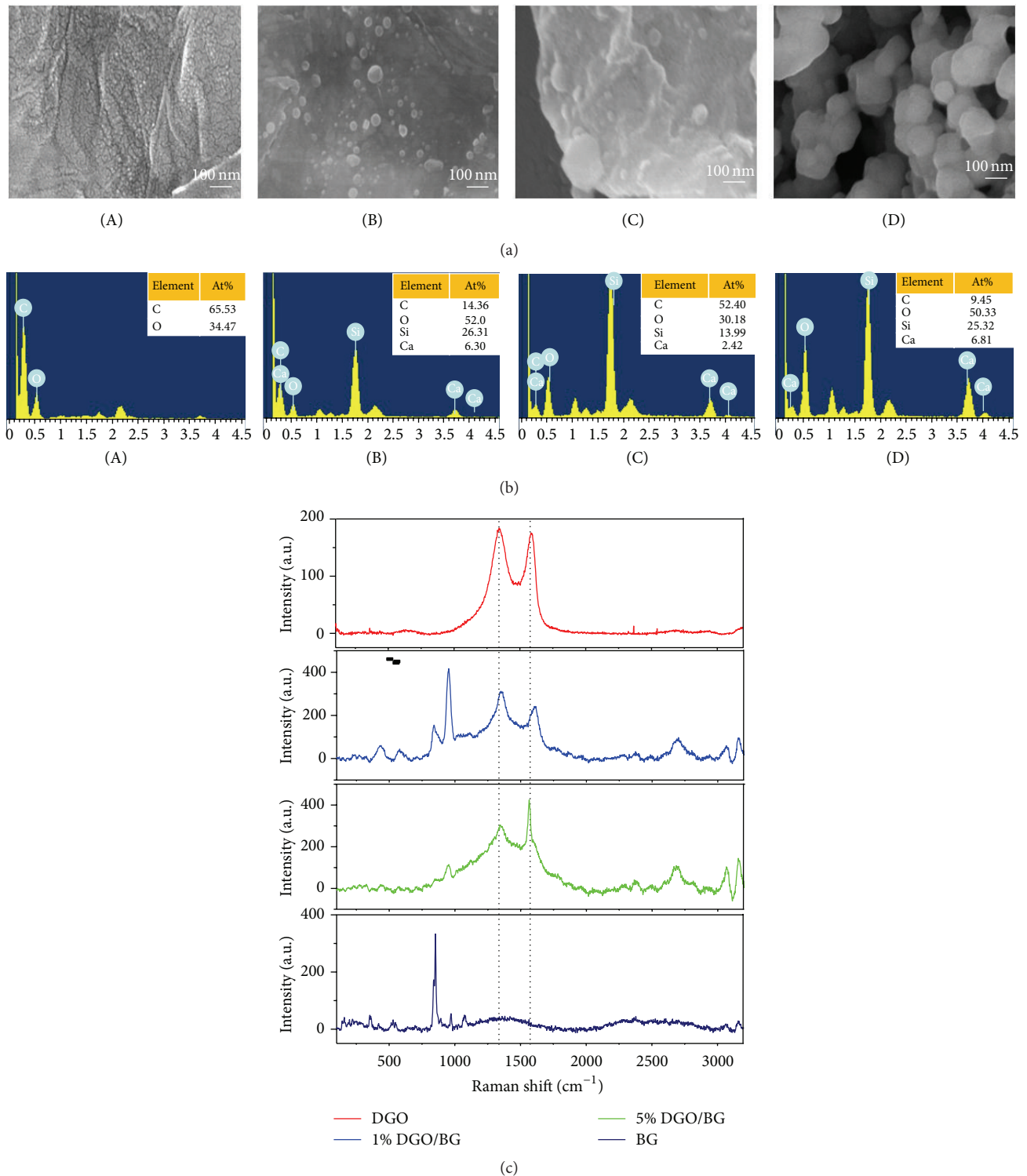


FIGURE 4: SEM images (a), EDS spectra (b), and Raman spectra (c) of different samples with 1000°C reaction temperature: (A) DGO, (B) 1 wt.% DGO/BG, (C) 5 wt.% DGO/BG, and (D) BG.

and the as-prepared biopolymers exhibited excellent adhesive ability to many kinds of solid surfaces. More recently, DA has been found to connect with GO by π -stacking. In our experiment, DA modification was found to enhance the

dispersion stability of GO, and it might also provide catechol groups to facilitate subsequent nucleation of BG on GO.

To improve the bioactivity of DGO in osteogenesis, BG was used in further surface functionalization due to its

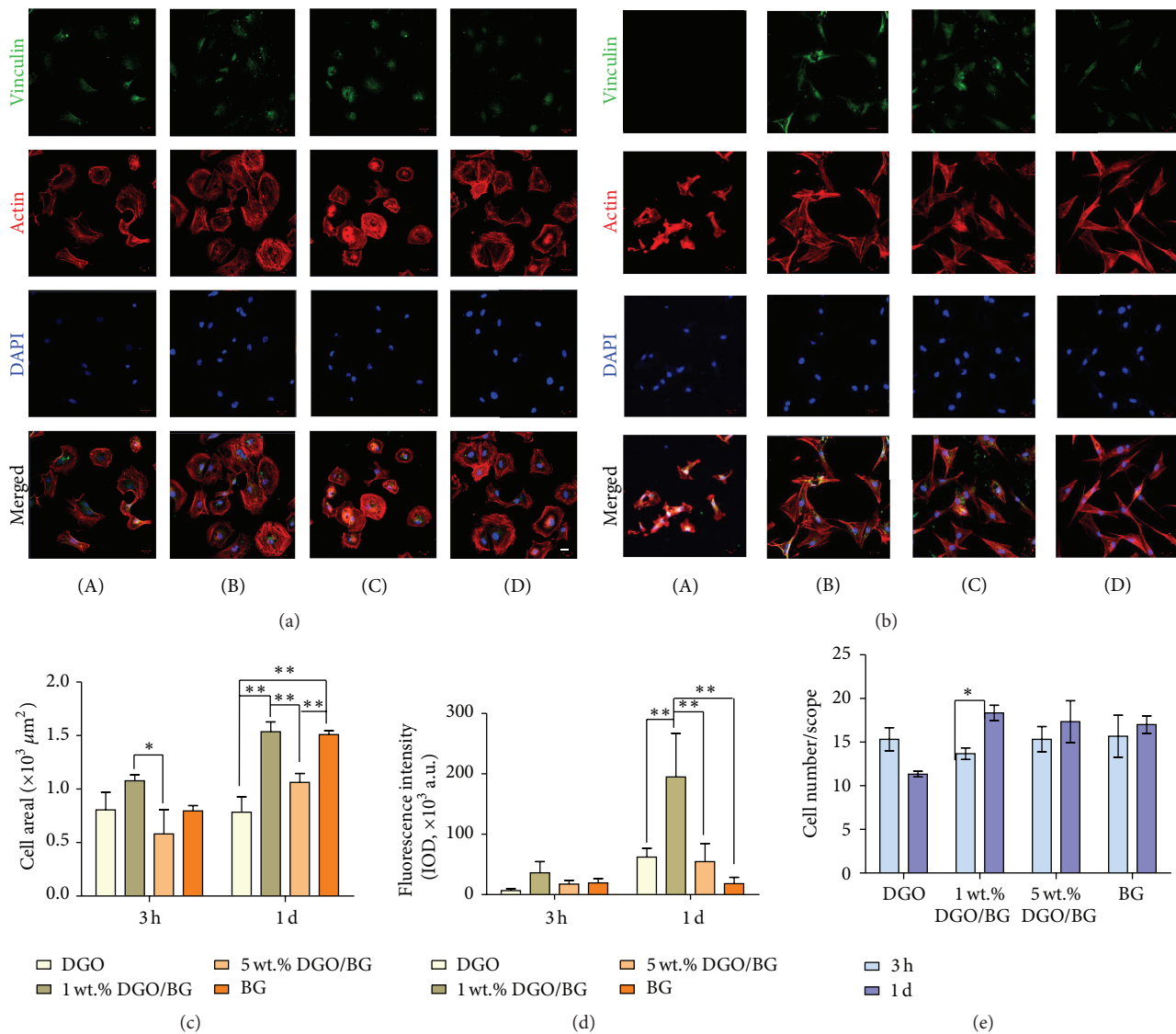


FIGURE 5: Adhesion and spreading patterns of rBMSCs on various samples. Immunostaining of vinculin (green), actin (red), and nuclei (blue) for rBMSCs cultured on the samples for 3 hours (a) and 1 day (b): (A) DGO, (B) 1 wt.% DGO/BG, (C) 5 wt.% DGO/BG, and (D) BG. Scale bars, 20 μm . The quantitative analysis of cell spreading area (c) and vinculin (d) on different samples. (e) Initial adhesion was evaluated by counting the number of live cells per unit area on each substrate at 3 hours and 1 day, and each group was repeated for three times (* $p < 0.05$, ** $p < 0.01$).

excellent osteoinductivity and osteoconductivity [21, 30, 31]. Previously, biopolymers such as polysaccharide, protein, and DNA have been used to promote the bioactivity of GO. However, in these studies, the biopolymer loading ratio, the elution of the adsorbed biopolymer, and the 2D surface morphology were difficult to be controlled. In our studies, the influences of different DGO/BG loading ratio and the sol-gel-melting technique on physical and chemical features of final composites were exquisitely controlled. As indicated in Figure 3, BG particles only emerged above reaction temperature of 600°C with sol-gel method, which proved the previous studies demonstrating that the nucleation of BG was impeded by low temperature [32]. Heterogeneous microscale particles presented on 5 wt.% DGO/BG composite scaffold,

while homogeneous distribution of nanospheric particles with diameter ranging from 50 to 100 nm was achieved at 1000°C on 1 wt.% DGO/BG. EDS spectra indicated that these particles are BG. These results indicated that the addition of DGO had generated the porous inner microstructure and coarse surface morphology for BG, which was attributed to the microphase separation between DGO and BG in the blend solution. During the carbonization and pore structure formation, BG precursors transformed into BG nanoparticles by thermodynamic driving force [33]. EDS spectra also showed that DGO/BG scaffold possessed the C element of GO and Si and Ca elements of BG. Raman spectrum demonstrated that DGO/BG composite scaffold has the characteristic peaks of both DGO and BG without

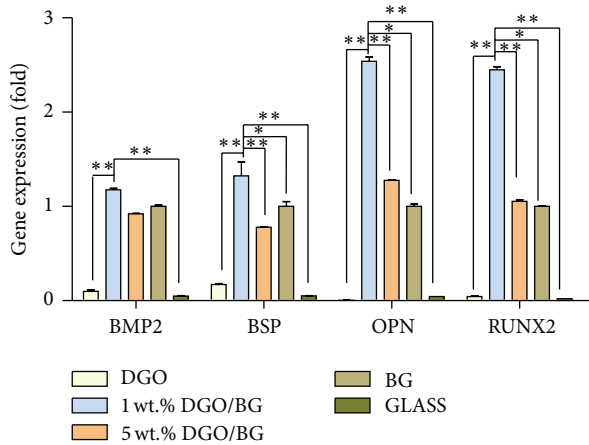


FIGURE 6: Gene expression levels of BMP2, BSP, OPN, and RUNX2 in rBMSCs cultured for 7 days (* $p < 0.05$, ** $p < 0.01$).

apparent shift, suggesting that these characteristic bands were not destroyed during the functionalization process. These results indicated that with unique topographical DGO/BG composite scaffolds were achieved with controlled DGO/BG loading ratio and sol-gel-melting technique.

As the first fundamental step of interaction with scaffold, cell adhesion could significantly impact the spreading morphology and capacity of cell proliferation and differentiation [34, 35]. Therefore, the cell adhesion and subsequent growth are essentially important markers to determine whether materials could be used as scaffolds in bone regeneration. In this study, to investigate whether the functionalization of BG on DGO would influence the initial behavior of rBMSCs, we examined the cell adhesion and spreading patterns by immunofluorescent staining at 3 h and 1 day. The immunofluorescent staining showed that rBMSCs cultivated on DGO/BG scaffolds are more favorable to rBMSCs than DGO and BG substrates with respect to cell adhesion. The stable adhesion of stem cells on substrates is a fundamental and important requirement for regulating stem cell functions. Furthermore, the qualified morphological analysis suggests that 1 wt.% and 5 wt.% DGO/BG scaffolds present much higher cell spreading area. It is widely accepted that enhanced cell spreading is an important factor to be considered for enhancing differentiation of stem cells. Additionally, cells on the DGO/BG substrates have higher cell viability than those on pure DGO and BG substrates regardless of the incorporated DGO/BG molar ratio. These results suggested that the incorporation of DGO and BG has improved the biocompatibility of both of them, yielding a suitable environment for the rBMSCs growth.

A growing number of studies suggested that the physical geometry as well as chemical composition of substrates could direct specific tissue lineages of stem cells [36]. Since as achieved DGO/BG has unique properties including topographic features and bioactive chemical components, we expected that DGO/BG scaffold would influence the differentiation of stem cells. Our study shows that all the DGO, BG, and DGO/BG scaffolds can be used to

modulate the osteogenesis of rBMSCs. In particular, 1 wt.% DGO/BG scaffold exhibits significantly highest osteogenic differentiation propensity compared to those on the other substrates, indicating that the 1 wt.% DGO/BG scaffold may have great potential for bone defect healing applications. According to the previous research, the effect of GO substrate on promoting stem cell differentiation was intimately related to its high Young's modulus [37] and the surface oxygen functional groups as well as proteins absorption [10, 38, 39]. On one hand, the favorable osteogenic lineage effect of BG was clarified to be ascribed to the release and exchange of critical concentrations of soluble Si and Ca ions. The BG nanoparticles with large surface area/volume ratio have been reported to facilitate quick ions release and high mineralization and have a significant function in genetic control over the cellular response to favor osteogenesis. Meanwhile, extensive works have demonstrated that the BG concentration is critical in cellular response to BG containing composites [40]. Moreover, the growth and differentiation of osteoblast-like cells and the kinetics of Ca-P chemistry on PLGA/BG and PDLA/BG films were shown to depend on BG content. As such, although a combination of factors including stiffness, reactive functional groups, and absorption of biomolecules on DGO/BG composite scaffolds could affect the rBMSCs osteogenic behaviors, the unique nanotopography and high bioactive BG content of 1 wt.% DGO/BG scaffold might provide more chances compared to microtopographical 5 wt.% DGO/BG to promote stem cell osteogenic differentiation. These findings suggest that the DGO/BG composite scaffolds could be used as an enabling tool for modulating the osteogenesis of stem cells.

5. Conclusions

In this study, from evaluation of the biocompatibility of DGO/BG, we found that DGO/BG hybrid scaffolds containing different content of DGO could enhance rBMSCs' adhesion, spreading, and differentiation. The TEM, XRD, Raman, and FTIR spectrums indicated successful synthesis of the typical fold morphology DGO by insertion of functional groups during the modification of graphite oxide. The dopamine modification enhanced the dispersion stability of GO and might provide catechol groups to facilitate subsequent nucleation of BG on DGO with sol-gel method. Scanning electron microscopy (SEM) showed that unique homogeneous nanospheric topography could be achieved on GO by controlling the DGO/BG molar ratio and reaction temperature. The Raman and EDS characterization confirmed the modification of BG on DGO. Higher cellular activities of cell adhesion and spreading were achieved on DGO/BG scaffolds compared to pure DGO and BG substrates. Enhanced cell adhesion and spreading were achieved on 1 wt.% and 5 wt.% DGO/BG scaffolds, indicating the favorable biocompatibility of DGO/BG. The highest expression level of osteogenic markers including BMP2, OPN, and RUNX2 was observed. The significantly high osteogenic markers expression on DGO/BG scaffold suggests that the proposed DGO/BG scaffolds could promote the osteogenic differentiation of rBMSCs. Taken together, we envision that the DGO/BG

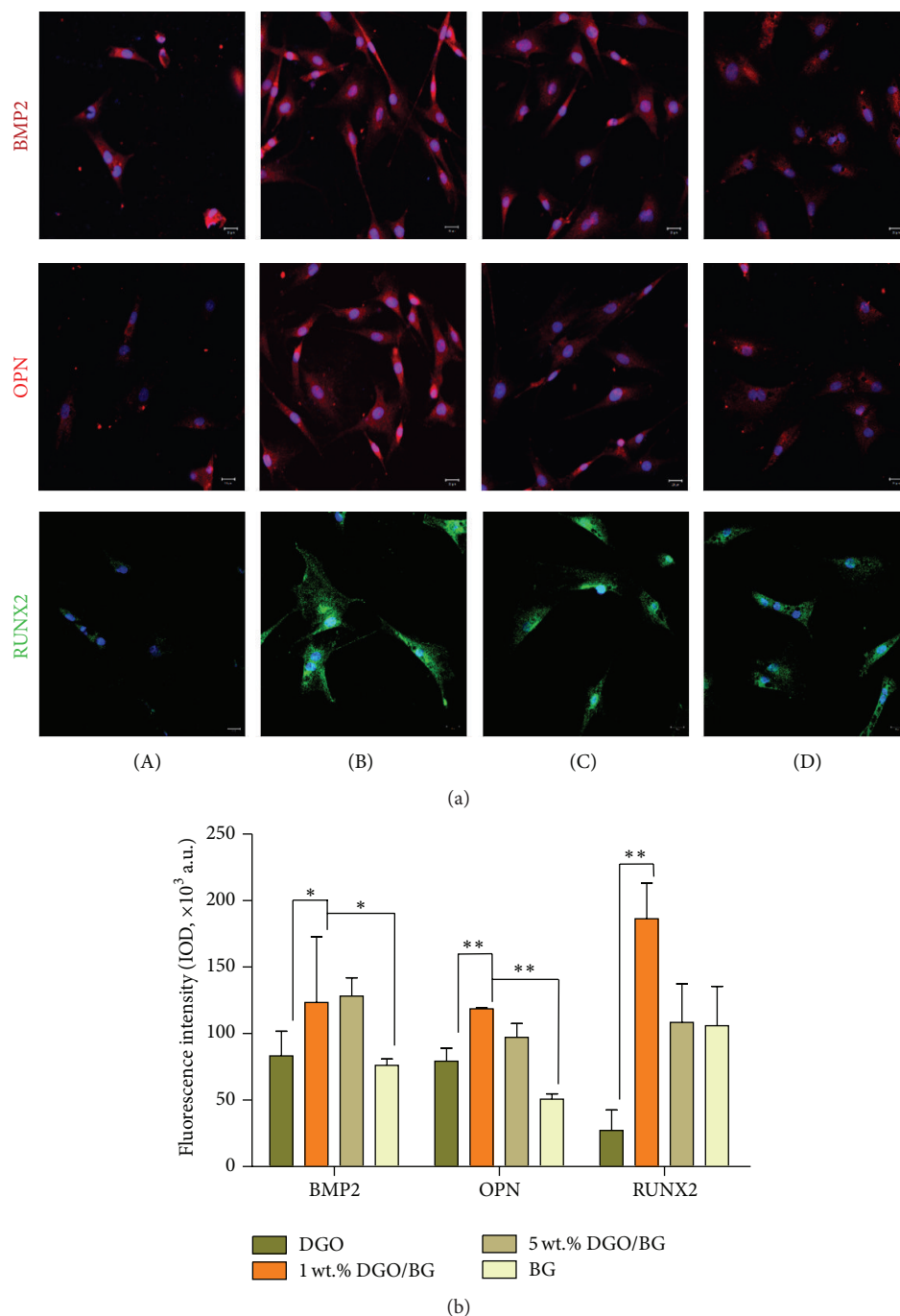


FIGURE 7: Semiquantitative analysis of GO/BG stimuli induced osteogenic differentiation of rBMSCs. (a) Immunostaining of osteogenic proteins BMP2, OPN, and RUNX2 on different samples at 7 days: (A) DGO, (B) 1 wt.% DGO/BG, (C) 5 wt.% DGO/BG, and (D) BG. Scale bars, 20 μm . (b) Quantification of mean immunofluorescence intensities of BMP2, OPN, and RUNX2 in groups as defined in (a). All measurements were performed in triplicate and analyzed by one-way ANOVA with Tukey's posttest to account for multiple comparisons. Data were plotted as mean; error bars are SEM. BMP2, red; OPN, red; RUNX2, green (* $p < 0.05$, ** $p < 0.01$).

scaffold will open avenues for next-generation graphene applications in the realm of functional biomaterial. However, further studies *in situ* are still needed to evaluate their efficacy in promoting bone regeneration and neovascularization.

Competing Interests

The authors declare that there are no competing interests regarding the publication of this paper.

Acknowledgments

This work was financially supported by the National Natural Science Foundation of China (81425007 and 51502005), the National Basic Science Research Program (2012CB933900), and the National High Technology Research and Development Program of China (2015AA033601). Additionally, the authors also acknowledge the support of the Peking University-Tsinghua University Joint Center and Beijing University of Chemical Technology for Life Sciences.

References

- [1] Q. Li, L. Liu, S. Zhang et al., "Modulating $A\beta_{33-42}$ peptide assembly by graphene oxide," *Chemistry—A European Journal*, vol. 20, no. 24, pp. 7236–7240, 2014.
- [2] J. Wang, Y. Cao, Q. Li, L. Liu, and M. Dong, "Size effect of graphene oxide on modulating amyloid peptide assembly," *Chemistry—A European Journal*, vol. 21, no. 27, pp. 9632–9637, 2015.
- [3] Z. M. Markovic, L. M. Harhaji-Trajkovic, B. M. Todorovic-Markovic et al., "In vitro comparison of the photothermal anticancer activity of graphene nanoparticles and carbon nanotubes," *Biomaterials*, vol. 32, no. 4, pp. 1121–1129, 2011.
- [4] D. Depan, J. Shah, and R. D. K. Misra, "Controlled release of drug from folate-decorated and graphene mediated drug delivery system: synthesis, loading efficiency, and drug release response," *Materials Science and Engineering C*, vol. 31, no. 7, pp. 1305–1312, 2011.
- [5] Z. Liu, J. T. Robinson, S. M. Tabakman, K. Yang, and H. Dai, "Carbon materials for drug delivery & cancer therapy," *Materials Today*, vol. 14, no. 7-8, pp. 316–323, 2011.
- [6] Z. Wang, Y. Gao, J. Xia, F. Zhang, Y. Xia, and Y. Li, "Synthesis and characterization of glycyrrhizin-decorated graphene oxide for hepatocyte-targeted delivery," *Comptes Rendus Chimie*, vol. 15, no. 8, pp. 708–713, 2012.
- [7] K. S. Novoselov, A. K. Geim, S. V. Morozov et al., "Electric field effect in atomically thin carbon films," *Science*, vol. 306, no. 5696, pp. 666–669, 2004.
- [8] L. L. Hench and J. M. Polak, "Third-generation biomedical materials," *Science*, vol. 295, no. 5557, pp. 1014–1017, 2002.
- [9] W. Wei and X. Qu, "Extraordinary physical properties of functionalized graphene," *Small*, vol. 8, no. 14, pp. 2138–2151, 2012.
- [10] W. C. Lee, C. H. Y. X. Lim, H. Shi et al., "Origin of enhanced stem cell growth and differentiation on graphene and graphene oxide," *ACS Nano*, vol. 5, no. 9, pp. 7334–7341, 2011.
- [11] J. Kim, K. S. Choi, Y. Kim et al., "Bioactive effects of graphene oxide cell culture substratum on structure and function of human adipose-derived stem cells," *Journal of Biomedical Materials Research Part A*, vol. 101, no. 12, pp. 3520–3530, 2013.
- [12] S. Some, S.-M. Ho, P. Dua et al., "Dual functions of highly potent graphene derivative-poly-L-lysine composites to inhibit bacteria and support human cells," *ACS Nano*, vol. 6, no. 8, pp. 7151–7161, 2012.
- [13] H. Liu, J. Cheng, F. Chen et al., "Gelatin functionalized graphene oxide for mineralization of hydroxyapatite: biomimetic and in vitro evaluation," *Nanoscale*, vol. 6, no. 10, pp. 5315–5322, 2014.
- [14] Y. Shi, M. Li, Q. Liu et al., "Electrophoretic deposition of graphene oxide reinforced chitosan-hydroxyapatite composite coatings for biomedical applications," *European Cells and Materials*, vol. 27, no. 3, article 48, 2013.
- [15] J. R. Jones, S. Lin, S. Yue et al., "Bioactive glass scaffolds for bone regeneration and their hierarchical characterisation," *Proceedings of the Institution of Mechanical Engineers Part H: Journal of Engineering in Medicine*, vol. 224, no. 12, pp. 1373–1387, 2010.
- [16] L. L. Hench, "Bioceramics—from concept to clinic," *Journal of the American Ceramic Society*, vol. 74, pp. 1487–1510, 1991.
- [17] T. Kokubo, H.-M. Kim, and M. Kawashita, "Novel bioactive materials with different mechanical properties," *Biomaterials*, vol. 24, no. 13, pp. 2161–2175, 2003.
- [18] L. L. Hench, "Bioceramics," *Journal of the American Ceramic Society*, vol. 81, no. 7, pp. 1705–1728, 1998.
- [19] J. R. Jones, "New trends in bioactive scaffolds: the importance of nanostructure," *Journal of the European Ceramic Society*, vol. 29, no. 7, pp. 1275–1281, 2009.
- [20] M. Tommila, A. Jokilampi, P. Terho, T. Wilson, R. Penttinen, and E. Ekholm, "Hydroxyapatite coating of cellulose sponges attracts bone-marrow-derived stem cells in rat subcutaneous tissue," *Journal of the Royal Society Interface*, vol. 6, no. 39, pp. 873–880, 2009.
- [21] S. Wang, X. Gao, W. Gong, Z. Zhang, X. Chen, and Y. Dong, "Odontogenic differentiation and dentin formation of dental pulp cells under nanobioactive glass induction," *Acta Biomaterialia*, vol. 10, no. 6, pp. 2792–2803, 2014.
- [22] C. Zhang, D. Cheng, T. Tang, X. Jia, Q. Cai, and X. Yang, "Nanoporous structured carbon nanofiber–bioactive glass composites for skeletal tissue regeneration," *Journal of Materials Chemistry B*, vol. 3, no. 26, pp. 5300–5309, 2015.
- [23] A. C. M. Renno, F. C. J. Van De Watering, M. R. Nejadnik et al., "Incorporation of bioactive glass in calcium phosphate cement: an evaluation," *Acta Biomaterialia*, vol. 9, no. 3, pp. 5728–5739, 2013.
- [24] W. S. Hummers and R. E. Offeman, "Preparation of Graphitic Oxide," *Journal of the American Chemical Society*, vol. 80, no. 6, p. 1339, 1958.
- [25] L. Zhao, L. Liu, Z. Wu, Y. Zhang, and P. K. Chu, "Effects of micropitted/nanotubular titania topographies on bone mesenchymal stem cell osteogenic differentiation," *Biomaterials*, vol. 33, no. 9, pp. 2629–2641, 2012.
- [26] C. H. Seo, H. Jeong, K. S. Furukawa, Y. Suzuki, and T. Ushida, "The switching of focal adhesion maturation sites and actin filament activation for MSCs by topography of well-defined micropatterned surfaces," *Biomaterials*, vol. 34, no. 7, pp. 1764–1771, 2013.
- [27] C. Wu, L. Xia, P. Han et al., "Graphene-oxide-modified β -tricalcium phosphate bioceramics stimulate in vitro and in vivo osteogenesis," *Carbon*, vol. 93, pp. 116–129, 2015.
- [28] Q. Q. Zhuo, J. Gao, M. Peng et al., "Large-scale synthesis of graphene by the reduction of graphene oxide at room temperature using metal nanoparticles as catalyst," *Carbon*, vol. 52, pp. 559–564, 2013.
- [29] J. Dong, J. Weng, and L. Z. Dai, "The effect of graphene on the lower critical solution temperature of poly(*N*-isopropylacrylamide)," *Carbon*, vol. 52, pp. 326–336, 2013.
- [30] J. R. Jones, P. Sepulveda, and L. L. Hench, "Dose-dependent behavior of bioactive glass dissolution," *Journal of Biomedical Materials Research*, vol. 58, no. 6, pp. 720–726, 2001.
- [31] J. Wilson, G. H. Pigott, F. J. Schoen, and L. L. Hench, "Toxicology and biocompatibility of bioglasses," *Journal of Biomedical Materials Research*, vol. 15, no. 6, pp. 805–817, 1981.

- [32] Y. Yin, F. Ye, J. Cui, F. Zhang, X. Li, and K. Yao, "Preparation and characterization of macroporous chitosan-gelatin/ β -tricalcium phosphate composite scaffolds for bone tissue engineering," *Journal of Biomedical Materials Research—Part A*, vol. 67, no. 3, pp. 844–855, 2003.
- [33] C. Kim, Y. I. Jeong, B. T. N. Ngoc et al., "Synthesis and characterization of porous carbon nanofibers with hollow cores through the thermal treatment of electrospun copolymeric nanofiber webs," *Small*, vol. 3, no. 1, pp. 91–95, 2007.
- [34] M. L. Rodriguez, P. J. McGarry, and N. J. Sniadecki, "Review on cell mechanics: experimental and modeling approaches," *Applied Mechanics Reviews*, vol. 65, no. 6, Article ID 060801, 2013.
- [35] S. R. Frenkel, R. M. Clancy, J. L. Ricci, P. E. Di Cesare, J. J. Rediske, and S. B. Abramson, "Effects of nitric oxide on chondrocyte migration, adhesion, and cytoskeletal assembly," *Arthritis and Rheumatism*, vol. 39, no. 11, pp. 1905–1912, 1996.
- [36] H. Nikukar, S. Reid, P. M. Tsimbouri, M. O. Riehle, A. S. G. Curtis, and M. J. Dalby, "Osteogenesis of mesenchymal stem cells by nanoscale mechanotransduction," *ACS Nano*, vol. 7, no. 3, pp. 2758–2767, 2013.
- [37] C. Yang, M. W. Tibbitt, L. Basta, and K. S. Anseth, "Mechanical memory and dosing influence stem cell fate," *Nature Materials*, vol. 13, no. 6, pp. 645–652, 2014.
- [38] W.-J. Li, R. Tuli, X. Huang, P. Laquerriere, and R. S. Tuan, "Multilineage differentiation of human mesenchymal stem cells in a three-dimensional nanofibrous scaffold," *Biomaterials*, vol. 26, no. 25, pp. 5158–5166, 2005.
- [39] M. Li, Q. Liu, Z. Jia et al., "Graphene oxide/hydroxyapatite composite coatings fabricated by electrophoretic nanotechnology for biological applications," *Carbon*, vol. 67, pp. 185–197, 2014.
- [40] P. Valerio, M. M. Pereira, A. M. Goes, and M. F. Leite, "The effect of ionic products from bioactive glass dissolution on osteoblast proliferation and collagen production," *Biomaterials*, vol. 25, no. 15, pp. 2941–2948, 2004.